ERROR ESTIMATION AND ADAPTIVE REFINEMENT TECHNIQUE IN THE METHOD OF MOMENTS

A Thesis
Presented to
The Academic Faculty

by

Sang Kyu Kim

In Partial Fulfillment
of the Requirements for the Degree
Doctor of Philosophy in the
School of Electrical and Computer Engineering

Georgia Institute of Technology
May 2017

ERROR ESTIMATION AND ADAPTIVE REFINEMENT TECHNIQUE IN THE METHOD OF MOMENTS

Approved by:

Dr. Andrew F. Peterson, Advisor
School of Electrical and Computer Engineering
Georgia Institute of Technology

Dr. Waymond R. Scott
School of Electrical and Computer Engineering
Georgia Institute of Technology

Dr. Gregory David Durgin
School of Electrical and Computer Engineering
Georgia Institute of Technology

Dr. Emmanouil M. Tentzeris
School of Electrical and Computer Engineering
Georgia Institute of Technology

Dr. Federico Bonetto
School of Mathematics
Georgia Institute of Technology

Date Approved: 14, December, 2016

ACKNOWLEDGEMENTS

First of all, I am truly greatful to my advisor, Dr. Andrew F. Peterson for his enormous efforts and advices throughout the Ph.D research. I am also appreciated to the reading committees of the proposal exam and the Ph.D. dissertation, Dr. Waymond R. Scott and Dr. Gregory David Durgin for offering valueable comments and reviewing the dissertation. I am also thankful to the other dissertation committees, Dr. Emmanouil M. Tentzeris and Dr. Federico Bonetto for their precious comments.

I would like to thank to members of the Propagation Group, Dr. Marcin Morys, Mr. Blake Marshall, Dr. Muhammad Bashir Akbar, Mr. Amato Francesco, Mr. Qi Cheng, Mr. Mohammad Alhassoun, Ms. Qian Yang, and Mr. Hakki Mert Torun. In addition, I would like to extend my gratitude to members of the Mixed Signal Design Group, Dr. Madhavan Swaminathan, Dr. Sung Joo Park, Dr. Jun Ki Min, Dr. Jae Young Choi, Dr. Jianyong Xie, Dr. Biancun Xie, Dr. Ming Yi, Dr. Kyu Hwan Han, Dr. Satyan Tellikepali, Dr. David Zhang, Dr. Sebastian Mueller, Mr. Rishik Bazaz, Mr. You Keun Han, and Mr. Colin Pardue.

I would like to thank to all my friends at Georgial Institute of Technology, especially for Mr. Ki Moon Lee, Mr. Eun Hwan Cho, and Mr. Chan Ho Kim. I would like to extend my special thanks to my friends and teachers in South Korea.

Finally, I am highly thankful to my parents, Mr. Kwan Soo Kim and Mrs. Young Ok Whang. Without their support and guidance, I could not have finished my doctorate course. I would like to extend my gratitude to my elder brother, Dr. Sang-Won Kim, his wife, Mrs. Saemi Hong, and their beloved daughter Da Ham Kim.

TABLE OF CONTENTS

LIST OF TABLES

LIST OF FIGURES

SUMMARY

The objective of this dissertation is to develop a reliable and computationally inexpensive adaptive refinement technique for the three-dimensional method of moments to reduce numerical errors in electromagnetics efficiently. The electric field integral equation with RWG basis functions is used to solve electromagnetic scattering problems on perfect electric conductors. Test cases are designed to induce well defined regions with large local errors on the specific domains to evaluate the adaptive h-refinement technique.

The adaptive refinement technique consists of an error estimator and a control algorithm. Error estimation plays an important role in the adaptive refinement technique because it determines regions where error is large. Various error estimators are investigated and implemented. With the Pearson correlation coefficient, local error plots, and scatter plots comparing the estimated errors with actual errors, we evaluate reliability and efficiency of the error estimators. Based on the study of the initial error estimators, we invent new error estimators, which satisfy accuracy and efficiency simultaneously.

The controller in the adaptive h-refinement technique is required to adjust mesh sizes and to maintain mesh quality over the regions that are identified for the refinement. The control algorithm distributes new nodes on the domains to be refined and employs the advancing front Delaunay algorithm to generate refined meshes. Since the quality of refined meshes can be aggravated during this procedure, we adopt Laplacian smoothing, which adjusts node positions by taking the average of their adjacent node positions. Numerical results of the error estimator assessment and the adaptive h-refinement technique will be presented and discussed.

CHAPTER I

INTRODUCTION

1.1 Background and Motivation

Electromagnetic engineering is very important in the communication and the information technologies. Designing practical applications at high frequencies such as antennas, microwave circuits, optical fiber communications, and mobile devices requires one to understand electromagnetic wave behaviors. The study of electromagnetic waves involves solving the boundary-value problem based on Maxwell's equations. Unfortunately, Maxwell's equations do not have closed form solutions in general and therefore we need to depend on numerical techniques. One of the goals of numerical EM analysis is to provide reliable and efficient approaches in order to understand scattering, propagation, and radiation of electromagnetic waves for such problems.

Surface integral equations have been popular in solving electromagnetic problems for many decades. The method of moments (MoM) is the widely-used numerical technique for solving the integral equations. In the MoM, a given geometry is discretized into small elements, called cells or meshes, and the induced surface currents on the cells are unknown variables to be determined. The unknown currents are replaced by a finite summation of basis functions. Suppose we have N basis functions (thus, N unknown variables). Then, imposing the boundary conditions gives a linear equation and applying an appropriate set of N testing functions, or weighting functions results in an $N \times N$ system of equations. Derivations and explanations of the MoM technique will be dealt with in Chapter 2.

The numerical technique has various error sources. For instance, approximations of equations, round-off, and quadrature rules for evaluating integrals can lead to errors. Using careful schemes, and increasing the order of quadrature rules can reduce these kinds of errors. Another source of errors comes from inaccurate modeling when curved surfaces are replaced by flat cells. This introduces errors when evaluating quantities at certain points

because the locations in actual geometries can be different from the flat cell models. The non-uniform rational B-splines (NURBS) and the subdivision surface technique can decrease the modeling errors by approximating curves, or curved surfaces in terms of piecewise polynomials interpolating the points on the curved surfaces.

Finally, errors due to the unknown surface current expressed by a finite summation of basis functions are referred to as discretization errors. These are usually a main source of error in the numerical technique. Moreover, they tend to be larger when the objects of interest have edges, and corners, or electromagnetic sources nearby. Therefore, the discretization errors are non-uniform in nature. This fact demands adaptive refinement techniques, which are numerical algorithms that adjust mesh sizes (h-refinement) or representation orders (p-refinement) to reduce the discretization error. We will implement an adaptive h-refinement technique in this dissertation.

Error estimation is a key ingredient of the adaptive refinement technique because its role is to determine the domains containing large errors. Unlike in the finite element method (FEM), few reliable and computationally inexpensive error estimators have been proposed for the MoM. We investigate several error estimation algorithms for the integral equations of electromagnetics problems. The accuracy and efficiency of the estimators will be evaluated by correlating them with the reference errors in various examples.

In addition to the error estimation, the adaptive h-refinement technique requires a controller. That is, the adaptive h-refinement needs to manage mesh division, mesh generation, and to maintain the quality of the mesh during the procedure. Since meshes used in our study are triangular meshes, the Delaunay triangulation algorithm is employed. The Delaunay triangulation is based on the circle test where a triangular cell is acceptable when the circumscribed circle of the cell does not include any nodes inside. The triangulation algorithm changes the shape of triangle, and the quality of the mesh can therefore decrease. We apply Laplacian smoothing, which adjusts a given node position by taking the average of adjacent nodes, to prevent this problem. Then, the algorithm solves the modified problem and this process is repeated until the error level is below the prescribed error criterion. With the error estimator and the controller, numerical solutions for electromagnetic scattering

problems will be obtained and discussed.

1.2 Contributions

The main contributions of the dissertation are following:

- The development of various error estimators including discontinuity error estimators, residual error estimators, a charge recovery error estimator, and an implicit error estimator for use in the the method of moments solution of the electric field integral equation.
- The evaluation of the error estimators quantitatively and qualitatively by using the Pearson correlation coefficient, the scatter plots and the local error plots.
- The development of combined discontinuity error estimators to fortify the discontinuity error estimators, which sometimes fail to identify large local error domains for specific test cases.
- The implementation of the adaptive h-refinement in the method of moments by using the advancing front Delaunay triangulation, and Laplacian smoothing.

1.3 Organization of the Dissertation

The dissertation is organized as follows: Chapter 2 will derive the general method of moments and the electric field integral equation (EFIE) for perfect electric conductors (PECs). The basis functions and testing functions used to formulate the integral equations are described. Chapter 2 also presents a literature survey of the error estimation and adaptive refinement techniques for the MoM. Chapter 3 introduces several error estimators: the discontinuity error estimators, the residual error estimators, the recovery error estimator, and the implicit error estimator. The Pearson correlation coefficient along with the scatter plot and the local error plot obtained by the error estimators are applied to various examples in order to evaluate the error estimators in Chapter 4. The discontinuity estimators exhibit low computational cost and often work well. However, since the discontinuity error estimators are unable to determine large error regions for several test cases, Chapter 5 introduces

combined discontinuity error estimators and compares their performance with the existing discontinuity error estimators. In Chapter 6, algorithms such as the advancing front Delaunay triangulation and Laplacian smoothing associated with the adaptive h-refinement are illustrated. Finally, we present conclusions and suggestion for future work in Chapter 7.

CHAPTER II

LITERATURE SURVEY OF THE INTEGRAL EQUATIONS FOR ELECTROMAGNETICS AND ADAPTIVE REFINEMENT TECHNIQUES

2.1 The Method of Moments

Let us consider the following equation:

$$\mathcal{L}u = f \tag{2.1}$$

where $\mathcal{L}$ is a linear operator, u is a variable, and f is a given function. The goal is to find the best approximation of (2.1) by expanding u in terms of a linear combination of basis functions $\{\phi_n\}_{n=1}^{N}$,

$$u \approx u_N = \sum_{n=1}^{N} \alpha_n \phi_n \tag{2.2}$$

where $\{\alpha_n\}_{n=1}^{N}$ are unknown coefficients to be determined. If the basis functions are orthogonal functions, the expansion (2.2) becomes linearly independent, and the coefficients α_n are called Fourier coefficients. However, the basis functions often used are linearly independent but not necessarily orthogonal [8]. This kind of basis function is usually a polynomial. Substituting (2.2) into (2.1) gives

$$\sum_{n=1}^{N} \alpha_n \mathcal{L}\phi_n = f \tag{2.3}$$

where the residual is defined as

$$\mathcal{R} = \sum_{n=1}^{N} \alpha_n \mathcal{L}\phi_n - f \tag{2.4}$$

Then, applying an inner product with weighting functions $\{w_m\}_{m=1}^{N}$, we can form the $N \times N$ system of equations of the method of moments:

$$\sum_{n=1}^{N} \alpha_n \langle \mathcal{L}\phi_n, w_m \rangle = \langle f, w_m \rangle \tag{2.5}$$

In matrix form,

$$ZI = V \tag{2.6}$$

where Z is an $N \times N$ matrix with entries

$$z_{nm} = \langle \mathcal{L}\phi_k, w_m \rangle \tag{2.7}$$

I is a column vector consisting of $\{\alpha_n\}_{n=1}^{N}$, and elements of V are given by

$$v_m = \langle f, w_m \rangle \tag{2.8}$$

2.2 The Electric Field Integral Equation for The Perfect Electric Conductor

In this section, we will derive an equation for the electromagnetic scattering problem involving a perfect electric conductor (PEC). The following derivation is called the Electric Field Integral Equation (EFIE) because it is based on the boundary condition for the tangential electric field on the PEC,

$$\hat{n} \times \left(\bar{E}^{inc} + \bar{E}^{s}\right)\big|_{\text{on S}} = 0 \tag{2.9}$$

where $\bar{E}^{inc}$ represents the given incident electric field, and $\bar{E}^{s}$ is the scattered electric field produced by the PEC target. Comparing (2.9) with (2.1), the linear operator $\mathcal{L}$ produces tangential components of the unknown scattered electric field on the PEC surface, and the given function f corresponds to the tangential component of the incident electric field. The boundary condition of the tangential magnetic field can be used in similar way,

$$\hat{n} \times \left(\bar{H}^{inc} + \bar{H}^{s}\right)\big|_{\text{on S}} = \bar{J}_s \tag{2.10}$$

Equation (2.10) is called the Magnetic Field Integral Equation (MFIE). Equations (2.9) and (2.10) state that when electromagnetic fields impinge on the PEC, they induce unknown reflected electromagnetic waves as well as surface current density on the surface S.

The surface equivalence principle allows us to change the original problem into an equivalent one: The incident field does not generate scattered waves anymore but the surface currents, which become unknown variables, on the PEC surface induce the scattered electromagnetic fields such that they satisfy the boundary conditions (2.9) and (2.10). Then,

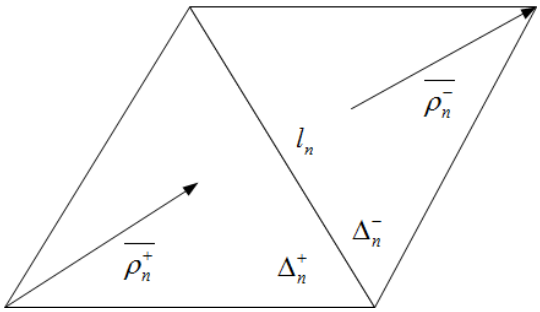

Figure 2.1: RWG basis functions.

the source-field relationship gives

$$\bar{E}^s = -jk\eta\bar{A} - \nabla\Phi_e \tag{2.11}$$

where k is the wave number, η is the intrinsic impedance, $\bar{A}$ is the magnetic vector potential, and Φ_e is the electric scalar potential. The magnetic vector potential and the electric scalar potentials are given by

$$\bar{A} = \iint_S \bar{J}_s \frac{e^{-jkR}}{4\pi R} dS \tag{2.12}$$

$$\Phi_e = \frac{jk}{\eta} \iint_S \left(\nabla \cdot \bar{J}_s\right) \frac{e^{-jkR}}{4\pi R} dS \tag{2.13}$$

$$R = \sqrt{(x-x')^2 + (y-y')^2 + (z-z')^2} \tag{2.14}$$

The PEC object is then discretized into triangular cells. This requires basis functions that are suitable for the triangular mesh. It is important that the basis functions enforce normal continuity across the cells. If normal components of the basis functions are not continuous across edges, fictitious charge sources will be generated, which result in inaccurate solutions. The Rao-Wilton-Glisson (RWG) basis functions [37], shown in Fig. 2.1, involve two triangular cells (Δ_n^+ and Δ_n^-) sharing the same edge, and satisfy the normal continuity across the edge. The RWG basis function for the n-the edge is defined as

$$\bar{B}_n(\bar{r}) = \begin{cases} \dfrac{l_n}{2A_n^+}\rho_n^+ & \bar{r} \in \Delta_n^+ \\ \dfrac{l_n}{2A_n^-}\rho_n^- & \bar{r} \in \Delta_n^- \\ 0 & \text{otherwise} \end{cases} \tag{2.15}$$

where l_n is the length of the n-th edge, A_n^+ and A_n^- are the areas of Δ_n^+ and Δ_n^-, respectively. The local position vector ρ_n^+ is defined from the free vertex of Δ_n^+. Position vector ρ_n^- for

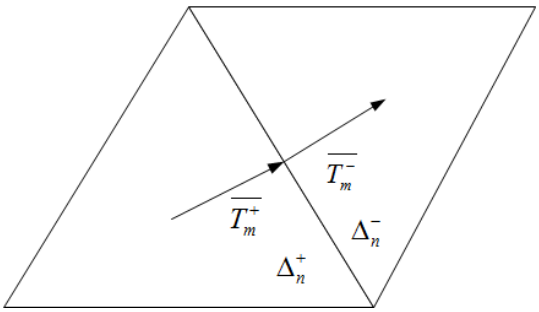

Figure 2.2: Razor blade testing function.

cell Δ_n^- is defined in a similar way, but the direction is opposite. Using the RWG basis functions, the surface current density can be approximated as:

$$\bar{J}_s \approx \sum_{n=1}^{N} I_n \bar{B}_n \tag{2.16}$$

Applying (2.11)-(2.16) to (2.9) and taking inner products with testing functions, we can obtain the EFIE:

$$\begin{aligned}\langle \bar{T}_m, \bar{E}^{inc} \rangle = jk\eta \sum_{n=1}^{N} I_n \left\langle \bar{T}_m, \iint_S \bar{B}_n \frac{e^{-jkR}}{4\pi R} dS \right\rangle \\ + \frac{jk}{\eta} \sum_{n=1}^{N} I_n \left\langle \bar{T}_m, \nabla \iint_S \left(\nabla \cdot \bar{B}_n\right) \frac{e^{-jkR}}{4\pi R} dS \right\rangle\end{aligned} \tag{2.17}$$

where the inner product between two vector functions are defined as

$$\langle \bar{f}, \bar{g} \rangle = \int \bar{f}(x) \cdot \bar{g}(x) dx \tag{2.18}$$

The testing functions used in this dissertation are the "razor-blade" testing functions ($\bar{T}_m$) [55], which are defined from the centroids of the triangular cells to the mid-point of the edge as shown in Figure 2.2.

In matrix form ($ZI = V$), elements of the system matrix are given by

$$z_{mn} = jk\eta \sum_{n=1}^{N} \left\langle \bar{T}_m, \iint_S \bar{B}_n \frac{e^{-jkR}}{4\pi R} dS \right\rangle + \frac{jk}{\eta} \sum_{n=1}^{N} \left\langle \bar{T}_m, \nabla \iint_S \left(\nabla \cdot \bar{B}_n\right) \frac{e^{-jkR}}{4\pi R} dS \right\rangle \tag{2.19}$$

and entries of the source matrix V are given by

$$v_m = \langle \bar{T}_m, \bar{E}^{inc} \rangle \tag{2.20}$$

2.3 Error Estimation and Adaptive Refinement Techniques

Adaptive refinement techniques reduce discretization errors in numerical solutions by decreasing cell sizes (h-refinement), or increasing the order of polynomials of the basis functions (p-refinement), or combining both approaches (hp-refinement) without user intervention. The main components of the adaptive refinement algorithm are an error estimator and a controller. The error estimator determines the error level within every cell of the mesh. For h-refinement, based on the information obtained from the error estimator, the control algorithm decides which cells to be refined into smaller cells while attempting to manage the quality of them (preventing their shape from becoming too skewed). Moreover, the controller contains the prescribed criterion to determine how many cells will be modified and when the refinement iterations will cease.

The error estimators must be efficient and reliable in order to achieve accurate solutions rapidly. The error estimators in electromagnetics are often based on the residuals, currents, and charges. These are explicit error estimators because they employ direct data from the numerical solutions. Botha and Davidson [27] derived and discussed residual error estimators for the finite element method (FEM), and Hsiao and Kleinman [31], [43] presented residual estimators for the method of moments. Another residual error estimator by Bibby and Peterson [50] adopted overdetermined systems, which increased the dimension of the $N \times N$ system matrix to $2N \times N$. Zienkiewicz and Zhu [53], [56], [59] proposed the superconvergent patch recovery (SPR) error estimator. "Superconvergent" implies that the errors between actual solutions and recovered solutions are proportional to the $p + \alpha$-th power of the cell size, where p is the order of basis functions and α is a positive number. If the superconvergence condition is satisfied, the recovered quantities would be chosen as good references for error estimations. Strydom and Botha [54] recovered charge densities by averaging, using the least square method and RWG basis functions. Then, they employed the recovered quantities as references in the error estimators.

Implicit error estimators divide problem domains into small sub-domains. The sub-domains typically consist of several cells sharing a common node (the sub-domain residual

method) but sometimes it is just one cell (the element residual method). Then, the estimators adopt smaller cells or increased degrees of the representation to re-solve the local problem on each sub-domain [26].

Saeed and Peterson [12] studied various error estimators, applied them to the adaptive refinement techniques for the 2D method of moments and the locally corrected Nyström method (LCN). They showed the validity of the estimators and discussed their performance. In this dissertation, we will extend their work to 3D problems, and assess the performance of various estimators by using the Pearson correlation coefficient, the local error plots, and the scatter plots.

Finite element analysis has employed error estimation for many years. Error estimators used in finite element analysis are sometimes evaluated using a global effectivity index, which is a ratio of the l^2-norm of the local error to the global error in energy norm. Local errors are obtained using the residual error estimator [11], [19] or the recovery error estimator [59]. The global error is either an exact solution or a good approximation to the exact solution. Although the effectivity index is expected to be close to 1, higher effectivity indices can also be acceptable. Researchers in [26] obtain the effectivity index, θ, by the weighted L^2-norm, which is given by

$$\theta = 1 - \frac{||\epsilon - e||_\Omega}{||e||_\Omega} \tag{2.21}$$

where ϵ is local error estimate obtained from an implicit error estimator, and e is the reference error obtained using higher order basis functions on the original mesh. $||\cdot||_\Omega$ is the weighted L^2-norm defined on the region Ω where the weight is determined based on the test cases.

In [23], the Pearson correlation coefficient and the effectivity indices were used to evaluate an implicit error estimator. Correlation coefficients and effectivity indices were computed for every adaptive refinement step to show that the implicit estimator helps the numerical solution converge to the actual solution. As we will see throughout the following chapters, however, the correlation coefficient alone is not always sufficient to assess the error estimator performance. The estimator may not always produce a good correlation with the reference error for an arbitrary test case. In the event that the correlation coefficient is

low, we need more detailed information to understand how and why the estimator failed. The correlation coefficient may have a low value because the estimator underestimated a large error or it may be low because the estimator overestimated small errors. Therefore, additional tools including the local error plot and the scatter plot are required to evaluate the error estimator.

The control algorithm of the adaptive h-refinement technique uses the input from an error estimator to refine the mesh in certain regions. Simple mesh refinement involves bisecting or trisecting triangular cells. De Cougny and Shephard [71] explained how to implement various bisection techniques for a 2D triangular mesh and a 3D tetrahedral mesh. In [26], the identified cells were divided into 4 smaller cells by adding mid-points of edges of the triangles while their adjacent cells, sharing an edge with those identified, were trisected at the centroids.

Another algorithm used to generate triangular meshes is the Delaunay triangulation. The Delaunay algorithm optimizes a triangular tessellation so that the cells do not become overly skewed in shape. Cell shapes are evaluated using the circle test, which forms a new triangular cell only when the circumscribed circle of the cell does not contain any corner node inside. There are several algorithms to achieve the Delaunay triangulation: the Bowyer-Watson algorithm, the Green-Sibson algorithm, and the advancing front Delaunay algorithm.

The Bowyer-Watson algorithm begins by adding new nodes to the initial mesh in the cells that need refinement. For each new node, the algorithm applies the circle test to the existing cells to find out which circumscribed circles of the meshes contain the node. The connectivity of the cells that are identified by the circle test are removed. Then, there remains a polygon containing the new node, and new triangular cells are created by connecting nodes of the polygon with the new node. While the Bowyer-Watson algorithm is useful for generating triangular meshes, it requires heavy computations, $\mathcal{O}(N^2)$ in the worst case [65].

The Green-Sibson algorithm is similar to the Bowyer-Watson algorithm. For a given new node, the Green-Sibson algorithm tries to find a triangle that contains the new node.

The triangle is trisected by connecting the new node with the existing nodes of the triangle. Then, the algorithm performs the circle tests for three triangular cells that are generated by the trisection. If the circumscribed circle of the new triangle contains the node of its adjacent triangular cell, then both triangles are altered by using a diagonal swapping. The Green-Sibson algorithm is successful for two-dimensional triangulation, but it demands not only the circle tests but also an algorithm that creates a triangle for each new node. Moreover, it is reported that the algorithm can fail in the three-dimensional situation [65].

The advancing front Delaunay triangulation is a reversal of the previous Delaunay triangulation algorithms. It provide an intuitive and simple idea for generating triangular meshes [65][67]. The advancing front approach adds new nodes to cells in a region needing refinement and removes the existing edges from those cells. This results in a polygon consisting of multiple edge segments and multiple interior nodes. The set of the edge segments is called a front. The algorithm picks one edge of the front and one node inside or on the polygon. It assumes a triangle formed by the end-points of the selected edge and the selected node. Then, it performs the circle test on that triangle. When the circumscribed circle of the triangle contains some other node, then that triangle is discarded and another triangle is formed using the same edge and a different interior node. If the circle test succeeds, the new triangle is accepted and added to the mesh. The algorithm then removes the original selected edge from the front and adds appropriate edges of the new triangle to the front. The algorithm repeats these steps until all edge segments are removed from the front.

Mesh refinement can result in cells of highly elongated shape, which may produce a numerical solution with poor accuracy. Cell shape can be characterized by a triangle "quality" factor. The triangle quality factor is defined as the ratio of the radius of the inscribed circle of the triangle to the radius of the circumscribed circle. Since an equilateral triangle is considered ideal, the radii ratio is multiplied by 2 to normalize the quality factor. To avoid producing a poor quality mesh, the adaptive refinement technique often includes another step where cell shapes are adjusted to improve their quality factor. This process is known as "mesh smoothing." The most fundamental algorithm for enhancing the mesh quality is Laplacian smoothing. Laplacian smoothing employs a very simple algorithm: it adjusts the

position of a given node by taking the average of its adjacent nodes [74].

Other techniques have been proposed for mesh smoothing. In [68], improved mesh quality is achieved by using the steepest descent smoothing technique. An objective function is defined as the product of the quality factors of all the cells in the mesh. The steepest decent smoothing algorithm uses gradients of the objective function to adjust a node position. Persson and Strang [46] employed the "tension force" algorithm to enhance the mesh quality. They modeled the mesh as a network of springs and varied node positions until the spring system reached an equilibrium status. Although these algorithms produce better quality meshes than Laplacian smoothing, they require additional cost to find an optimized node position.

CHAPTER III

ERROR ESTIMATION IN THE METHOD OF MOMENTS

3.1 Introduction

Error estimation is an important component in the adaptive refinement process. It is essential to identify domains with large errors and it is useful to determine the rate of convergence of numerical solutions when the mesh size is reduced or the basis function's order is increased. A good error estimator is required to be reliable and efficient, because an inaccurate and inefficient estimator will add cost to the solution process and may lead to poor results.

Local error estimators are roughly categorized into explicit error estimators and implicit error estimators. An explicit error estimator employs the numerical solution itself to evaluate local errors. For instance, the estimator may measure the discontinuity of the numerical current density or charge density between adjacent cells, or it calculates residuals from the solution by applying a different boundary condition than the one used to obtain the original solution, or it computes a smoother numerical solution to determine regions where there is a large difference between the original and smoothed result. On the other hand, an implicit error estimator decomposes a global problem into a large number of local problems and re-solves them with a different discretization to determine how much they change. A large local change suggests that the result has not yet converged in that region and requires refinement there. Local problems can involve a single cell or several cells. The former is called the element residual method, and the latter is called the sub-domain residual method.

In the following sections, reference local errors are defined for various problems to assess several local error estimators. If a problem has a theoretical solution, exact current densities are directly compared with numerical current densities. Such examples include a spherical cavity and a cylindrical cavity. For the purpose of evaluating various estimators, we use interior problems of this type rather than exterior problems. For other problems, such as a

plate, a torus, and a NASA almond, numerical current densities obtained by finer meshes are used for reference solutions. Then, local error estimators are introduced including discontinuity error estimators, residual error estimators, a charge recovery error estimator, and an implicit error estimator. Each estimator will be illustrated and some of numerical results are shown.

3.2 Reference Error

In order to evaluate reliability of the given error estimators, we need to introduce a number of test problems and identify reference local errors for each problem. Geometries of the test problems considered throughout this research are shown in Fig. 1 and all scatterers are assumed to be perfect electric conductors (PECs).

The first two examples (see Fig. 3.1(a) and Fig. 3.1(b)) are spherical- and cylindrical cavity problems where exact solutions are already known. There is a point source inside each cavity and it is close to the surface of the cavity so as to induce gradients in the currents nearby. The point source can be either electric current density or magnetic current density and can have different polarizations. Theoretical field quantities for both cavity problems can be obtained by using a Dyadic Green's function [9].

The dyad is a mathematical operator using two vector notations. In electromagnetics, the first vector denotes the field polarization and the other one is related to the source polarization. For example, let an electric field be generated by an electric current $\bar{J} = \hat{x}J_x + \hat{y}J_y + \hat{z}J_z$. Then, the dyadic function of the electric field, $\bar{\bar{E}}$, can be expressed as:

$$\begin{aligned}\bar{\bar{E}} = {} & \hat{x}'\hat{x}E_{x'x} + \hat{x}'\hat{y}E_{x'y} + \hat{x}'\hat{z}E_{x'z} \\ & + \hat{y}'\hat{x}E_{y'x} + \hat{y}'\hat{y}E_{y'y} + \hat{y}'\hat{z}E_{y'z} \\ & + \hat{z}'\hat{x}E_{z'x} + \hat{z}'\hat{y}E_{z'y} + \hat{z}'\hat{z}E_{z'z} \end{aligned} \tag{3.1}$$

where primed vectors involve the source current and unprimed vectors correspond to the field components. If we take a dot product of $\bar{\bar{E}}$ and $\hat{x}'$, for instance, then it gives the electric field generated by J_x. On the other hand, taking a dot product of $\bar{\bar{E}}$ and $\hat{x}$ results in x-component of the electric field caused by $\bar{J}$. Detailed derivations of the dyadic Green's

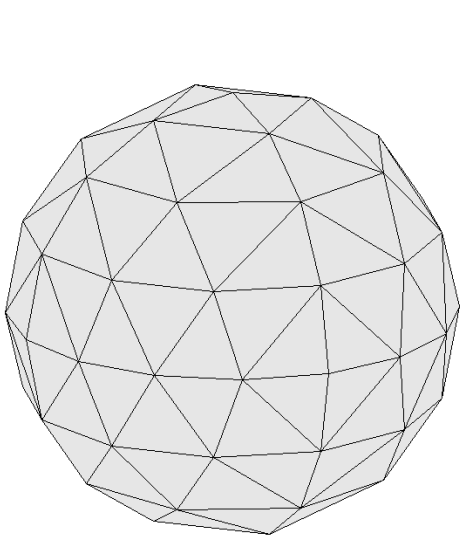

(a) A PEC spherical cavity

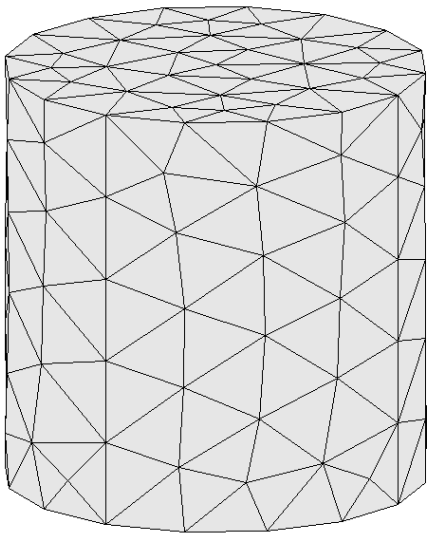

(b) A PEC cylindrical cavity

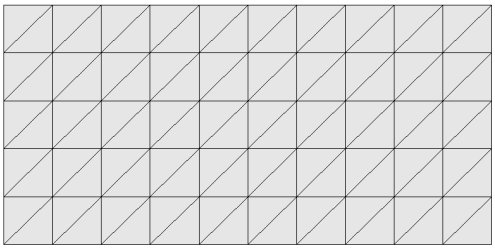

(c) A PEC plate

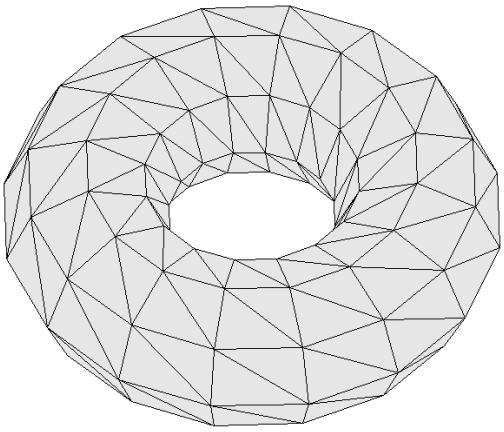

(d) A PEC torus

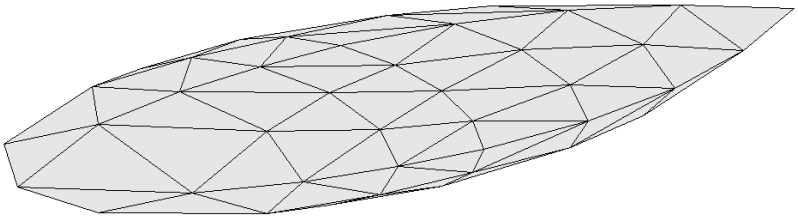

(e) A PEC NASA almond

Figure 3.1: Geometries of the testing problems.

functions for both cavity problems are shown in [9], and the dyadic Green's functions and the reference surface current densities of the spherical- and cylindrical cavities are summarized in Appendix I.

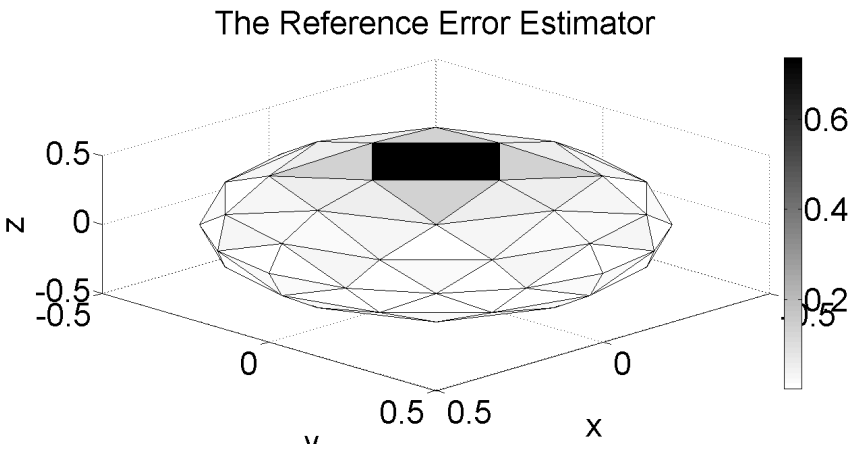

(a) Reference error of the PEC spherical cavity whose radius is 0.5λ.

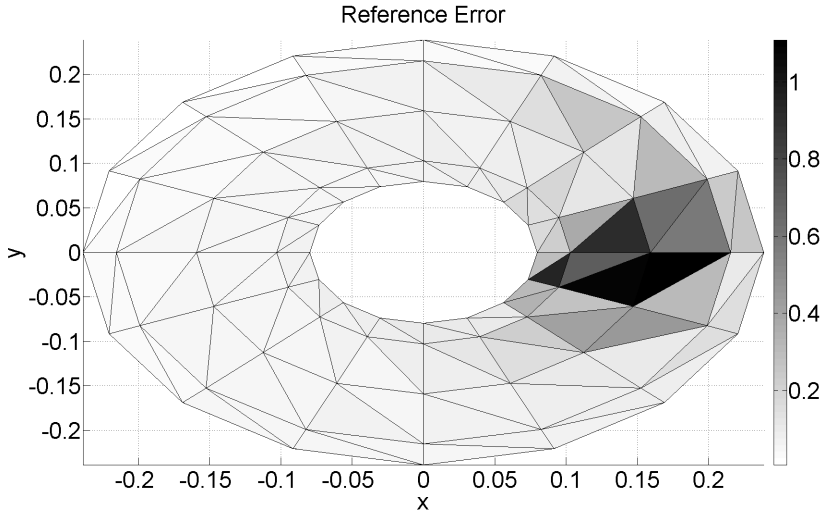

(b) Reference error of the PEC torus where major radius is $(1/2\pi)\lambda$ and minor radius is $(1/4\pi)\lambda$.

Figure 3.2: Local error plot of the reference error when a z-polarized electric point source is closely placed around the PEC surface.

For the other problems where exact solutions do not exist (see Fig. 3.1(c)-(e)), the original meshes are subdivided into 4 smaller meshes and the reference current densities are obtained by solving the finer mesh problems. Then, the local reference error at the i-th mesh ($i = 1, 2, \ldots, N$) is defined by

$$\mathrm{LE}^i_{\mathrm{ref}} = \frac{\left|\bar{J}^i_{\mathrm{ref}} - \bar{J}^i_{\mathrm{MoM}}\right|}{\max_i \left|\bar{J}^i_{\mathrm{ref}}\right|} \tag{3.2}$$

where $\bar{J}^i_{\mathrm{ref}}$ and $\bar{J}^i_{\mathrm{MoM}}$ are the reference surface current and the numerical solution sampled at the centroid of the i-th mesh, respectively.

Some reference local errors are shown in Fig. 3.2. Figure 3.2(a) is the reference error of

the spherical cavity when its radius is 0.5λ and a z-polarized electric point source is placed on the z axis. The point source and the surface of the sphere are separated by 0.05λ in order to induce a large gradient in the current density around the North pole. Because of the inability of the numerical technique to represent the rapid change in the current, there is a relatively large error in that region. Large local error meshes are represented by shaded regions in Fig. 3.2 while bright regions imply low errors. Figure 3.2.(b) shows the reference local errors of the PEC torus with major radius $b = (1/2\pi)\lambda$ and minor radius $a = (1/4\pi)\lambda$. A z-polarized electric point source is located on the top of the torus. The distance between the source and the surface of the torus is $(1/4\pi)\lambda$. As we intended, mesh cells close to the point source have large errors and errors decrease as an observer moves away from the source.

3.3 Discontinuity Error Estimator

In a numerical solution, discretization error is likely to be large where a geometry of interest has corners and edges or where sources are placed closely to it. The magnitude of field quantities including the electric field, surface current density, and surface charge density in such domains are larger than those in smooth regions, and the rate of change of them is rapid. Thus, error tends to be larger in such a region.

As discussed in Chapter 2, the RWG basis function only enforces the normal continuity between two adjacent cells, but tangential continuity is not guaranteed in general. Hence, the surface current density and the surface charge density obtained from the RWG basis functions will have jump discontinuities between two neighboring cells and, in particular, the discontinuities will be relatively large around edges, corners, and sources. Moreover, in the actual problem, both normal and tangential components of the surface current density and the surface charge density have to be continuous over a given geometry unless there exists external sources on some points, lines, and surfaces of the geometry or the geometry is not continuous. Thus, certain domains having large discontinuous current- and charge densities imply large numerical errors.

Therefore, calculating the current or/and charge discontinuity between adjacent cells in

a surface mesh will provide a good estimation of the local discretization errors. We call these a "current discontinuity error estimator" or a "charge discontinuity error estimator" based on which field quantities are evaluated. The discontinuity error estimators benefit from simple implementation and good efficiency, but can be inaccurate for certain problems. The overall accuracy of the discontinuity error estimators will be improved by using combined discontinuity error estimators in Chapter 5.

3.3.1 Current Discontinuity Error Estimator

For a given cell, the current discontinuity error estimator evaluates jump discontinuities in the numerical solution at the mid-point of edges of each cell. Then, the estimator averages the values obtained at all edges of each cell. Since the geometry is discretized into triangular cells, the local error estimator of the i-th cell can be written by

$$\mathrm{LE}^i_{J\tan} = \frac{\sum_{m=1}^{3} \left| \hat{t}_m \cdot \left(\bar{J}^i - \bar{J}^{n(i,m)} \right) \right|}{3 \max_i \left| \bar{J}^i \right|} \tag{3.3}$$

where the superscript i denotes the index of the given cell, m is the local index of edges of the i-th cell, and $n(i,m)$ indicates the neighbor cell of the m-th edge of the i-the cell.

Examples of local error plots obtained by the current discontinuity error estimator are shown in Fig. 3.3. Source types, source positions, source polarizations and geometry dimensions are identical to those in Fig. 3.2. For the spherical cavity, the current discontinuity estimator failed to find large local errors right at the North pole. This occurs when current discontinuities around the North pole are canceled by symmetry in the mesh geometries and characteristics of the point source. Detailed analysis about the estimator's failure will be presented in Chapter 5. For the PEC torus, however, the current discontinuity estimator assesses the large local error domain correctly.

3.3.2 Charge Discontinuity Error Estimator

The charge discontinuity error estimator is defined similar to the current discontinuity error estimator except that it evaluates discontinuities of the surface charge density across cell boundaries. The local error of the estimator is given by:

$$\mathrm{LE}^i_{\rho} = \frac{\sum_{m=1}^{3} \left| \rho^i - \rho^{n(i,m)} \right|}{3 \max_i \left| \rho^i \right|} \tag{3.4}$$

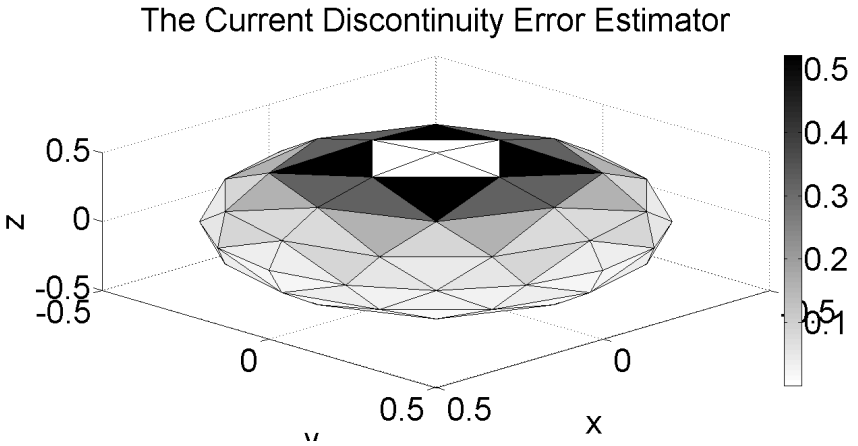

(a) Local error of the current discontinuity error estimator for the PEC spherical cavity whose radius is 0.5λ.

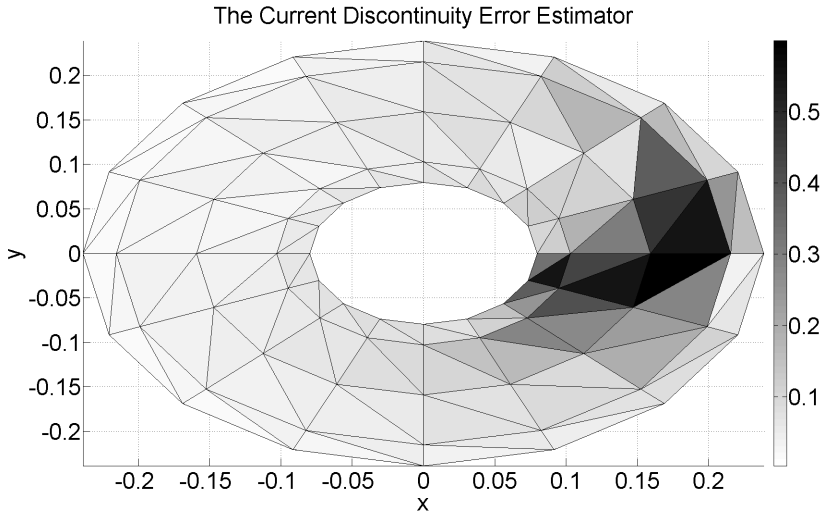

(b) Local error of the current discontinuity error estimator of the PEC torus where major radius is $(1/2\pi)\lambda$ and minor radius is $(1/4\pi)\lambda$.

Figure 3.3: Local error plots obtained by the current discontinuity error estimator when a z-polarized electric point source is closely placed around the PEC surface.

Superscripts and subscripts are identical to those defined in the current discontinuity error estimator.

Figure 3.4(a) shows local errors of the spherical cavity acquired by the charge discontinuity error estimator. The estimator recognizes mesh cells around the North pole as large error domains, but not in the same proportions as the reference error. The same goes for the PEC torus shown in Fig. 3.4(b). This implies if we use the charge discontinuity estimator and want to refine the mesh around the North pole, then four additional cells will be included in the adaptive refinement process. That will increase computational costs and,

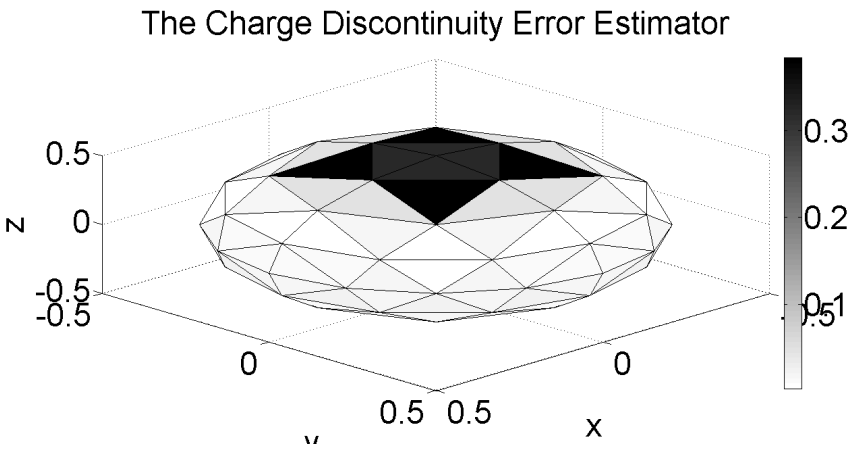

(a) Local error of the charge discontinuity error estimator for the PEC spherical cavity whose radius is 0.5λ.

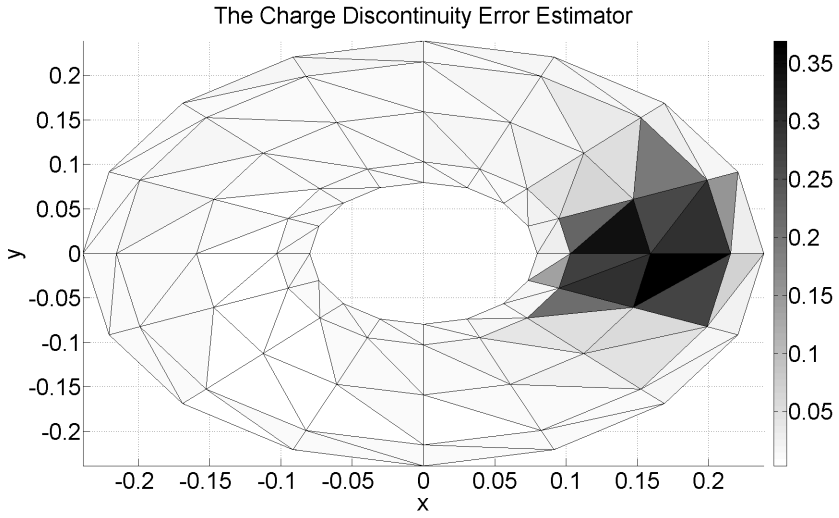

(b) Local error of the charge discontinuity error estimator of the PEC torus where major radius is $(1/2\pi)\lambda$ and minor radius is $(1/4\pi)\lambda$.

Figure 3.4: Local error plots obtained by the charge discontinuity error estimator when a z-polarized electric point source is closely placed around the PEC surface.

therefore, slow down the process.

3.4 Residual Error Estimator

Residual-based error estimators are often used in computational electromagnetics. The residual error estimator proved its validity for the finite element method (FEM) [27] and the method of moments [31], [43] when a Galerkin testing function is used. Despite of its robustness, the residual estimator is known for heavy computational cost because it requires a computation comparable to a matrix fill and often extensive use of numerical quadrature.

Two kinds of residual type estimators will be discussed in this section. The first is a tangential residual error estimator based on the tangential boundary condition for the electric field. The other estimator is a normal residual error estimator, which is based on the normal boundary condition for the magnetic field on the PEC.

3.4.1 Tangential Residual Error Estimator

In Chapter 2, razor-blade test functions are used with the electric field integral equation, to impose the boundary condition for the tangential electric field on the PEC surface. In other words, using the razor-blade functions forces residuals in (2.4) to be zero in certain directions and points. If the RWG basis functions can completely represent the surface current density, then applying other test functions or boundary conditions will result in zero residuals. However, the numerical surface current density is not correct in general. Hence, residuals obtained from different test functions or boundary conditions can serve as a good error estimator.

In this work, a residual error is obtained by employing razor-blade test functions in an independent location (having the same direction but scaled and shifted) from those used to produce the original solution. The test function used for the tangential residual estimator is shown in Fig. 3.5. A residual error estimator using the same EFIE and scaled and shifted test functions can be easily implemented because it is identical to the original MoM algorithm. Since the estimator takes advantage of the boundary condition for the tangential electric field, it is called the "tangential residual" error estimator.

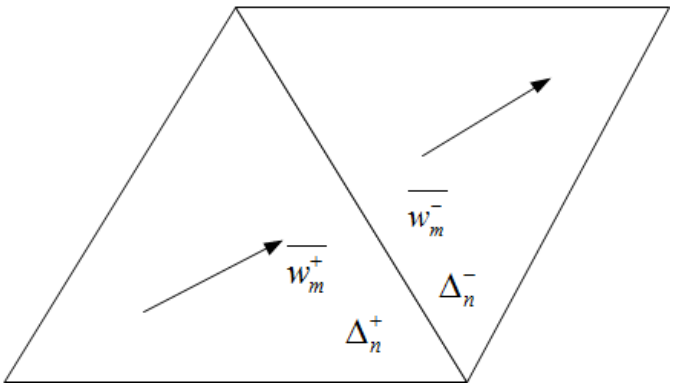

Figure 3.5: Testing functions for the tangential residual error estimator.

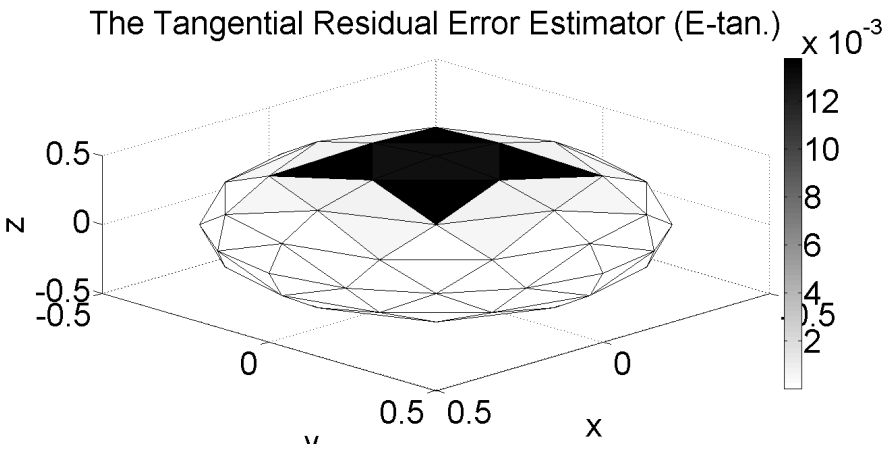

(a) Local error of the tangential residual error estimator for the PEC spherical cavity whose radius is 0.5λ.

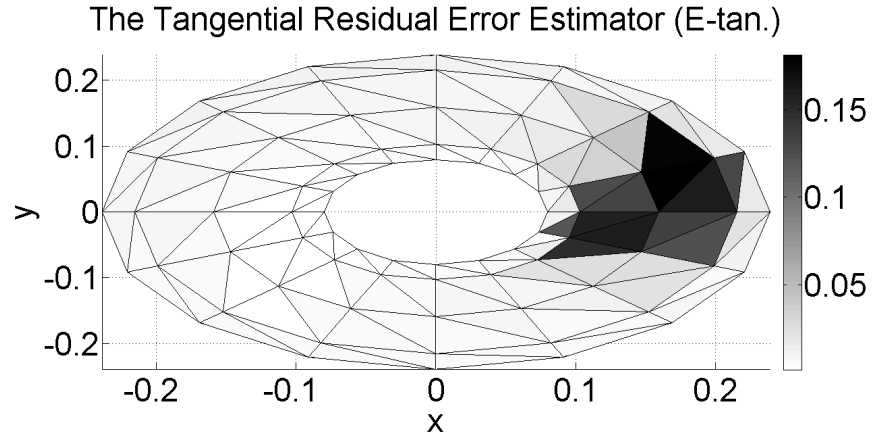

(b) Local error of the tangential residual error estimator of the PEC torus where major radius is $(1/2\pi)\lambda$ and minor radius is $(1/4\pi)\lambda$.

Figure 3.6: Local error plots obtained by the tangential residual error estimator when a z-polarized electric point source is closely placed around the PEC surface.

As in the discontinuity estimators, the local errors obtained with the tangential residual estimator at the edges of the i-th cell are averaged to produce one cell-based error estimate. The local errors are given by:

$$\mathrm{LE}^i_{E\tan} = \frac{\sum_{m=1}^{3} \left| \langle \bar{w}^i_m, \bar{E}^{tot} \rangle \right|}{3 \max_i \left| \bar{E}^{inc} \right|} \tag{3.5}$$

where $\bar{w}^i_m$ is the scaled and shifted test function at m-th edge of the i-th mesh, and $\bar{E}^{tot} = \bar{E}^{inc} + \bar{E}^s$ is the total electric field.

Figure 3.6 shows local error plots for the spherical cavity and the torus when using the tangential error estimator. It is interesting to note that shaded regions determined by the estimator resemble those of the charge discontinuity error estimator. For the sphere test

problem, the tangential residual estimator includes some mesh cells with relatively low errors, which demands more computations. The correlation between the charge discontinuity error estimator and the tangential residual error estimator will be studied in Chapter 4.

3.4.2 Normal Residual Error Estimator

Another residual error estimator can be built by using the magnetic-field integral equation (MFIE), and the PEC boundary condition for normal component of the magnetic field:

$$\hat{n} \cdot \left(\bar{H}^{inc} + \int_S \bar{J}(\bar{r}') \times \nabla' G(\bar{r}, \bar{r}') dS' \right) = 0 \tag{3.6}$$

where the integral in (3.6) is a scattered magnetic field and primed vectors are with respect to the source.

The integral in (3.6) needs to be treated specially when source points overlap with observation points. Using an integral formula in [29], it becomes:

$$\int_S \bar{J}(\bar{r}') \times \nabla' G(\bar{r}, \bar{r}') dS' = \bar{J} \times \bar{T} + \int_{S_o} \bar{J}(\bar{r}') \times \nabla' G(\bar{r}, \bar{r}') dS' \tag{3.7}$$

where S_o consists of mesh cells that are not overlapping with the source cell and $\bar{T}$ is a closed line integral along the source cell and is tangent to the surface (see Fig. 3.7). The

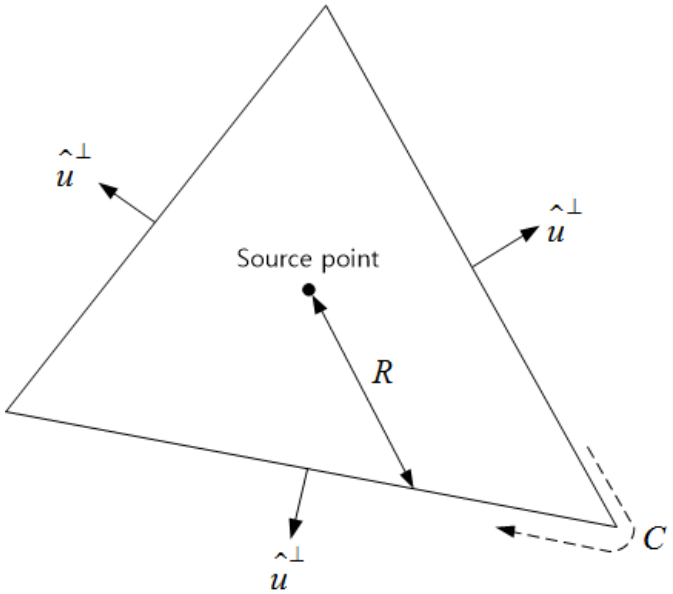

Figure 3.7: A line integral when a source cell and an observation cell overlap.

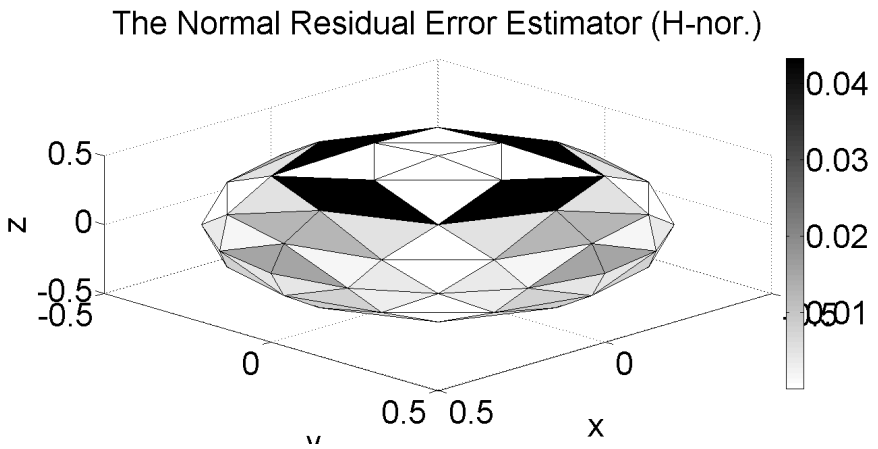

(a) Local error of the normal residual error estimator for the PEC spherical cavity whose radius is 0.5λ.

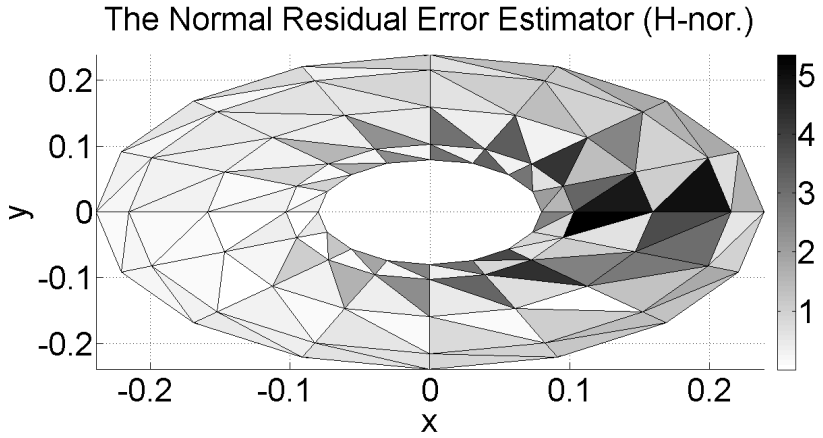

(b) Local error of the normal residual error estimator of the PEC torus where major radius is $(1/2\pi)\lambda$ and minor radius is $(1/4\pi)\lambda$.

Figure 3.8: Local error plots obtained by the normal residual error estimator when a z-polarized electric point source is closely placed around the PEC surface.

line integral is given by:

$$\bar{T} = \oint_C \frac{\hat{u}^{\perp}}{4\pi R} dl \tag{3.8}$$

The unit vector $\hat{u}^{\perp}$ is normal to the path C and R is the distance between the source point and any points on the path C.

The local error of i-th cell is defined as

$$\mathrm{LE}^{i}_{H_{\mathrm{nor}}} = \frac{\left|\hat{n}^{i} \cdot \bar{H}^{\mathrm{tot}}\right|}{\max_i \left|\bar{H}^{inc}\right|} \tag{3.9}$$

where $\hat{n}^i$ is the normal unit vector with respect to the i-th cell and $\bar{H}^{tot}$ is the total magnetic field.

Local error plots of the "normal residual" error estimator are shown in Fig. 3.8. The normal residual estimator failed to determine some large local error cells for the spherical cavity, perhaps because of symmetries imposed by the mesh and source position. Furthermore, the normal residual estimator reports large errors for many cells on the torus where the actual error is small. One possible reason for the poor performance of the estimator is that the test function at the i-th mesh, $\hat{n}^i$, samples only one value at the centroid of the mesh.

3.5 Charge Recovery Error Estimator

Many electromagnetic simulation tools provide post-processing procedures that recover quantities of interest from the original solution. For example, one might want to obtain the charge density, which involves the divergence of electric fields. The charge density obtained by the MoM is generally a discontinuous approximation to its true values because the RWG basis functions are only linear in order. An improved approximation for the discontinuous charge can be "recovered" by smoothing the numerical results. Under certain conditions, the recovered quantities are closer to the true quantities than the original solutions as mesh size decreases. Hence, the recovered solutions can serve as a reference solution and can be used for local error estimation.

From a mathematical standpoint, the relation between the recovered solution and the true solution is guided by the consistency condition, localization condition, bounded and linearity conditions, and the superconvergence property [11]. Roughly speaking, the consistency condition implies if the true values are polynomials, the recovery procedure must reproduce them exactly. The localization condition requires that recovered quantities at certain point only depend on true values sampled around that point. Boundedness and linearity conditions state that the recovery procedure, or the recovery operator must be linear and bounded. Finally, the superconvergence property demands that the solutions obtained from the method of moments converge to the interpolations of the true values as cells decrease. Strict conditions, properties and their derivations are shown in [11].

Then, the next task is to construct a recovery operator that satisfies above conditions.

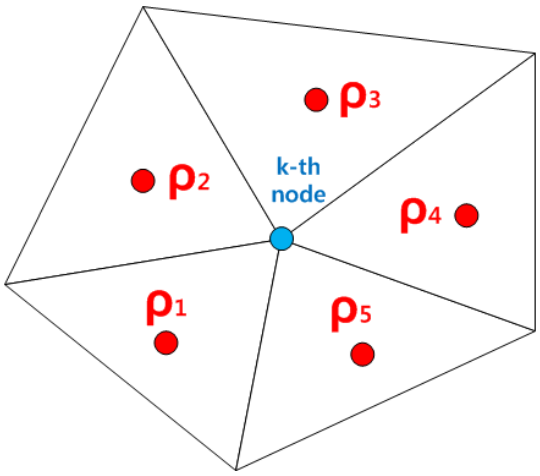

Figure 3.9: A group of cells sharing a node.

One of the methods is called superconvergent patch recovery (SPR), which was developed by Zienkiewicz and Zhu [53], [56], [59]. Consider a node of the mesh, say the k-th node, and cells sharing the node as shown in Fig. 3.9. The SPR defines a surface charge density at the k-th node by averaging charge densities, ρ_i, sampled at the centroids of the neighboring cells.

$$\rho_k = \frac{1}{n}\sum_{i=1}^{n}\rho_i \tag{3.10}$$

With averaged node charge densities and the Lagrangian basis functions, the reconstructed charge density is given by

$$\rho_{\text{recovery}} = \sum_{k=1}^{N}\rho_k\theta_k(\bar{r}) \tag{3.11}$$

where θ_k is the Lagrangian basis function with respect to the k-th node.

The charge recovery error estimator for the i-th cell evaluates the difference between the recovered charge density and numerically computed charge density, according to

$$\text{LE}^i_{\text{Recovery}} = \frac{\sqrt{\int_{S_i}|\rho_{\text{recovery}}-\rho_i|\,dS_i}}{\max_i\sqrt{\int_{S_i}|\rho_i|\,dS_i}} \tag{3.12}$$

where ρ_{recovery} is the recovered charge density at i-th mesh, ρ_i is the charge density of the MoM, and S_i represents the surface of the i-th cell in the mesh.

Results from the charge recovery error estimator are shown in Fig. 3.10. Large error domains identified by the charge recovery estimator resemble those obtained by the charge

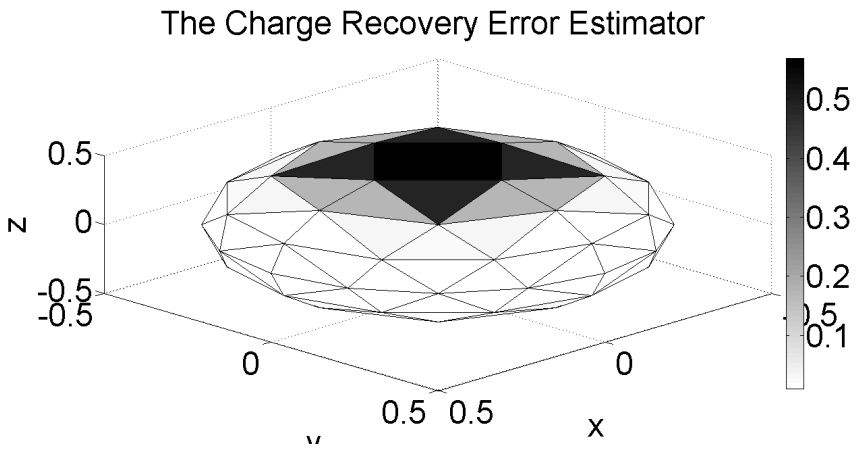

(a) Local error of the charge recovery error estimator for the PEC spherical cavity whose radius is 0.5λ.

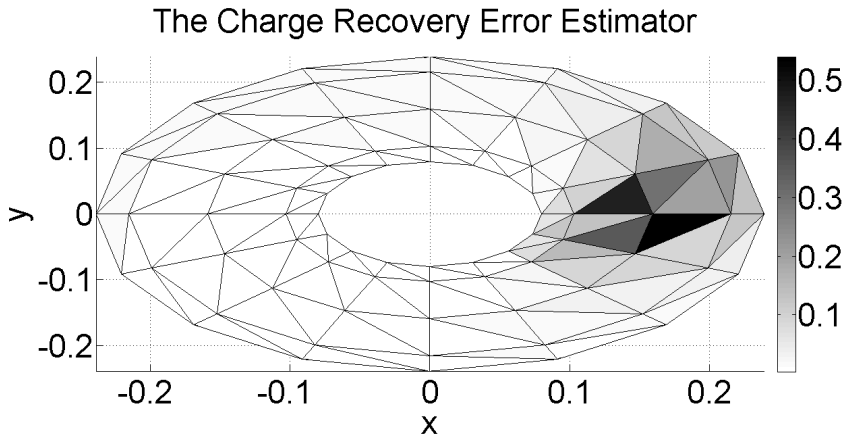

(b) Local error of the charge recovery error estimator of the PEC torus where major radius is $(1/2\pi)\lambda$ and minor radius is $(1/4\pi)\lambda$.

Figure 3.10: Local error plots obtained by the charge recovery error estimator when a z-polarized electric point source is closely placed around the PEC surface.

discontinuity error estimator and the tangential residual error estimator. Unlike the tangential residual estimator, the similarity between the charge recovery estimator and the charge discontinuity estimator is expected and can be explained.

Since node-based Lagrangian basis functions are used to construct the recovery charge density, the recovered charge density at a point in the i-th mesh is just a weighted sum of the surrounding node charge densities. Cells around a central node usually contain different charge densities, and if their difference are large, then the recovered charge density is likely to deviate considerably from the original charge density. Therefore, cells where differences between recovered charge densities and original charge densities are large tend to be those

with large surface charge discontinuities.

3.6 Implicit Error Estimator

The computational solutions in electromagnetics usually become more accurate when refining meshes or increasing the polynomial order of basis functions. The order of error is given by $\mathcal{O}(\Delta^{p+1})$, where Δ is cell size and p is the polynomial order of basis functions. Some error estimators in [12], and [26] used this property. They selected subsets of cells and used higher order basis functions to represent the surface current density. With appropriate boundary conditions, they re-solved the given problems, and local error estimates were achieved by comparing the new solutions with original solutions.

In this section, a similar implicit error estimator will be introduced based on h-refinement. When the original result has small local error, the solutions obtained with finer cells will not change much from the original solutions. On the other hand, the surface current on a large error cell (i.e., close to sources or edge singularities) would vary greatly when the cell is split into finer meshes and re-solved. Thus, a solution obtained with a refined mesh will change significantly if the original error tends to be large.

In the proposed estimator, which works with one original cell at a time, each cell is

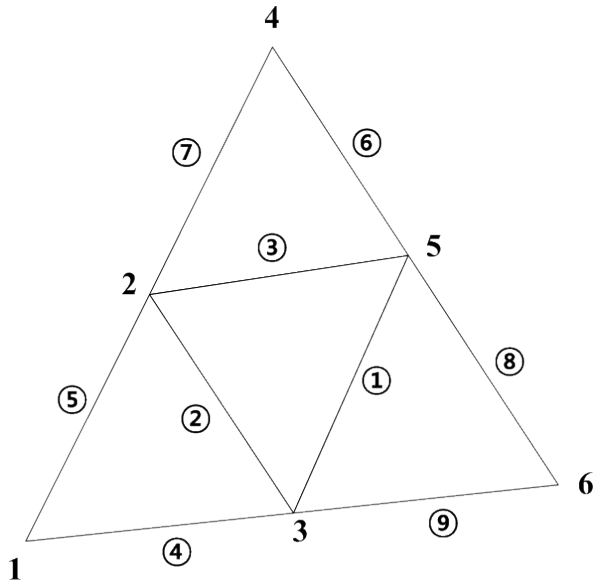

Figure 3.11: A scheme of the implicit error estimator.

divided into four smaller cells. In Fig. 3.11, local mesh and edge indices are depicted as numbers and circled numbers, respectively. Each edge of the refined mesh corresponds to the location of an RWG basis function as defined in in (2.15) and a new coefficient. Thus, there are 9 basis functions required to represent the surface current density over the mesh subset. For the edges labeled ①, ②, and ③, the coefficients are unknown and will be determined by a solution of the EFIE. The coefficients of basis functions for edges ④-⑨ will be kept the same as those on the original mesh by matching them with the original solutions.

If the current densities are matched at the mid-points of edges in finer cells, the system matrix for the cell in Fig. 3.11 can be obtained as

$$\begin{bmatrix} Z_{11} & Z_{12} & Z_{13} & Z_{14} & Z_{15} & Z_{16} & Z_{17} & Z_{18} & Z_{19} \\ Z_{21} & Z_{22} & Z_{23} & Z_{24} & Z_{25} & Z_{26} & Z_{27} & Z_{28} & Z_{29} \\ Z_{31} & Z_{32} & Z_{33} & Z_{34} & Z_{35} & Z_{36} & Z_{37} & Z_{38} & Z_{39} \\ 0 & 0 & 0 & \bar{t}_4 \cdot \bar{B}_4 & 0 & 0 & 0 & 0 & 0 \\ 0 & 0 & 0 & 0 & \bar{t}_5 \cdot \bar{B}_5 & 0 & 0 & 0 & 0 \\ 0 & 0 & 0 & 0 & 0 & \bar{t}_6 \cdot \bar{B}_6 & 0 & 0 & 0 \\ 0 & 0 & 0 & 0 & 0 & 0 & \bar{t}_7 \cdot \bar{B}_7 & 0 & 0 \\ 0 & 0 & 0 & 0 & 0 & 0 & 0 & \bar{t}_8 \cdot \bar{B}_8 & 0 \\ 0 & 0 & 0 & 0 & 0 & 0 & 0 & 0 & \bar{t}_9 \cdot \bar{B}_9 \end{bmatrix} \begin{bmatrix} I_1 \\ I_2 \\ I_3 \\ I_4 \\ I_5 \\ I_6 \\ I_7 \\ I_8 \\ I_9 \end{bmatrix} = \begin{bmatrix} V_1 \\ V_2 \\ V_3 \\ \bar{t}_4 \cdot \bar{J}_4 \\ \bar{t}_5 \cdot \bar{J}_5 \\ \bar{t}_6 \cdot \bar{J}_6 \\ \bar{t}_7 \cdot \bar{J}_7 \\ \bar{t}_8 \cdot \bar{J}_8 \\ \bar{t}_9 \cdot \bar{J}_9 \end{bmatrix} \tag{3.13}$$

where I_m $(m = 1, 2, \ldots, 9)$ are unknown variables, Z_{mn} and V_m are defined as in (2.19) and (2.20), and $\bar{B}_m$ and $\bar{t}_m$ $(m = 4, 5, \ldots, 9)$ are the basis functions and test functions for edges ④-⑨, respectively. Since the surface current density $\bar{J}_i$ is defined along the i-th edge, the original current density at this edge has two distinct values. The first value of the current density is from the original mesh in Fig. 3.12 and the other is from its adjacent mesh. Hence, we obtain $\bar{J}_i$ by averaging these current densities. The testing functions and the surface current densities are shown in Fig. 3.12.

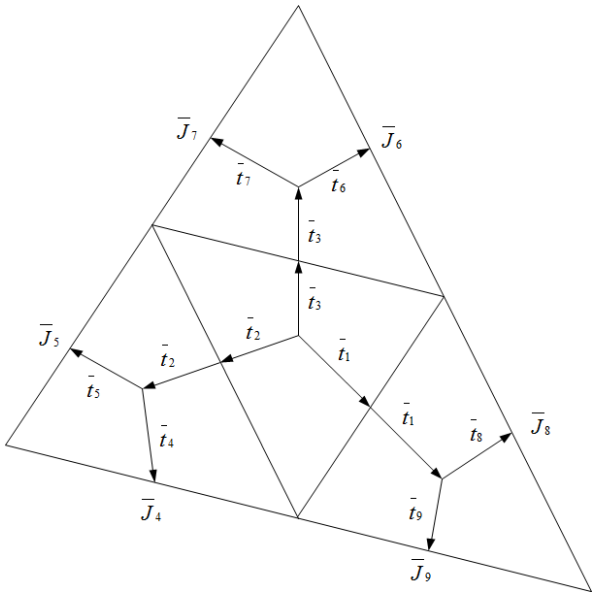

Figure 3.12: Testing functions of the implicit error estimator.

The local error of the implicit estimator at the i-th cell is given by

$$\mathrm{LE}^i_{J_{\mathrm{imp}}} = \frac{\left|\bar{J}^i_{\mathrm{imp}} - \bar{J}^i_{MoM}\right|}{\max_i \left|\bar{J}^i_{\mathrm{imp}}\right|} \tag{3.14}$$

where J_{imp} is locally re-solved surface current density obtained by inverting (3.13), and $\bar{J}_{MoM}$ is the current density of the original MoM solution.

Local error plots for the spherical cavity and the torus are shown in Fig. 3.13. For these examples, the implicit estimator accurately identifies large error domains. In particular, the local error plot of the implicit estimator for the spherical cavity is almost same as that of the reference error.

3.7 Concluding Remarks

This chapter introduced various error estimators that can be used with numerical solution of the EFIE. The error estimators employed discontinuities of field quantities, residuals, smoothed original solutions, and locally re-solved solutions. Scatterers such as a PEC sphere and a PEC torus were used to test the estimators. A point source is placed near the surface of each problem so as to induce large local errors.

To compare the performance of the error estimators, a reference local error was defined. For the spherical- and cylindrical cavity problems, the exact surface current density can be

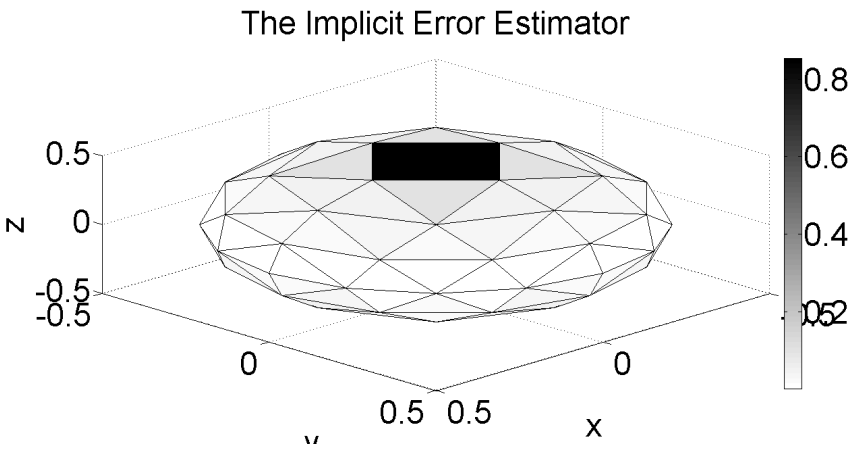

(a) Local error of the implicit error estimator for the PEC spherical cavity whose radius is 0.5λ.

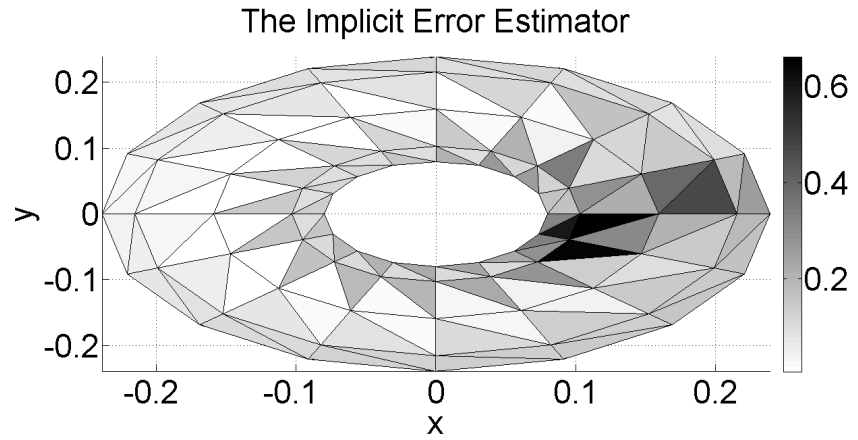

(b) Local error of the implicit error estimator of the PEC torus where major radius is $(1/2\pi)\lambda$ and minor radius is $(1/4\pi)\lambda$.

Figure 3.13: Local error plots obtained by the implicit error estimator when a z-polarized electric point source is closely placed around the PEC surface.

found by using the Dyadic Green's functions. For the other problems, solutions obtained by finer meshes were chosen as the reference because they do not have theoretical solutions in general.

The discretized error tends to be large in regions where current and charge change rapidly because of insufficient representation of their behaviors. The discontinuity error estimators utilize this property as well as the tangential discontinuity of the RWG basis function. The discontinuity estimators are easily implemented, and demand less computational cost, but they failed to identify large local error regions for some cases. Analysis of this failures and enhancement of the discontinuity estimators will be dealt with in Chapter 5.

The residual error estimators are known to be robust but expensive error estimators. The tangential residual error estimator based on the boundary condition of tangential electric field on the PEC objects provides simple implementation and moderate accuracy of error estimation, but it requires the same amount of computation as it takes to produce the original MoM system of equations. However, the examples given in this chapter imply that there is a correlation between the tangential residual estimator and the charge discontinuity estimator. The normal residual error estimator, however, showed poor performance in determining large error domains for the spherical cavity problem.

Processing the surface charge density to remove its discontinuity can be a good reference and can be used to produce an error estimator. The smoothed charge density is referred to as a "recovered" charge density. The charge recovery error estimator evaluates local errors by taking a difference between the smooth version of the charge density and the one obtained by the MoM. The difference becomes greater when meshes used to obtain the recovered charge density contain a large charge discontinuity. Hence, local errors identified by the charge recovery estimator resemble those detected by the charge discontinuity error estimator.

Another type of estimator, called an implicit error estimator, is obtained from a locally re-solved surface current density. The implicit error estimator works with one cell of the mesh at a time. That cell is divided into four smaller cells and a new solution is obtained from the EFIE on the subdomain. The error is estimated in proportion to the amount of change between the original and refined solutions. The implicit error estimator accurately detected large error regions for both the spherical cavity and the torus problems.

CHAPTER IV

EVALUATION OF ERROR ESTIMATORS

4.1 Introduction

In this chapter we evaluate the performance of the error estimators introduced in Chapter 3. The key features in error estimation are accuracy and efficiency. When used for adaptive refinement, an error estimator must accurately evaluate local errors to properly identify cells that benefit from a reduction in size or an increase in basis order. Efficiency of the error estimator is also important, since flagging unnecessary cells results in additional computation in the adaptive refinement process. In addition, the computational cost of an error estimator must be cheap enough that the total cost of the adaptive refinement is much lower than a non-adaptive, global refinement.

Adaptive refinement is a process where either a given problem's model or mesh is refined in places where error is high (h-refinement), or the polynomial degree of the representation in certain cells is increased (p-refinement), or both. The procedure usually begins with an initial numerical solution obtained using a relatively coarse mesh, from which an error estimate is determined. Cells in the mesh exhibiting error levels that exceed a prescribed error criterion are identified. The error criterion may be adjusted based on the type of estimator in use or the type of problem. Often, the error criterion is defined as some percentage of the maximum error value measured by the estimator. For instance, the adaptive refinement may flag mesh cells whose errors are greater than 50% of the maximum local error.

Ideally, an error estimator should have linear relationship with the true error or *reference* error. To illustrate, let a reference error set be X, and a local error estimate set be Y. Further, assume that the two sets have a quadratic relation, i.e., $Y = X^2$. The performance of the error estimator appears to be good simply because it can sort out error values in the same order of the reference values. However, the number of mesh cells identified by the

error estimator will generally be different from those with a reference error level exceeding the same criterion. If the error criterion is set to be 50% of the maximum local error, some of cells that should be flagged for adaptive refinement will not be when using the error estimator. To have the same cells refined, one would needs to define the error criterion as 25% of the maximum local error. If the relationship between the error estimator and the reference error is $Y = \sqrt{X}$, then additional, unnecessary cells will be flagged for adaptive refinement. On the other hand, if two sets have a linear relation such as $Y = AX + B$, where A and B are unknown constants, then the exact same cells will be included in the adaptive refinement. Therefore, we can conclude that an error estimator having a linear relationship with the reference error is an ideal error estimator.

Unfortunately, it is unlikely that any of the error estimators from Chapter 3 will exhibit such a clear relationship with the true error. However, the observation gives a clue to assessing error estimators. That is, the quality of an error estimator depends on how closely it approximates a linear relationship with the true error. There is a parameter for quantifying a linear relationship between two sets. It is called the Pearson product-moment correlation coefficient, or the Pearson correlation coefficient. The Pearson correlation coefficient quantifies a linear relationship between two sets. The coefficient approaches unity when two sets are linearly related while it goes to zero as two sets deviate from linearity.

However, the correlation coefficient alone does not indicate whether the error estimator has identified a cell as having a large error when the true error is small (what we will call *inefficient*) or whether it has identified a cell as having a small error when the true error is large (what we will call *inaccurate*). A useful tool to better address this issue is a scatter plot of the two sets. The scatter plot intuitively shows the quality of the error estimators. With the local error plots shown in Chapter 3, the Pearson correlation coefficients, and the scatter plots, we can evaluate error estimators in terms of the distribution of local errors, how close a given error estimator is to an ideal error estimator, and whether the error estimators are inefficient or inaccurate.

Finally, for many practical problems the true error is unknown. We consider test cases involving spheres and cylinders, for which the exact solutions and the true errors can be

determined. We will also consider problems such as flat plates and the NASA almond, for which we will estimate a reference error from a numerical solution involving many more degrees of freedom than the problem being tested.

Therefore, in this chapter, we will explain the Pearson correlation coefficient, introduce the scatter plot of two error estimators, and use them to assess the error estimators introduced in Chapter 3 for various examples.

4.2 Pearson Correlation Coefficient

Let us begin with the definition of the Pearson correlation coefficient. For two given distinct sets X, and Y, the Pearson correlation coefficient $\rho_{X,Y} \in [-1, 1]$ is defined as

$$\rho_{X,Y} = \frac{\text{cov}(X, Y)}{\sigma_X \sigma_Y} = \frac{E[(X - \mu_X)(Y - \mu_Y)]}{\sigma_X \sigma_Y} \tag{4.1}$$

where $\text{cov}(\cdot, \cdot)$ is the covariance, $E[\cdot]$ is the expectation, μ_X is the mean of X, and σ_X is the standard variation of X. If the sets contain a finite number of elements, i.e., $X = (x_1, x_2, \ldots, x_N)$ and $Y = (y_1, y_2, \ldots, y_N)$, then (4.1) becomes

$$\rho_{X,Y} = \frac{\sum_{i=1}^{N}(x_i - \mu_X)(y_i - \mu_Y)}{\sqrt{\sum_{i=1}^{N}(x_i - \mu_X)^2 \sum_{i=1}^{N}(y_i - \mu_Y)^2}} \tag{4.2}$$

Assume that two sets are in a linear relationship, i.e., $Y = AX + B$. Then, each element x_i and y_i, $i = 1, 2, \ldots, N$ satisfies $y_i = Ax_i + B$ and their mean values do the same ($\mu_Y = A\mu_X + B$). Subtracting gives

$$y_i - \mu_Y = A\,(x_i - \mu_X) \tag{4.3}$$

for all $i = 1, 2, \ldots, N$. Substituting (4.3) into (4.2) results in

$$\rho_{X,Y} = \frac{A\sum_{i=1}^{N}(x_i - \mu_X)^2}{\sqrt{A^2\left[\sum_{i=1}^{N}(x_i - \mu_X)^2\right]^2}} = \frac{A}{|A|} = \pm 1 \tag{4.4}$$

Table 1: Pearson correlation coefficients of error estimators for the spherical cavity when a z-polarized electric current source is located near the North pole.

	J_{ref}	J_{t}	ρ_{e}	Res $\mathrm{E_t}$	Res $\mathrm{H_n}$	ρ_{rec}	J_{imp}
J_{ref}	1.00	0.05	0.74	0.78	-0.08	0.83	0.99
J_{t}	0.05	1.00	0.54	0.49	0.47	0.54	-0.03
ρ_{e}	0.74	0.54	1.00	1.00	-0.09	0.96	0.69
Res $\mathrm{E_t}$	0.78	0.49	1.00	1.00	-0.13	0.96	0.73
Res $\mathrm{H_n}$	-0.08	0.47	-0.09	-0.13	1.00	0.09	-0.09
ρ_{rec}	0.83	0.54	0.96	0.96	0.09	1.00	0.79
J_{imp}	0.99	-0.03	0.69	0.73	-0.09	0.79	1.00

Hence, points consisting of (x_i, y_i) $(i = 1, 2, \ldots, N)$ are exactly on a line when the Pearson correlation coefficient is either 1 or -1. The sign of the coefficient depends on whether the line has a positive slope or a negative slope.

If the absolute value of the correlation coefficient is close to 1, the elements of the two sets are likely to be clustered around a certain line, implying two sets are linearly correlated. In practice, two sets are said to be strongly correlated when the absolute value of the correlation coefficient is greater than 0.7. In contrast, they tend to be scattered irregularly when the coefficient is close to 0. If the coefficient is equal to 0, the two sets are uncorrelated and are considered to be random and independent.

An example of the Pearson correlation coefficients of error estimators is shown in Table 1. The correlation coefficients are obtained from the spherical cavity problem, where the sphere radius is 0.5λ, and a z-polarized electric current source is placed on the z-axis. The distance between the point source and the surface is 0.05λ. The local error plots are shown throughout Chapter 3.

In Table 1, J_{ref} is the reference error, J_t is the current discontinuity error estimator, ρ_{e} is the charge discontinuity error estimator, Res $\mathrm{E_t}$ is the tangential residual error estimator, Res $\mathrm{H_n}$ is the normal residual error estimator, ρ_{rec} is the charge recovery error estimator, and J_{imp} is the implicit error estimator. Each element in Table 1 gives the correlation

coefficient between the two error estimators corresponding to that row and column. For instance, elements in the first column are the correlation coefficients between the reference error and the other error estimators. The diagonal of Table 1 is equal to 1 because two identical sets exactly form a line. In addition, Table 1 is symmetric along the diagonal because $\rho_{X,Y} = \rho_{Y,X}$.

In Table 1, the implicit error estimator shows the strongest correlation with the reference error with a correlation coefficient of almost 1. Correlation coefficients for the charge discontinuity estimator, the tangential residual estimator, and the charge recovery estimator are larger than 0.7, which implies strong correlations with the actual error. In contrast, the current discontinuity estimator and the normal residual estimator appear to be uncorrelated with the true error. It is notable that the charge discontinuity error estimator, the tangential residual error estimator, and the charge recovery error estimator produce similar error levels because their correlation coefficients with each other are more than 0.96, even though these error estimators have different correlation coefficients with the reference error.

The correlation coefficients in Table 1 suggest several issues. The first arises when the correlation coefficient is below 0. If the correlation coefficient is close to -1, the estimator is assigning a large error to regions with small actual error and small errors to regions with large actual error. In that case, the error estimator may be poorly defined, since its result is the opposite of what is desired. However, Table 1 does not show any results with a correlation near -1. The negative correlations in Table 1 are all near zero, suggesting that the data sets are uncorrelated. Therefore, we can conclude that the quality of a given error estimator is poor when its correlation coefficient is less than 0.

Secondly, correlation coefficients near 0, for instance the correlation between the reference error and the current discontinuity error estimator, suggest that the local error plot will be random and independent. However, Fig. 3.2(a) and Fig. 3.3(a) show that the current discontinuity error estimator appears to agree with the reference error except for 4 mesh cells around the North pole of the sphere. For the normal residual error estimator, there are only 8 cells around the North pole where the estimator error differs significantly from the reference error (see Fig. 3.8 (a)). The local error plots indicate that these two

error estimators are inaccurate in these regions rather than random and independent.

Finally, Table 1 shows that the charge discontinuity error estimator, the tangential residual error estimator, and the charge recovery error estimator are in strong correlation to one another (correlation coefficients of 0.96 or greater). However, their correlations with the reference error are only 0.74, 0.78, and 0.83, respectively. It infers that the performance of different error estimators can be similar to one another even though the correlation coefficients with the reference error are different.

In order to resolve the second and the third issues, it is useful to compute the likelihood or probability that the correlation coefficient of two uncorrelated sets is greater than any given value, ρ_0. This will clarify how often two random sets could be highly correlated, given the number of samples involved. This probability is denoted by

$$\text{Prob}_N(|\rho_{X,Y}| \geq \rho_0) \tag{4.5}$$

where N is the number of finite samples. The probability $\text{Prob}_N(|\rho_{X,Y}| \geq \rho_0)$ in (4.5) can be obtained by:

$$\text{Prob}_N(|\rho_{X,Y}| \geq \rho_0) = -\frac{2\Gamma(N-1)/2}{\sqrt{\pi}\Gamma((N-2)/2} \int_{|\rho_0|}^{1} (1-\rho_{X,Y})^{(N-4)/2} d\rho_{X,Y} \tag{4.6}$$

where $\Gamma(\cdot)$ is the Gamma function. Equation (4.6) can be obtained numerically.

It is said that the correlation of X and Y is *significant* when $\text{Prob}_N(|\rho_{X,Y}| \geq \rho_0) \leq 5\%$ and is *highly significant* when $\text{Prob}_N(|\rho_{X,Y}| \geq \rho_0) < 1\%$. In other words, it is very probable that two sets are related even though they are not in a linear relationship. For example, $\text{Prob}_{20}(|\rho_{X,Y}| \geq 0.7)$ is the probability that the correlation coefficient between two uncorrelated sets X and Y exceeds 0.7 when 20 samples are measured. The probability of this example is just 0.1%, which implies the correlation of the sets is highly significant and they are unlikely to be uncorrelated.

The probability $\text{Prob}_N(|\rho_{X,Y}| \geq \rho_0)$ for various examples are shown in Table 2. The first column represents the geometries in Fig. 3.1. The second column is the number of mesh cells for each geometry (local errors are defined on cells), and therefore the number of mesh cells is equivalent to the finite number of samples. The other columns give probabilities

Table 2: Probability that two uncorrelated sets produce the correlation coefficient greater than ρ_0 after N measurements.

		ρ_0						
Geometry	# of Cells	0	0.05	0.1	0.15	0.2	0.25	0.3
Plate	100	100	62	32	14	4.6	1.2	0.2
Sphere & Almond	128	100	58	26	9	2.4	0.4	
Torus	256	100	43	11	1.6	0.1		
Cylinder	320	100	37	7.4				

$\text{Prob}_N(|\rho_{X,Y}| \geq \rho_0)$ when ρ_0 varies from 0 to 0.3. Blanks in the table means that the probability is less than 0.1%.

The data in Table 2 lead to two observations. The first one is that even if the correlation coefficient has a value near 0, it does not necessarily mean that the two sets are random and independent. The correlation coefficient between the current discontinuity error estimator and the reference error for the spherical cavity is 0.05. If the relationship of the error estimators are truly random, the possibility of obtaining a correlation coefficient greater than 0.05 is 58%. This implies there is a reasonable chance (42%) that they are not actually uncorrelated. In fact, the local plot in Fig. 3.3 (a) tells they are not uncorrelated in reality. Therefore, a given error estimate and the reference error can be somewhat correlated even if their correlation coefficient is close to 0.

Another observation is that an error estimator can be useful for identifying large error domains even though it is not highly correlated with the reference error. According to Table 2, any error estimate, whose correlation coefficient with the reference error is larger than 0.3, is highly significant. Error estimators may deviate from an ideal, which means some of mesh cells having large local errors can be excluded and/or some of unwanted cells can be flagged for adaptive refinement. However, those estimators still exhibit some correlation with the reference error, and they can be utilized with an appropriate scheme for adaptive refinement. As we shall see in the following section, for the range of example problems under consideration, the correlation coefficients between estimators and the reference error

are never completely consistent, and no error estimator always yields a Pearson correlation coefficient greater than 0.7 with the reference error.

In order to better understand the error estimators under investigation, we introduce a scatter plot. The scatter plot allows us to interpret the correlation between two sets graphically. Examples of scatter plots are shown in Fig. 4.1 along with their possible correlation coefficient and artificial lines indicating how two sets form linear relationships. When the correlation coefficient is -1 or 1, we can see points from two sets are exactly on a specific line. When the absolute value of the correlation coefficient is between 0 and 1, the points start to deviate from the line but they still cluster around the line. The points are scattered irregularly as the correlation coefficient approaches 0. However, the points are not essentially random in distribution even in this case, as discussed above.

The scatter plot is formed as the following: consider two distinct sets X and Y. The number of elements in the two sets are finite and the same (i.e., $X = (x_1, x_2, \ldots, x_N)$ and $Y = (y_1, y_2, \ldots, y_N)$). Each element corresponds to the same measurement point. For instance, elements x_i and y_i are local errors measured by error estimators X and Y at the i-th mesh cell, respectively. Then, a scatter plot can be drawn by defining points (x_i, y_i) in the xy-plane.

For analysis of error estimators, two auxiliary lines are included each scatter plot as shown in Fig. 4.2. A vertical line represents the error criterion of the error estimator X, which will be the reference error in general. A horizontal line corresponds to the error criterion of the other error estimators.

The first quadrant of xy-plane is now divided into 4 regions and each region is explained as follows:

1. Region A: Local errors in this region are identified as large by the given error estimator and the reference error. The corresponding mesh cells will be included in the adaptive refinement process.

2. Region B: Local errors in this region are identified as small by the given error estimator and the reference error. The corresponding meshes will be excluded from adaptive

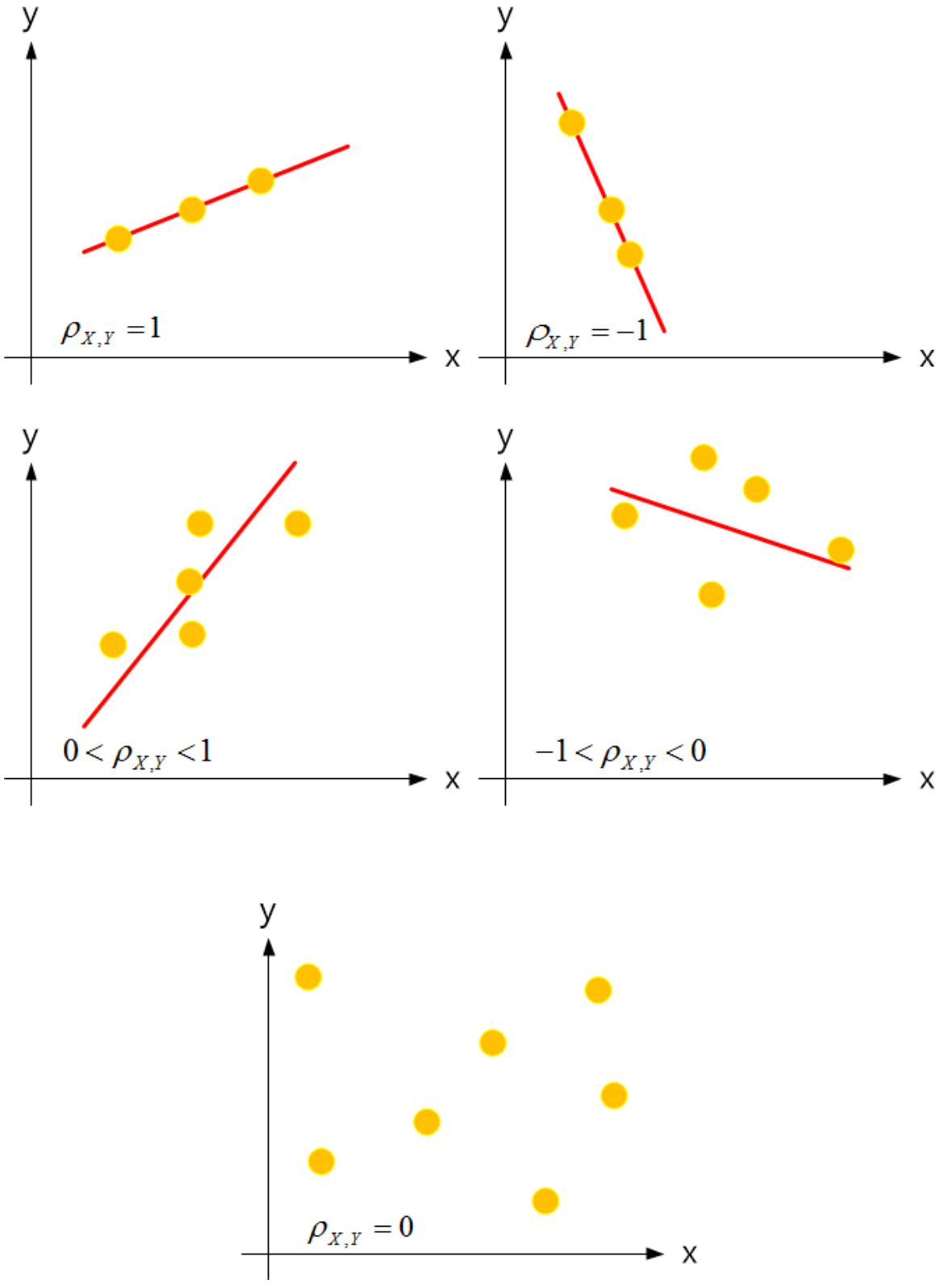

Figure 4.1: Examples of scatter plots and their possible correlation coefficient ranges.

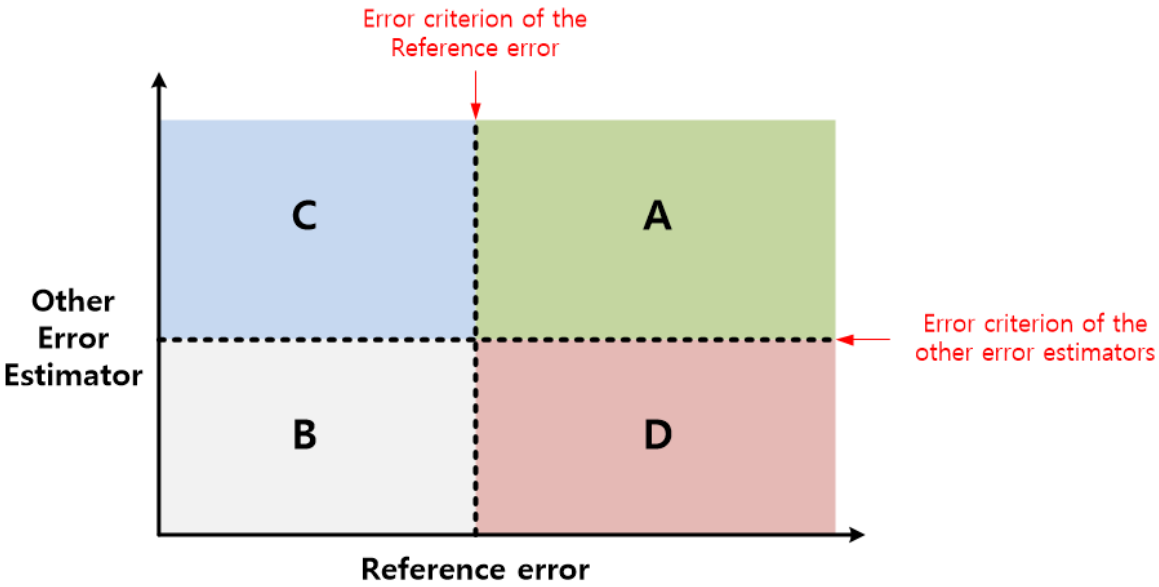

Figure 4.2: A scatter plot and two auxiliary lines for error estimators. Each dotted line represents the error criterion of the estimator.

refinement.

3. Region C: Local errors in this region are classified as large by the given error estimator, but the actual error is smaller than the error criterion. The corresponding mesh cells will be included in the refinement, unnecessarily, which give an additional cost to the adaptive refinement. Thus, the error estimator is inefficient.

4. Region D: Local errors in this region are classified as small by the error estimator, but the actual error is larger than the error criterion. This implies the error estimator is inaccurate.

Note that the areas of each region can be varied by adjusting the error criterion for each error estimator. That is, the accuracy of the error estimator may be improved by lowering the error criterion. However, that makes the error estimator less efficient. In Fig. 4.2, lowering the error criterion of the error estimator will lower the horizontal line. This leads to decrease of Region D (inaccuracy) and increase of Region A (accuracy) at the expense of increasing region C (inefficiency). Furthermore, for some example problems including the current discontinuity error estimator and the normal residual error estimator for the spherical cavity, lowering the error criterion does not improve the accuracy because

the largest reference errors are identified as the lowest when using those estimators. Thus, lowering the error criterion associated with an error estimator can only be useful for certain problems.

In the following sections, we will evaluate error estimators by considering test cases involving different geometries, source types, and source positions. We report the Pearson correlation coefficients, scatter plots, and local error plots. Based on this analysis, we will evaluate the various estimators under consideration and attempt to establish a scheme for the precise and computationally inexpensive adaptive refinement.

4.3 Correlation Between Error Estimators and Reference Error

In this section, six error estimators will be analyzed for five scattering problem test cases. We employ combinations of electric/magnetic current sources, different polarizations, and different positions of the current source for each case. The following subsections begin with descriptions of the geometry and source types. Then, the Pearson correlation coefficients, scatter plots, and local error plots will be reported. Due to the large number of scatter plots and local error plots, only some of them will be represented. Since our main interest is the correlation between the reference error and the other estimators, showing tables of the Pearson correlation coefficients will be sufficient to evaluate the quality of the error estimators. In the following, the x-axis of the scatter plots corresponds to the reference error. In addition, correlations between the charge discontinuity error estimator, the tangential residual error estimator, and the charge recovery error estimator will be presented because they are strongly correlated to one another for almost all cases. Finally we assign the error criterion for the error estimators and the reference error to be half of the maximum local error level produced from each error estimate.

4.3.1 Spherical Cavity

As a first test problem, consider a spherical cavity excited by an internal point source near its surface. The cavity geometry yields an exact solution, which facilitates obtaining a reference to compare with. By locating the point source near the sphere surface, we expect to force the current density to undergo rapid variation in that vicinity. This in turn should

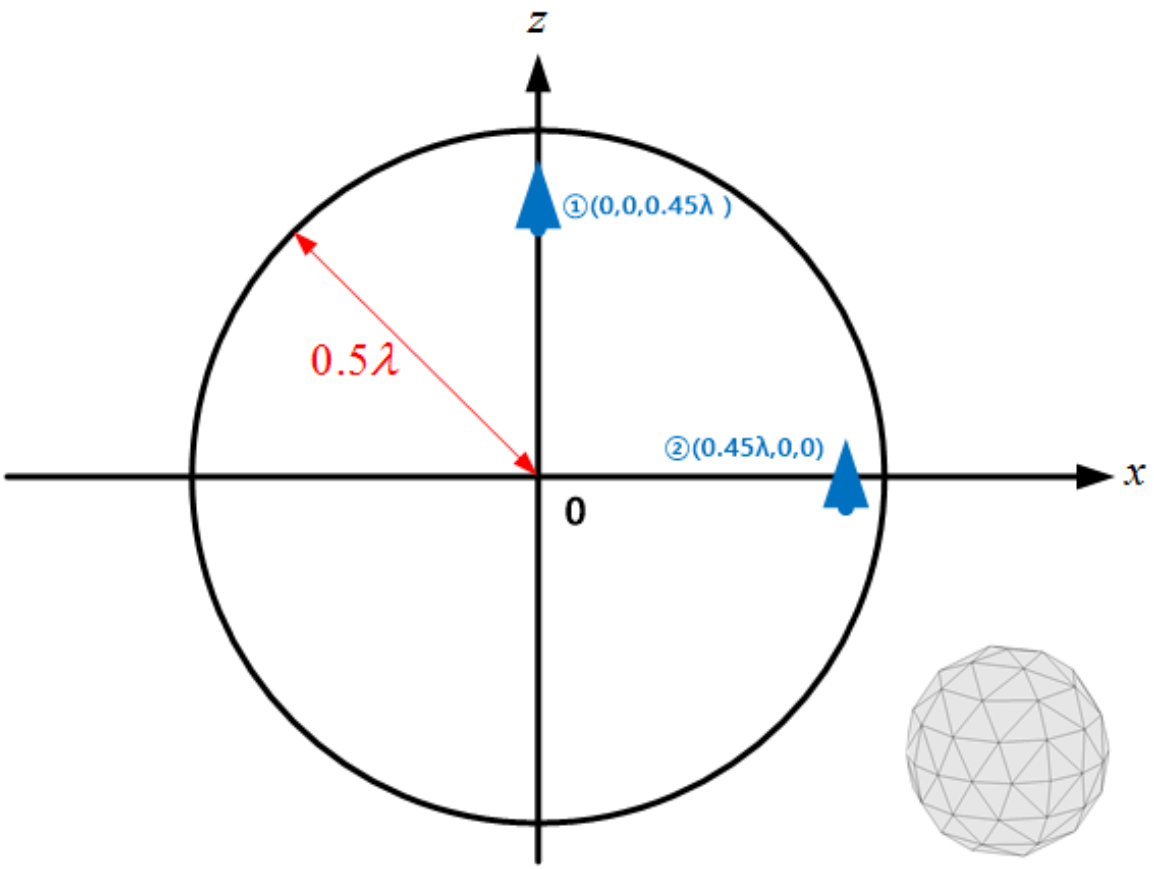

Figure 4.3: Geometry and source positions for a spherical cavity.

stress the numerical solution technique in that region, forcing it to exhibit greater error near the point source than over the other parts of the spherical surface.

The geometry of the spherical cavity is shown in Fig. 4.3. The radius of the sphere is 0.5λ. The sphere is discretized into 128 flat triangular cells, which are uniform and symmetric along the z-axis. Point sources are placed inside the sphere on either the z-axis or the x-axis, and their locations are denoted as circled numbers such as ①, ②. A magnetic current source and an electric current source are used on the z-axis while only an electric current source is employed for the x-axis. The point sources are all z-polarized, but the z-polarized point source on the x-axis is equivalent to an x- or y-polarized point source on the z-axis because the sphere itself is symmetric. Each of point sources is separated from the sphere surface by 0.05λ.

The reference surface current is obtained in exact form in terms of a Dyadic Green's

Table 3: Correlation coefficients between the reference error and the other error estimators for the spherical cavity.

Src.	Pos.	J_{t}	ρ_{e}	Res $\mathrm{E_t}$	Res $\mathrm{H_n}$	ρ_{rec}	J_{imp}
J_z	①	0.05	0.74	0.78	-0.08	0.83	0.99
J_z	②	0.95	0.76	0.79	0.95	0.71	0.71
M_z	①	0.85	0.35	0.83	0.82	0.30	0.83

function, where each expression in (A.1)-(A.6) involves infinite summations. For this example we truncated the summation after 60 terms (i.e., $n = 1, 2, \ldots, 60$).

The Pearson correlation coefficients between the reference error and the other error estimators are shown in Table 3. Again, J_{ref} represents the reference error, J_{t} is the current discontinuity error estimator, ρ_{e} is the charge discontinuity error estimator, Res $\mathrm{E_t}$ is the tangential residual error estimator, Res $\mathrm{H_n}$ is the normal residual error estimator, ρ_{rec} is the charge recovery error estimator, and J_{imp} is the implicit error estimator.

Consider the case when a z-polarized electric current source is placed near the North pole of the sphere (the first row in Table 3). Based on the Pearson correlation coefficients, the implicit estimator behaves almost like as an ideal error estimator. In contrast, the normal residual error estimator presents the worst performance, where the correlation coefficient is -0.08. The current discontinuity error estimator, whose correlation coefficient is 0.05, also does not appear to work correctly. Both the current discontinuity estimator and the normal residual error estimator miss mesh cells with high error around the North pole. The number of overlooked cells are greater for the normal residual estimator, which gives a lower correlation coefficient.

Scatter plots for the current discontinuity estimator, the charge discontinuity estimator, and the implicit estimator are presented because the scatter plot of the current discontinuity estimator looks similar to the normal residual estimator, and the scatter plots of the tangential residual estimator and the charge recovery estimator are analogous to the charge discontinuity estimator. The three scatter plots along with their local error plots

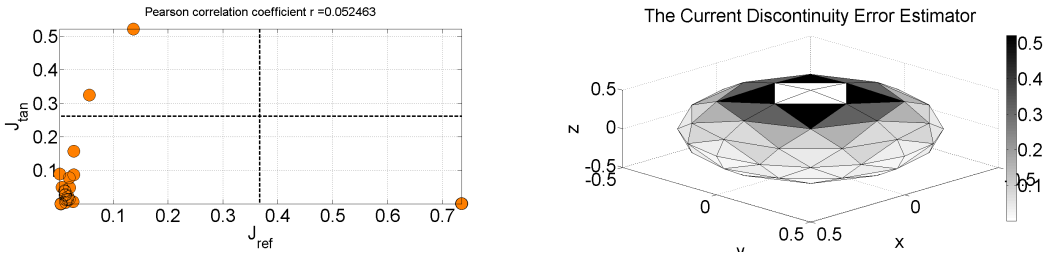

(a) A local error plot and a scatter plot for the current discontinuity error estimator.

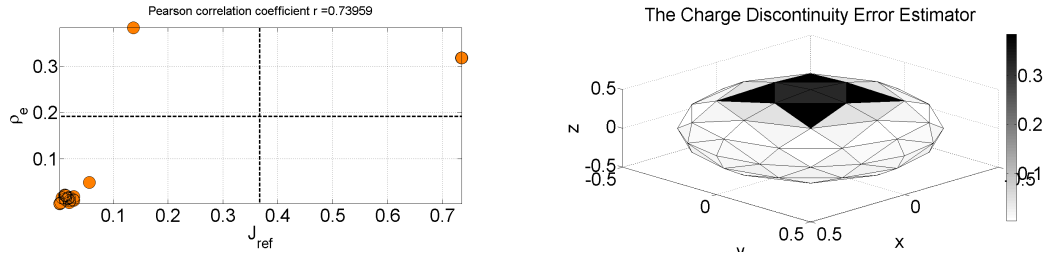

(b) A local error plot and a scatter plot for the charge discontinuity error estimator.

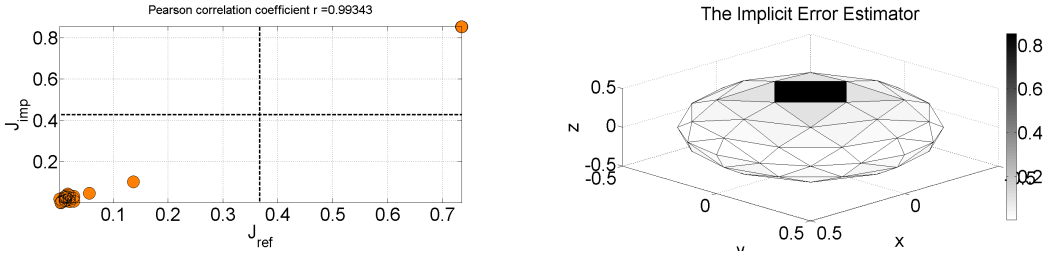

(c) A local error plot and a scatter plot for the implicit error estimator.

Figure 4.4: Local error plots and scatter plots of the spherical cavity when a z-polarized electric current source is at ①.

are presented in Fig. 4.4. Note that some of points in all scatter plots overlap because the spherical cavity mesh is uniform and symmetric.

From Fig 4.4(a), one can see that the current discontinuity error estimator fails to identify the large error cells. In fact, the error estimator cannot be improved by lowering its error criterion (the horizontal line in Fig. 4.4(a)) until the adaptive refinement region includes almost every cell. Moreover, the current discontinuity estimator forces several unnecessary cells into the adaptive refinement region, which deteriorates the estimator's efficiency.

One can improve the accuracy of the current discontinuity estimator to some extent by using the cells identified by the estimator but including additional neighboring cells. According to the scatter plot, the current discontinuity estimator and the reference error

are strongly correlated except for those cells around the North pole and this is clearly seen in the local error plot. The cells containing the largest errors determined by the current discontinuity estimator are adjacent to those having largest reference errors. That is, if the adaptive refinement scheme includes not only identified meshes but also some of their neighbors, the accuracy of the estimator can be enhanced at the expense of some additional computational cost.

For this test case, the charge discontinuity error estimator and the implicit error estimator are better at identifying cells with large error. The scatter plot and the local error plot obtained by the charge discontinuity estimator are shown in Fig. 4.4(b). Although the estimator has identified several unwanted mesh cells, it is accurate enough to be considered as being reliable and cheap. The scatter plot and the correlation coefficient for the implicit estimator is shown in Fig. 4.4(c). This estimate is well correlated with the reference error. As mentioned before, however, the performance of the error estimators is not consistent with every problem.

When an electric current source is located along the x-axis within the spherical cavity, the correlation coefficients of all the error estimators are above 0.7 (see the second row in Table 3). In this case, the performance of the error estimators seem to be reversed; the current discontinuity estimator is the closest to an ideal estimator, and the implicit error estimator shows the least resemblance to the true error (although since the correlation coefficient is 0.71, it can still be considered a good estimator).

The scatter plots and the local error plots for these estimators are shown in Fig. 4.5. The implicit error estimator misses several large error mesh cells.

These examples show that the Pearson correlation coefficient gives a good indication of the performance of an error estimator, but it does not provide any detailed information. The scatter plots provide another perspective that assists us in evaluating these estimators.

It is interesting to see that the performance of the current discontinuity estimator, the charge discontinuity estimator, the normal residual error estimator, and the charge recovery estimator appear to be opposite based on the source type: either an electric current source or a magnetic current source. This is shown in the third, fourth, sixth, and seventh columns

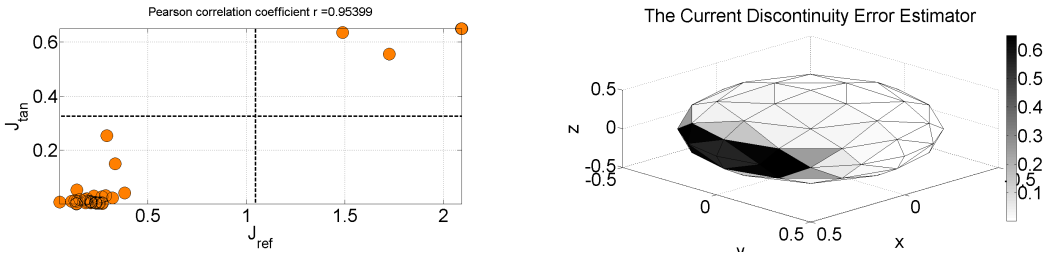

(a) A local error plot and a scatter plot for the current discontinuity error estimator.

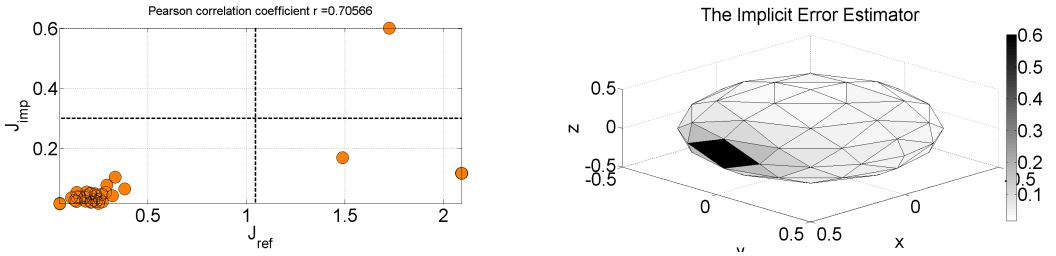

(b) A local error plot and a scatter plot for the implicit error estimator.

Figure 4.5: Local error plots and scatter plots of the spherical cavity when a z-polarized electric current source is at ②.

Table 4: Correlation coefficients between the charge discontinuity error estimator and the tangential residual error estimator/the charge recovery error estimator for the spherical cavity.

Src.	Pos.	Res E_t	ρ_{rec}
J_z	①	1.00	0.96
J_z	②	0.96	0.99
M_z	①	-0.06	0.91

of Table 3. The reason of failures of these estimators will be discussed in Chapter 5.

Finally, Table 4 provides correlation coefficients between the charge discontinuity error estimator and the tangential residual and charge recovery error estimators. The correlation coefficients are greater than 0.9, except for the case when the source is a magnetic current. This supports the conclusion that three error estimators are strongly correlated. The exception is that the charge discontinuity and the charge recovery estimators fail when a magnetic source is applied along the z-axis. As we shall see through the following subsections, the three estimators continue to show strong correlation with each other even when they are less correlated to the reference error.

4.3.2 Cylindrical Cavity

A second test problem is a cylindrical cavity excited by internal point sources. Like the sphere, this geometry yields an exact solution. The geometry of the cavity is shown in Fig. 4.5. The radius and the height of the cylinder are 0.2λ and 0.5λ, respectively. The number of mesh cells are 320, but they are neither uniform nor symmetric. Point sources are located inside the cavity, and all of them are separated from the surface by 0.05λ. As with the spherical cavity, electric current sources are x- or z-polarized while magnetic current sources are only z-polarized. The point sources create rapidly varying currents in their vicinity and stress the numerical solution in those regions. Thus, the large-error regions are those near the point sources.

The Dyadic Green's function is used for the expression of the reference current and it is presented in Appendix I. Since the reference current density is written as an infinite summation, it is truncated after 84 terms after ensuring the summation converges.

The correlation coefficients for the cylindrical cavity are summarized in Table 5. For a z-polarized electric current source, the current discontinuity error estimator shows the best performance for all cases, with correlation coefficients greater than 0.88. The correlation coefficients of the normal residual estimator are greater than 0.77, which similarly indicate strong correlation with the reference error. Unlike the spherical cavity, the implicit error estimator has the least correlation when the source is placed on ① and ③. The charge recovery estimator shows the smallest correlation with the reference error when the source is located at ②. Examples of the scatter plots and the local error plots for a source located at ① are shown in Fig. 4.7. The reported estimators are the current discontinuity estimator, the charge recovery estimator, and the implicit error estimator, respectively. The scatter plots reflect the non-uniform and non-symmetric mesh characteristics: distributions of points in the plots for the cylindrical cavity are widely distributed while those in the spherical cavity are gathered except for several cells.

The current discontinuity estimator, shown in Fig. 4.7(a), accurately predicts all large error cells but includes a few unnecessary cells, too. The large error domains are not cells that have the shortest distance to the source point. The charge recovery estimator

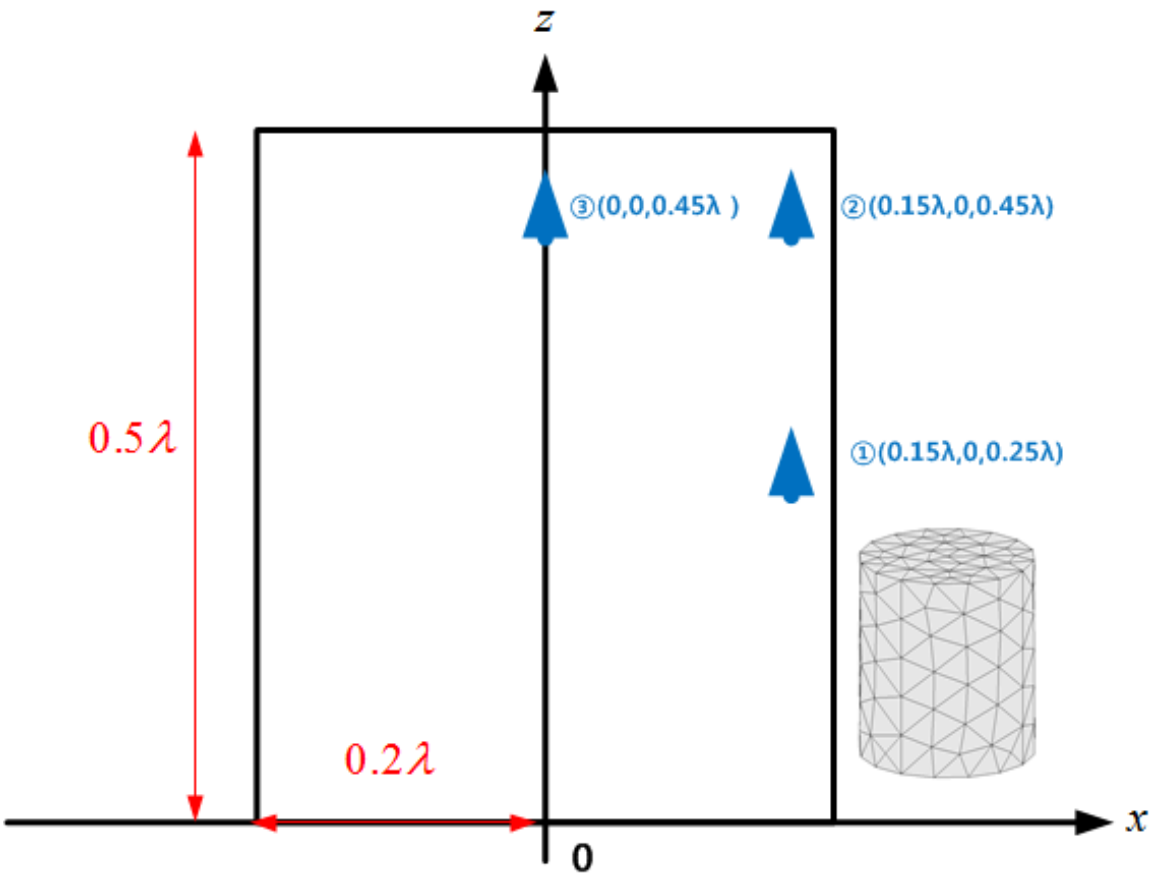

Figure 4.6: Geometry and source positions for a cylindrical cavity.

Table 5: Correlation coefficients between the reference error and the other error estimators for the cylindrical cavity.

Src.	Pos.	J_t	ρ_e	Res E_t	Res H_n	ρ_{rec}	J_{imp}
J_z	①	0.94	0.63	0.62	0.80	0.50	0.49
J_z	②	0.94	0.75	0.80	0.82	0.65	0.74
J_z	③	0.88	0.70	0.70	0.77	0.71	0.70
M_z	①	0.80	0.85	0.54	0.86	0.93	0.81
M_z	②	0.88	0.88	0.73	0.45	0.84	0.65
M_z	③	0.74	0.74	0.82	0.58	0.60	0.78
J_x	①	0.95	0.62	0.85	0.90	0.60	0.70
J_x	②	0.86	0.81	0.83	0.76	0.69	0.77
J_x	③	0.81	0.79	0.81	0.66	0.69	0.83

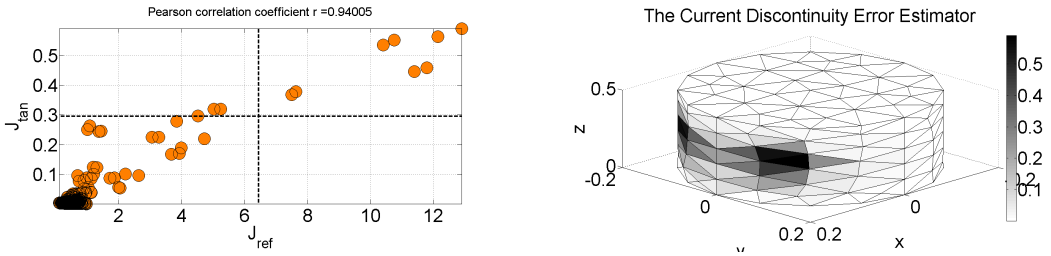

(a) A local error plot and a scatter plot for the current discontinuity error estimator.

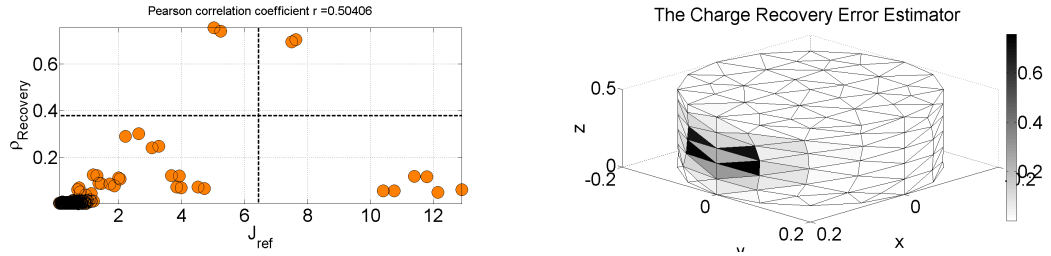

(b) A local error plot and a scatter plot for the charge recovery error estimator.

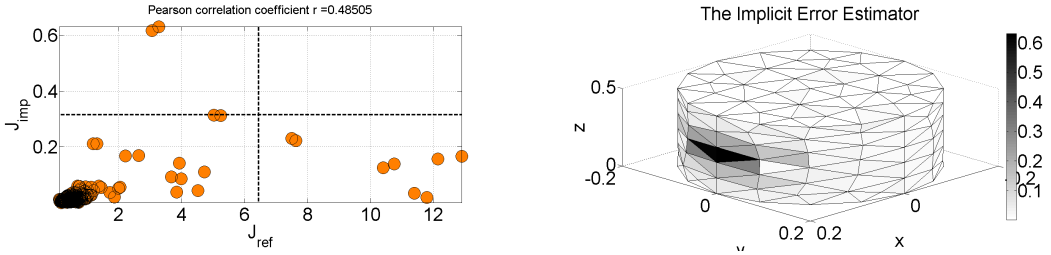

(c) A local error plot and a scatter plot for the implicit error estimator.

Figure 4.7: Local error plots and scatter plots of the cylindrical cavity when a z-polarized electric current source is at ①.

overlooks most of the important large-error cells, but identifies some of their neighbors (see Fig. 4.7(b)). It suggests that it is not sufficient to only include cells immediately adjacent to those identified by the estimator, but also to involve more mesh cells. This performance can also be seen for the scatter plot and the local error plot of the implicit estimator as shown in Fig. 4.7(c). The implicit estimator identifies the cells which are the closest to the point source as large error regions and determines none of the actual large error mesh cells. The actual large-error cells are not only those sharing edges of those flagged by the estimator but also those sharing nodes with them.

For magnetic current sources, the correlation coefficients between the current discontinuity estimator and the reference are reduced compared to those produced by electric current sources. Instead, the charge recovery estimator, the charge discontinuity estimator, and the

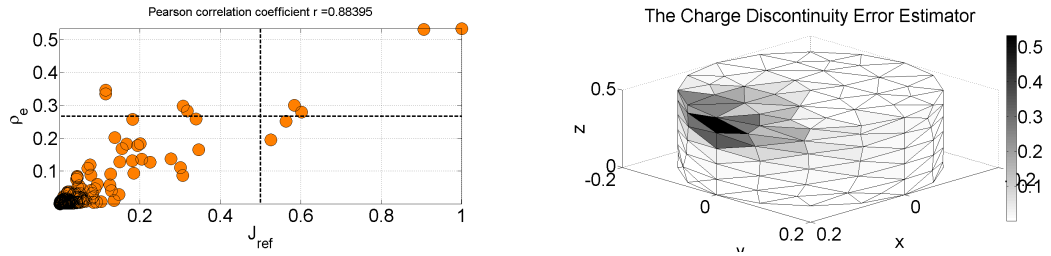

(a) A local error plot and a scatter plot for the charge discontinuity error estimator.

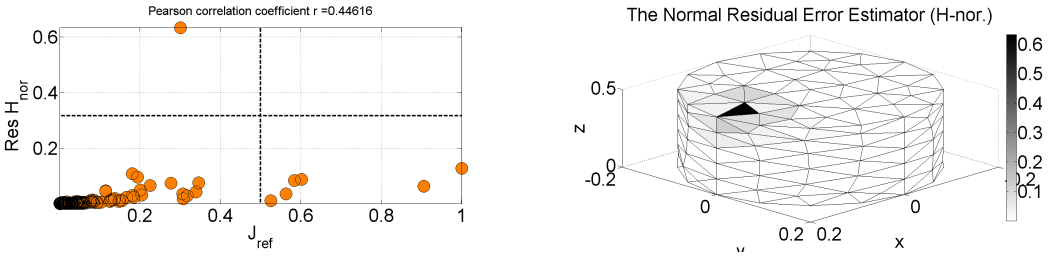

(b) A local error plot and a scatter plot for the normal residual error estimator.

Figure 4.8: Local error plots and scatter plots of the cylindrical cavity when a z-polarized magnetic current source is at ②.

tangential residual estimator give the strongest correlations when the magnetic sources are at ①, ②, and ③, respectively.

Examples of the scatter and local error plots for a source located at ② within the cylinder are shown in Fig. 4.8. Plots are shown for the charge discontinuity estimator and the normal residual estimator. The charge discontinuity estimator identifies major error domains as well as several unwanted cells as shown in Fig. 4.8(a). Although two cells having large reference error are not identified by the charge discontinuity estimator, those are adjacent cells and can easily be covered by adaptive refinement. Figure 4.8(b) show plots for the normal residual estimator. When only observing the local error plot and the correlation coefficient, the estimator identifies an incorrect cell and this results in a low correlation coefficient. However, the scatter plot shows that the normal residual estimator is reasonably correlated with the reference error except for that one cell. This suggests that a minor error can seriously deteriorate the overall performance of the estimator.

When an electric current is x-polarized (Table 5), the current discontinuity estimator has strong correlation with the reference estimator. It has the largest correlation coefficients when the source is at ①, and ②. Unlike z-polarized sources, all correlation coefficients are

Table 6: Correlation coefficients between the charge discontinuity error estimator and the tangential residual error estimator/the charge recovery error estimator for the cylindrical cavity.

Src.	Pos.	Res E_t	ρ_{rec}
J_z	①	0.95	0.91
J_z	②	0.88	0.91
J_z	③	0.96	0.91
M_z	①	0.86	0.88
M_z	②	0.90	0.89
M_z	③	0.88	0.94
J_x	①	0.83	0.89
J_x	②	0.92	0.89
J_x	③	0.92	0.93

greater than 0.6. On the other hand, the correlation coefficients for the charge recovery estimator are always below 0.7, indicating that that estimator has difficulty in identifying large error meshes.

Table 6 shows correlations between the charge discontinuity estimator and the tangential residual and charge recovery estimators. The estimators are strongly correlated, with correlation coefficients greater than 0.83. This implies that the large error regions are similar to one another even if one of the estimators has a low correlation with the reference. For x-polarized electric sources, for example, the tangential residual estimator gives correlation coefficients greater than 0.81 while the correlation coefficients of the charge recovery estimator are lower than 0.7. However, the resemblance of these estimators suggests that a good adaptive refinement strategy may be able to use them to identify all the large-error cells.

4.3.3 Rectangular Plate

The rectangular plate is a simple structure but does not yield to exact electromagnetic analysis, even for a plane wave excitation. Simple numerical solutions (such as those based

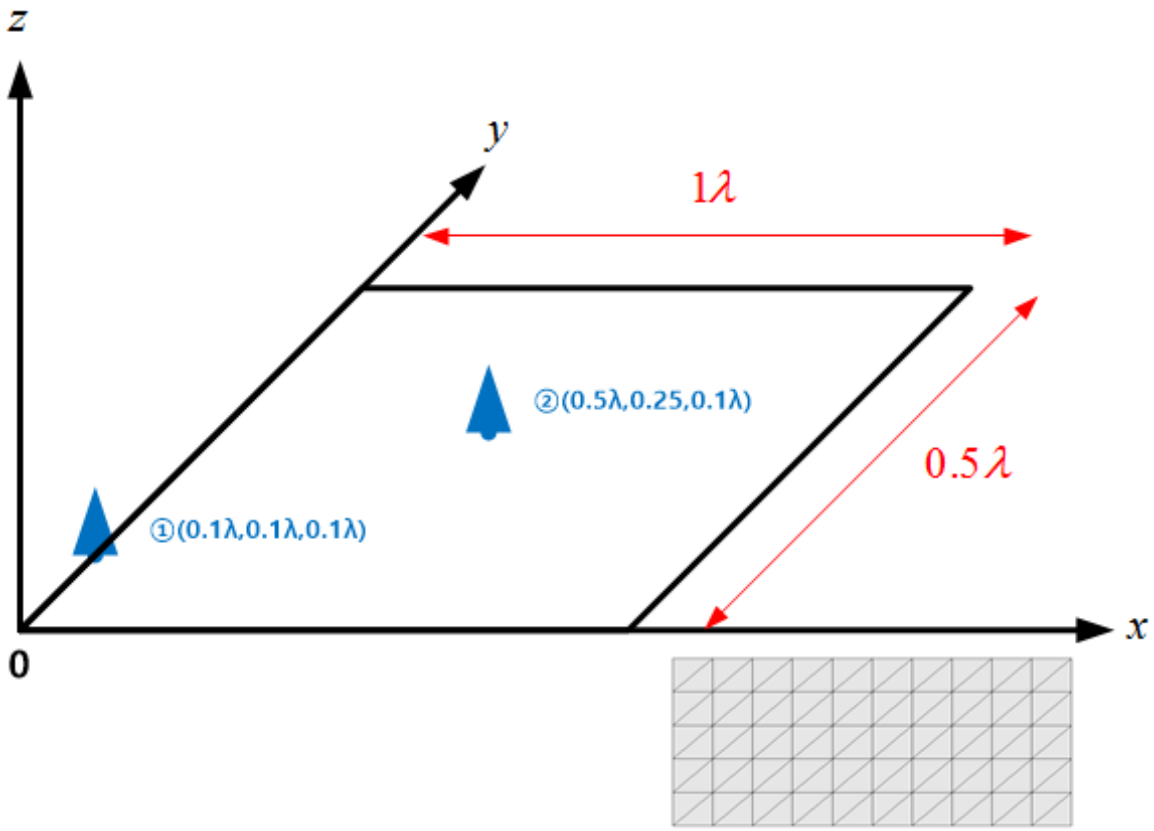

Figure 4.9: Geometry and source positions for a rectangular plate.

on the RWG basis functions) do not properly incorporate the edge conditions (where certain components of the current and charge density are infinite). Therefore, the large error domains of the rectangular plate tend to be the edges. There is an additional singularity in the current density at each corner that is not represented by the basis. For this example we employ a normally-incident plane wave excitation as well as point source excitations.

The dimensions of the plate are presented in Fig. 4.9. The length and width of the

Table 7: Correlation coefficients between the reference error and the other error estimators for the rectangular plate.

Src.	Pos.	J_t	ρ_e	Res E_t	Res H_n	ρ_{rec}	J_{imp}
J_z	Plane wave	0.49	0.31	0.30	0.83	0.30	0.87
J_z	①	0.70	0.59	0.63	0.81	0.44	0.41
J_z	②	0.54	0.41	0.45	0.49	0.21	0.29

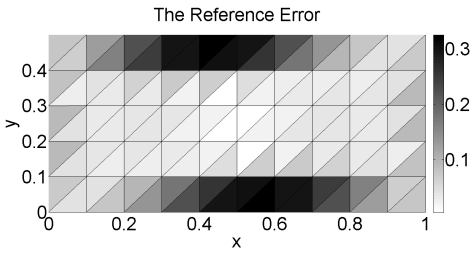

(a) A local error plot for the reference error.

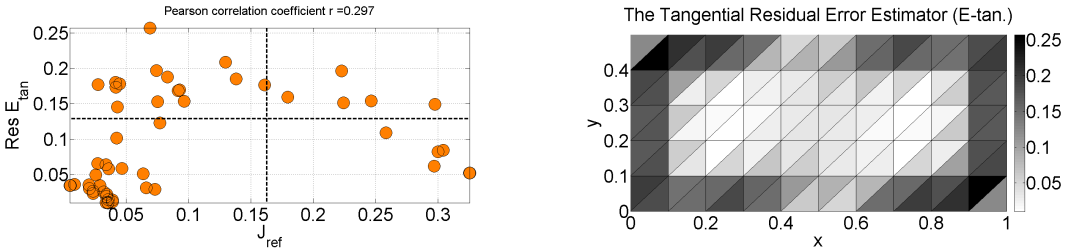

(b) A local error plot and a scatter plot for the tangential residual error estimator.

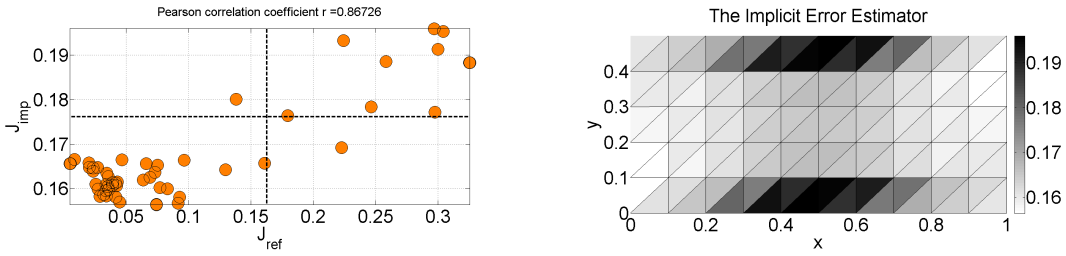

(c) A local error plot and a scatter plot for the implicit error estimator.

Figure 4.10: Local error plots and scatter plots for the rectangular plate when a plane wave source is x-polarized and propagates in the z-direction.

plate are 1λ and 0.5λ, respectively. The number of mesh cells is 200. The magnitude of the incident plane wave electric field is unity, it is x-polarized, and it propagates in the z-direction. Electric current sources are z-polarized, and are located at the corner and the center of the plate. The reference error is obtained by solving the problem with a refined mesh, containing 800 cells.

For the plate test case, correlation coefficients for various estimators are given in Table 7. Comparing to previous test cases, the coefficients are relatively small. In particular, none of correlation coefficients is greater than 0.54 when the source is at the center of the plate. Because of this, we will provide local error plots of the reference error before evaluating the other error estimators.

Figure 4.10(a) shows a plot of the reference error for the plate with plane wave excitation.

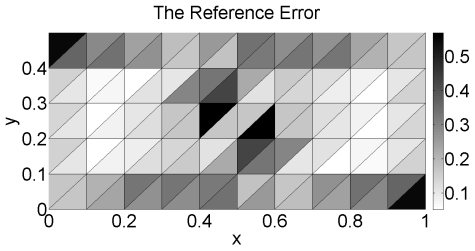

(a) A local error plot for the reference error.

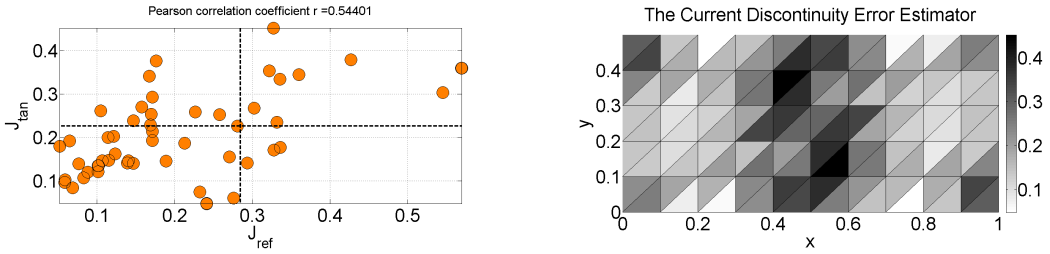

(b) A local error plot and a scatter plot for the current discontinuity error estimator.

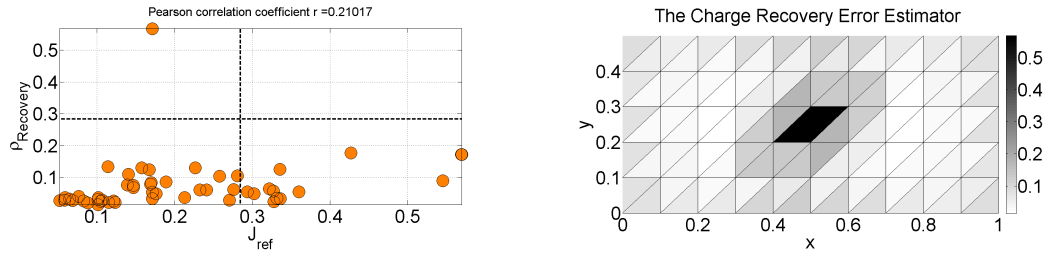

(c) A local error plot and a scatter plot for the charge recovery error estimator.

Figure 4.11: Local error plots and scatter plots of the rectangular plate when a z-polarized electric current source is at ②.

The reference error is largest near the center of the longer plate edges, where the current density is the largest. Figure 4.10(b) shows a scatter plot and a local error plot obtained from the tangential residual error estimator. The estimator identifies almost all the cells along the plate edges. While it only overlooks a few large-error cells, it flags too many unnecessary cells for adaptive refinement, which in turn will require excessive computations and slow down the refinement algorithm. On the other hand, the implicit estimator correctly identifies the large-error domains as shown in Fig. 4.10(c). Compared with the reference error, the large error regions determined by the implicit estimator are slightly shifted along the edges.

Figure 4.11 shows plots for the plate excited by an electric current source at the center, ②. A plot of the reference error is shown in Fig. 4.11(a). The large local error domains are

near the center and are at two corners of the plate. Those errors at the corners may be due to an insufficient representation of the current density by the RWG basis functions, which do not properly model either the edge singularity or the separate corner singularity.

For this excitation, the largest correlation coefficient (Table 7) is 0.54, which is produced by the current discontinuity estimator. The scatter and local error plots for the current discontinuity estimator are shown in Fig. 4.11(b). The estimator incorrectly identifies many cells, resulting in the relatively low correlation coefficient, even though the estimator includes most of the large-error cells. The implicit estimator recognizes two cells at the center of the plate as the large error domains as shown in Fig. 4.11(c). These cells are in the vicinity of the large-error region around the center of the plate, but the estimator misses the regions around the corners. The charge discontinuity estimator, the tangential residual estimator, and the charge recovery estimator yield similar results as the implicit estimator. For this example, it appears that estimators with correlation coefficients less than 0.7 may miss large error domains.

Finally, the Pearson correlation coefficients between the charge discontinuity estimator and the tangential residual and charge recovery estimators are given in Table 8. As in previous examples, the tangential residual estimator shows a very strong correlation with the charge discontinuity estimator, with correlation coefficients greater than 0.9. The charge recovery estimator is also strongly correlated with the charge discontinuity estimator.

Table 8: Correlation coefficients between the charge discontinuity error estimator and the tangential residual error estimator/the charge recovery error estimator for the rectangular plate.

Src.	Pos.	Res E_t	ρ_{rec}
J_z	Plane wave	0.99	0.79
J_z	②	0.98	0.94
J_z	③	0.91	0.80

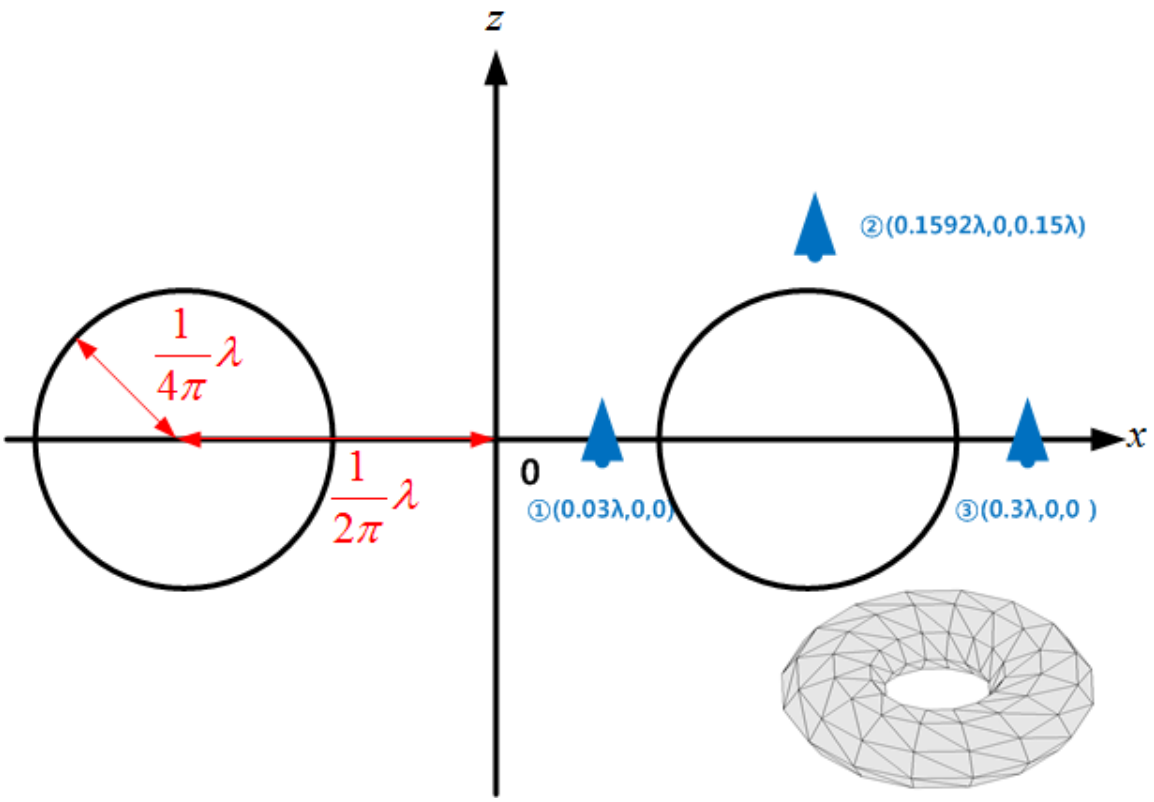

Figure 4.12: Geometry and source positions of a torus.

4.3.4 Torus

A torus is is generated by rotating a circle in three dimensions. The radius of the circle is called the minor radius. In addition, the trajectory of the rotation also draws a circle. The radius of the trajectory that passes the center of the circle having the minor radius is said to be the major radius. In common with a sphere or spheroid, the torus is a smooth geometry and is sometimes used to verify numerical solutions due to this well-behaved property. While it does not yield exact solutions some reference data is available [16].

A cross section of the torus is presented in Fig. 4.12. The major radius and the minor radius are $\frac{\lambda}{2\pi}$ and $\frac{\lambda}{4\pi}$, respectively. Meshes of the torus can be uniform and symmetric, and the total number of cells is 256. A reference solution is obtained from a numerical solutions with a finer mesh, with 1024 cells. Electric current sources are placed on the x-axis, and they are all z-polarized. The positions of the point sources are inside(①), above(②), and outside(③) the torus cross section.

Table 9: Correlation coefficients between the reference error and the other error estimators for the torus.

Src.	Pos.	J_{t}	ρ_{e}	Res $\mathrm{E_t}$	Res $\mathrm{H_n}$	ρ_{rec}	J_{imp}
J_z	①	0.89	0.78	0.80	0.57	0.76	0.85
J_z	②	0.91	0.87	0.82	0.52	0.87	0.67
J_z	③	0.93	0.88	0.88	0.69	0.78	0.86

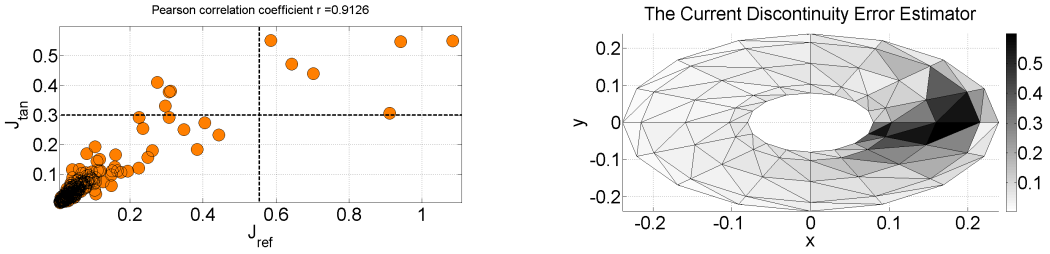

(a) A local error plot and a scatter plot for the current discontinuity error estimator.

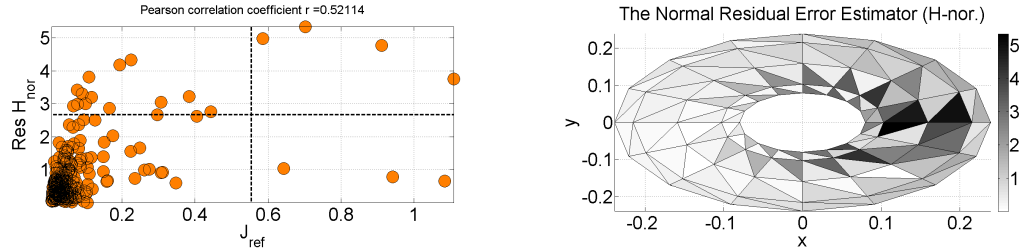

(b) A local error plot and a scatter plot for the normal residual error estimator.

Figure 4.13: Local error plots and scatter plots of the torus when a z-polarized electric current source is at ②.

Table 9 presents the Pearson correlation coefficients for the torus. Most of the estimators except for the normal residual estimator and the implicit estimator show strong correlation with the reference error for all cases. This is because the torus is a continuous geometry and there is no cancellation due to symmetry as in the spherical cavity. The performance of the current discontinuity estimator is the best for this problem according to the correlation coefficients. The values are 0.89 for a source located inside the torus, 0.91 for a source on the top, and 0.93 for a source outside. In contrast to the current discontinuity estimator, the normal residual error estimator has the smallest correlation coefficients. They are 0.57 for the inside, 0.52 for the top, and 0.69 for the outside.

Table 10: Correlation coefficients between the charge discontinuity error estimator and the tangential residual error estimator/the charge recovery error estimator for the torus.

Src.	Pos.	Res E_t	ρ_{rec}
J_z	①	0.95	0.83
J_z	②	0.95	0.89
J_z	③	0.96	0.89

The scatter and local error plots for the current discontinuity estimator and the normal residual estimator, when the point source is located above the torus, are shown in Fig. 4.13. Except for several unnecessary cells, the current discontinuity estimator, as shown in Fig. 4.13(a), identifies the same cells as those determined by the reference error. The normal residual estimator flags more unwanted cells than the current discontinuity estimator and omits 3 cells that actually have large error. Those cells are adjacent to others that are flagged, however, so an adaptive refinement scheme that uses a slightly larger footprint will catch them. The other test cases show similar results: the current discontinuity estimator detects all important cells as well as some low-error cells while the other estimators each miss several cells with large errors and include more inessential ones.

As in the preceding examples, the correlations between the charge discontinuity estimator and the tangential residual and charge recovery estimators are given in Table 10. Again, the three estimators are strongly correlated, and in particular, correlations between the charge discontinuity estimator and the tangential residual estimator are stronger, with coefficients greater than 0.95, while those between the charge discontinuity estimator and the charge recovery estimator are 0.89 at best.

4.3.5 NASA Almond

The NASA almond is an interesting airfoil-like geometry: the front of the NASA almond is smooth, the top and bottom are quite flat, and the back surface forms a tip. Moreover, it is relatively long but thin. The thin and smooth sides of the NASA almond can be distorted to sharp corners, which can aggravate the accuracy of the numerical solution.

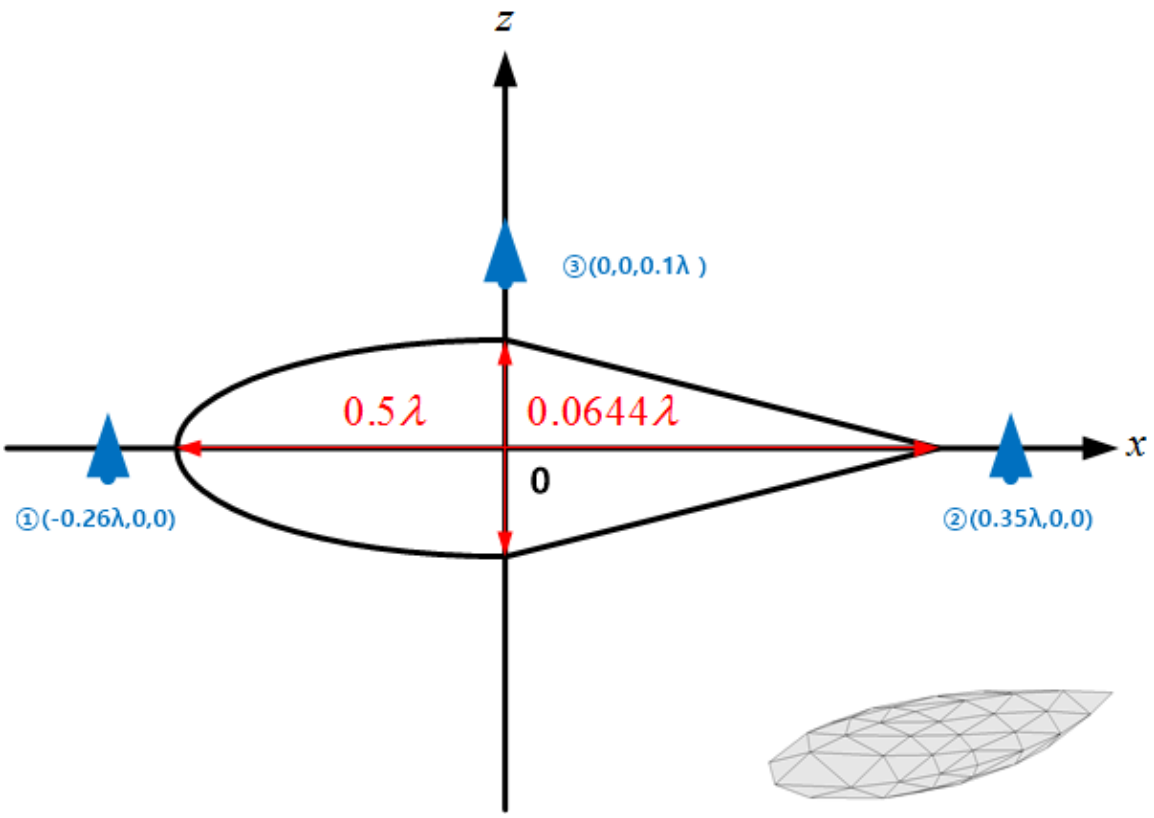

Figure 4.14: Geometry and source positions of a NASA almond.

The geometry of the NASA almond is described in Fig. 4.14. The length and the thickness of the almond are 0.5λ and 0.0644λ, respectively. z-polarized electric current sources are placed around the front (①), the back (②), and the top (③) of the scatterer. The distance between the point sources and the surface is set to be less than 0.1λ, to create a rapid variation in the local current density. A numerical solution obtained using a refined mesh with 512 cells is used as the reference error. The number of mesh cells used in the tests is 128. The meshes are built in the same way as the spherical cavity and therefore, they are symmetric but are not uniform due to the geometry of the almond.

The correlation coefficients for the NASA almond are shown in Table 11. Regardless of the positions of the sources, the correlation coefficients for the charge discontinuity estimator are the largest among the other estimators. They are 0.96 for sources at the front and the back, and 0.71 for a source at the top of the almond. The implicit estimator, however, has correlation coefficients close to 0. Except for the implicit estimator, correlation coefficients

Table 11: Correlation coefficients between the reference error and the other error estimators for the NASA almond.

Src.	Pos.	J_{t}	ρ_{e}	Res $\mathrm{E_t}$	Res $\mathrm{H_n}$	ρ_{rec}	J_{imp}
J_z	①	0.87	0.96	0.95	0.65	0.90	-0.13
J_z	②	0.90	0.96	0.81	0.65	0.94	0.04
J_z	③	0.70	0.71	0.57	0.25	0.58	0.14

of all estimators are smaller when the source is located on the top.

Figure 4.15 shows the scatter and local error plots of the current discontinuity estimator, the charge discontinuity estimator, the tangential residual estimator, and the implicit estimator when the point source is close to the front of the NASA almond. A plot of the reference error is added in Fig. 4.15(a). In this example, the charge continuity estimator yield the greatest correlation coefficient, 0.96. The coefficients of the current discontinuity estimator and the tangential residual error estimator are 0.87 and 0.95, respectively. When comparing the scatter plots of the current discontinuity estimator and the tangential residual estimator (see Fig. 4.15(b) and Fig. 4.15(c)) with that of the charge discontinuity estimator (Fig. 4.15(c)), those two error estimators contains 8 cells containing large reference error while the charge discontinuity estimator flags only half of them. Although the scatter plots and the local error plots indicate that the charge discontinuity estimator resembles the reference error, meshes that are included in the adaptive refinement by the charge discontinuity estimator are different from those included by the reference error. In contrast, meshes resulted from the current discontinuity estimator and the tangential residual estimator will be exactly same with those produced by the reference error. This happens due to the cells having error values close to the error criterion.

It is interesting to see that the implicit estimator does not work for this example. Although error estimators for the previous cases sometimes have very low correlation coefficients (i.e., the correlation coefficients of the discontinuity estimators in the spherical cavity), at least they usually identify cells near ones having a large actual error. For the

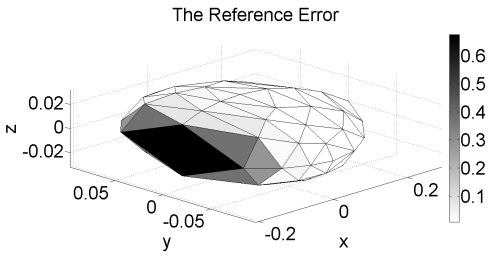

(a) A local error plot for the reference error.

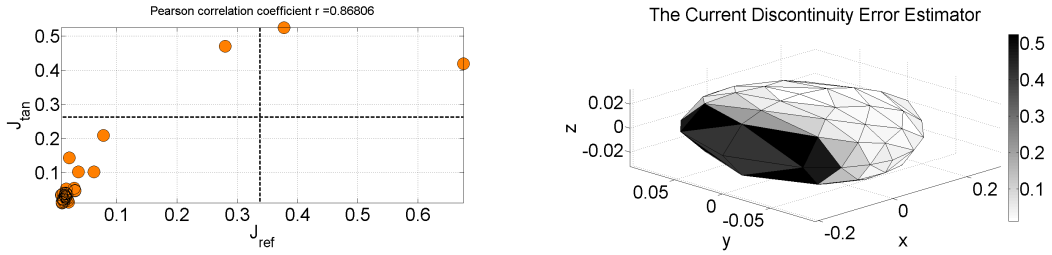

(b) A local error plot and a scatter plot for the current discontinuity error estimator.

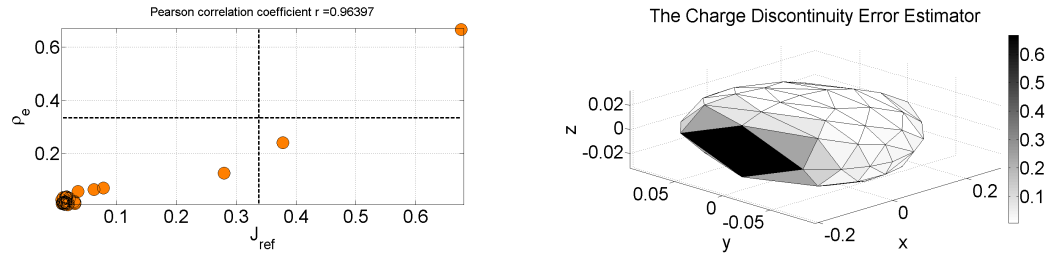

(c) A local error plot and a scatter plot for the charge discontinuity error estimator.

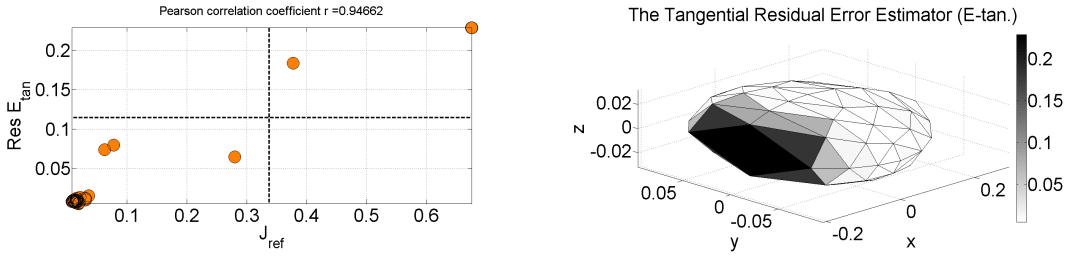

(d) A local error plot and a scatter plot for the tangential residual error estimator.

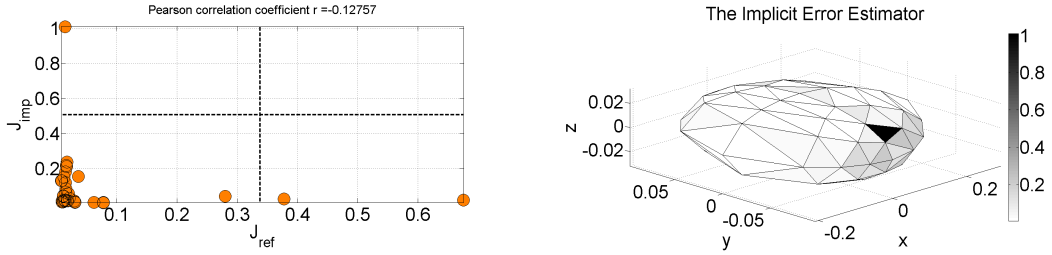

(e) A local error plot and a scatter plot for the implicit error estimator.

Figure 4.15: Local error plots and scatter plots of the NASA almond when a z-polarized electric current source is at ①.

almond, the implicit estimator fails for different source positions, which implies that the failure may come from the geometry combined with the source types.

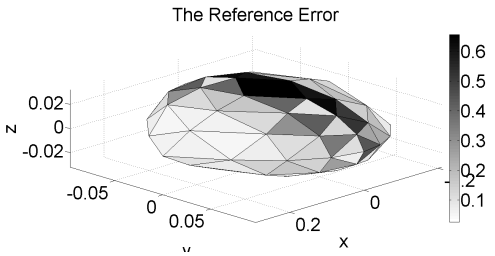

(a) A local error plot for the reference error.

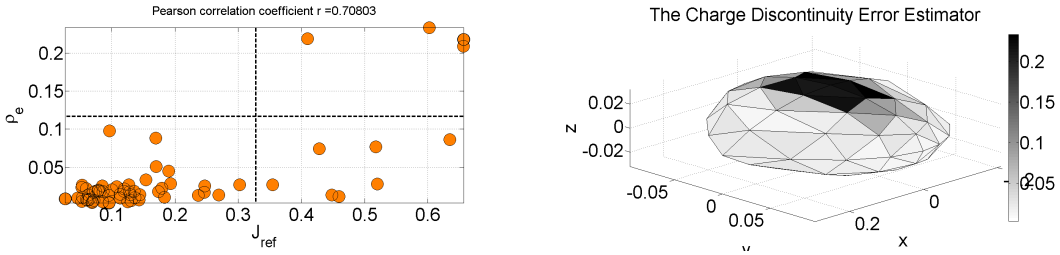

(b) A local error plot and a scatter plot for the charge discontinuity error estimator.

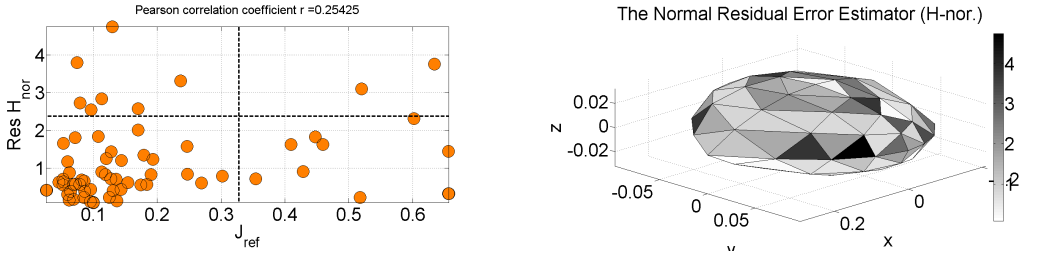

(c) A local error plot and a scatter plot for the normal residual error estimator.

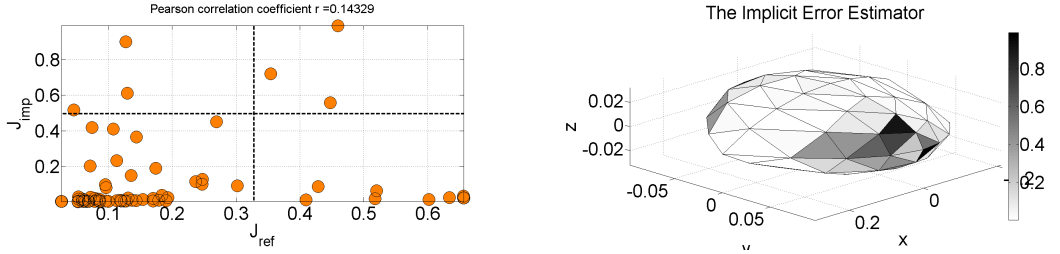

(d) A local error plot and a scatter plot for the implicit error estimator.

Figure 4.16: Local error plots and scatter plots of the NASA almond when a z-polarized electric current source is placed at ③.

Another example of the scatter and local error plots is given in Fig. 4.16 where the current source is located at the top of the almond. The reference error plot is presented in Fig. 4.16(a). The plots for the charge discontinuity estimator, the normal residual estimator, and the implicit estimator are shown in Fig. 4.16(b)-(d), respectively. The charge discontinuity estimator produces an error pattern similar to the reference error. The normal residual estimator and the implicit estimator, however, show irregular behaviors.

Lastly, the correlation coefficients between the charge discontinuity estimator and the

Table 12: Correlation coefficients between the charge discontinuity error estimator and the tangential residual error estimator/the charge recovery error estimator for the NASA almond.

Src.	Pos.	Res E_t	ρ_{rec}
J_z	①	0.91	0.98
J_z	②	0.70	0.98
J_z	③	0.95	0.84

tangential residual and charge recovery estimators are shown in Table 12. The correlations of these estimators are strong overall, but relatively weak when the source is at the back of the NASA almond. The reason may be due to large differences between error values at several cells. According to the correlation coefficients of these estimators, however, the local error plots seem to be similar to each other because the estimators are closely related to the reference error.

4.4 Concluding Remarks

In this chapter, we attempted to evaluate the performance of the local error estimators introduced in Chapter 3. We considered various test problems including a spherical cavity, a cylindrical cavity, a rectangular plate, a torus, and the NASA almond. In addition, we considered different source types, polarizations, and source locations. We employed the Pearson correlation coefficient, the scatter plot, and the local error plot to evaluate those error estimators.

An ideal error estimator should have a linear relationship with the reference error because only in that situation will the estimator correctly flag all the mesh cells requiring adaptive refinement. Since the Pearson correlation coefficient is able to quantify a linear relationship between two sets, it is useful for assessing error estimators. However, a larger correlation coefficient does not always indicate that an error estimate is more accurate. Based on the correlation coefficients, error estimators can be evaluated as follows:

1. $0.7 \leq \rho_{X,Y} \leq 1$: An error estimator with the correlation coefficient in this range can be

said to be reliable and efficient. Mesh cells overlooked by a given error estimator can be fully covered by broadening the footprint of the estimate to include cells sharing nodes with those that are identified.

2. $0.5 \leq \rho_{X,Y} < 0.7$: An error estimator having the correlation coefficient between 0.5 and 0.7 may be inefficient, but quite accurate. The estimator may identify some unnecessary cells and may omit some cells with large errors. The accuracy of the adaptive refinement can be improved by broadening the footprint as described above.

3. $0 \leq \rho_{X,Y} < 0.5$: This estimator is either unreliable and/or inefficient. The estimator will identify a large number of unnecessary cells or will fail to determine large-error domains. The accuracy may be improved by broadening the estimate footprint but not as reliably as in the previous cases.

Table 13 provides averaged values of the correlation coefficients for the different geometries. Discontinuity estimators show strong correlations with the reference error in many problems: the current discontinuity estimator has the greatest correlation coefficients for the cylindrical cavity and the torus, and the charge discontinuity estimator has the largest correlation coefficient for the NASA almond. However, the correlation coefficients of the discontinuity estimators are relatively small for the spherical cavity, which will be explained in the next chapter. The normal residual estimator showed poor correlations with the reference error except for the rectangular plate, where the other estimators produced much lower coefficients. The implicit estimator is more strongly correlated with the reference error than the other estimators for the spherical cavity, but totally failed for the NASA almond.

The correlation coefficients for the tangential residual estimator were reasonably large except for the rectangular plate (but note that most estimators produced lower correlations for the plate problem). Considering the consistent performance and heavy computational cost of the tangential residual estimator, it is noteworthy and interesting that the charge discontinuity estimator is strongly correlated with the tangential residual estimator (and thus may provide a cheaper alternative). However, there was one exception when a z-polarized magnetic current is used as the source near the North pole of the spherical cavity. If that

Table 13: Averaged values of the correlation coefficient between reference error and other error estimators for various scatterers.

Geometry	J_t	ρ_e	Res E_t	Res H_n	ρ_{rec}	J_{imp}
Sphere	0.62	0.62	0.80	0.56	0.61	0.84
Cylinder	0.87	0.75	0.74	0.73	0.69	0.72
Plate	0.58	0.44	0.46	0.71	0.32	0.52
Torus	0.91	0.84	0.83	0.59	0.80	0.79
NASA almond	0.82	0.88	0.78	0.51	0.81	0.02

failure can be addressed, then one can achieve a computationally inexpensive and consistent error estimate from the charge discontinuity estimator. This issue will be addressed in Chapter 5.

Based on the correlation coefficients, the current discontinuity estimator produced the best results overall, with the charge discontinuity estimator running in second. It is noteworthy that these estimators are among the cheapest to implement. Chapter 5 will consider the combination of these two estimators in an attempt to improve their performance.

Results of the preceding test cases suggest that the Pearson correlation coefficient is not sufficient to completely evaluate error estimators. As mentioned above, more detailed information can be obtained from the scatter plot and the local error plot. After combining the correlation analysis with these tools, we conclude the following:

1. An error estimator having a correlation coefficient that is close to 1 is likely to imply a reliable and efficient one. As the coefficient approaches 0, the quality of the estimator is degraded. However, this does not mean that error patterns are random and independent in general.

2. The adaptive refinement scheme should use a broadened footprint that includes cells that share nodes with cells in the identified domains. In this way, even when the estimator fails to determine cells with large errors there is a good chance that those cells will be included.

3. The proposed error estimators are strongly correlated with the reference error for most applications. However, every estimator exhibited poor results in at least one case. In those cases, lowering the error criterion or broadening the footprint to include mesh cells adjacent to those identified may not prevent the estimator from missing a large-error cell.

Last but not least, we summarize the elapsed time of the error estimators in Table 14. A computer with an Intel i5-4210U CPU, 8GB of RAM and a Windows 10 64bit home edition operating system is used to measure the elapsed time spent calculating the error estimates. The discontinuity estimators almost instantly give local error values in less than 1 second. The elapsed time of the discontinuity error estimators slightly increases as the number of cells increase. The charge recovery estimator requires few seconds to yield the result of local errors and the elapsed time is almost linearly proportional to the number of cells. The elapsed time for the implicit estimator has also a linear relation to the number of cells, but it demands more calculations than the previously mentioned estimators because it involves quadrature rules and matrix filling. In contrast, both residual estimators are proportional to the square of the number of cells. In particular, the tangential residual estimator is the slowest error estimator for all test cases.

Table 14: The elapsed time of the error estimators.

		Elapsed time [sec]					
Geometry	# of Cells	J_t	ρ_e	Res E_t	Res H_n	ρ_{rec}	J_{imp}
Plate	100	0.62	0.60	805.90	210.24	2.01	811.05
Sphere & Almond	128	0.64	0.62	1441.26	314.55	2.12	1015.50
Torus	256	0.78	0.69	4330.83	1369.06	3.96	2019.59
Cylinder	320	0.86	0.71	6205.46	2210.98	4.86	2669.54

CHAPTER V

COMBINED DISCONTINUITY ERROR ESTIMATOR

5.1 Introduction

Discontinuity error estimators are cheap and accurate to a certain extent: computing the discontinuities in the surface current and surface charge densities require only simple algebraic calculations. These estimators exhibit an $O(N)$ cost that grows linearly with the size of the problem. As seen in the previous chapter, the discontinuity estimators show strong correlations with the reference error in many applications. Based on the averages of the Pearson correlation coefficients, the current discontinuity estimator accurately predicts the actual error for the cylindrical cavity, the torus and the NASA almond. In addition, it shows a reasonable reliability for the rectangular plate case where the other estimators do not. (Although the normal residual estimator has the largest correlation coefficient for the plate problem, it performs poorly for the other geometries, and exhibits an $O(N^2)$ cost.) The charge discontinuity error estimator is also strongly correlated with the reference error for the cylinder, torus, and almond geometries. Moreover, the charge discontinuity estimator shows strong correlations with the tangential residual estimator, which also exhibits consistent performance.

However, the discontinuity estimators did not properly identify the cells containing the largest local errors for the spherical cavity, when a point source is placed near the North pole. In addition, the correlation between the charge discontinuity estimator and the tangential residual estimator was very weak for that geometry, i.e., $\rho_{X,Y} = -0.06$. The inaccuracy due to the failure of the discontinuity estimators can be alleviated by broadening the footprint of the regions considered for adaptive refinement, but at the cost of extra computations. Thus, enhancing the discontinuity estimator's accuracy would be a more desirable approach. In order to do this, we need to understand why the discontinuity estimator did not work properly for the spherical cavity and conceive a new error estimator from the analysis.

Since the discontinuity estimators are known to be inexpensive, improving their precision will achieve one of our goals: to develop an efficient and reliable error estimator.

It is interesting to note that, for the sphere problem, one of the discontinuity error estimators is often strongly correlated with the reference error when the other is not. To be specific, the correlation coefficients of the current discontinuity estimator and the charge discontinuity estimator are 0.05, and 0.74, respectively when an electric current source is close to the North pole of the sphere. The opposite behavior is observed when a magnetic current source replaces the electric current source: The correlation coefficient is 0.85 for the current discontinuity estimator, and 0.35 for the charge discontinuity estimator. From this observation, we deduce that either estimator can fail for certain testing cases, but that a combination based on both the surface current density and the surface charge density may be more successful. We call the resulting estimator the *combined discontinuity* error estimator.

We start by investigating the reason of the failure of the discontinuity estimator for the sphere in the following section. Then, the next section will illustrate how to combine the discontinuity estimators. Two combined discontinuity estimators will be considered. The first one is obtained by simply matching units of the surface current density and the surface charge density, and the other one is obtained by an analogy with the way current and charge appear within the EFIE. The Pearson correlation coefficient will be used to evaluate the combined discontinuity estimators and scattering plots and local error plots will be provided for several examples.

5.2 Analysis of Discontinuity Error Estimators for The Spherical Cavity

Figure 5.1 repeats the local error plot from Fig. 4.4(a) where the current discontinuity estimator is used and an electric current source is placed on the z-axis near the North pole. The cell index and edge index of the interested regions, denoted by a dotted line in Fig. 5.1, are presented in Fig. 5.2(a) and Fig. 5.2(b), respectively. The largest reference error levels occur in cells 16, 32, 48, and 64 while the current discontinuity estimator indicates cells 14, 30, 46, and 62.

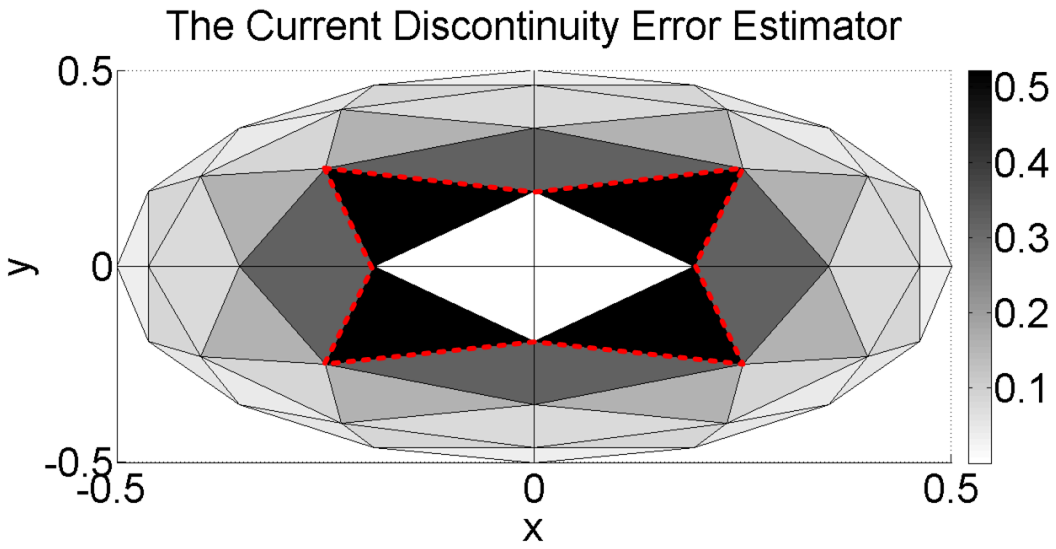

Figure 5.1: A local error plot obtained by the current discontinuity estimator when an electric current source is near the North pole. The cell and edge indices within the dotted line are shown in Fig. 5.2.

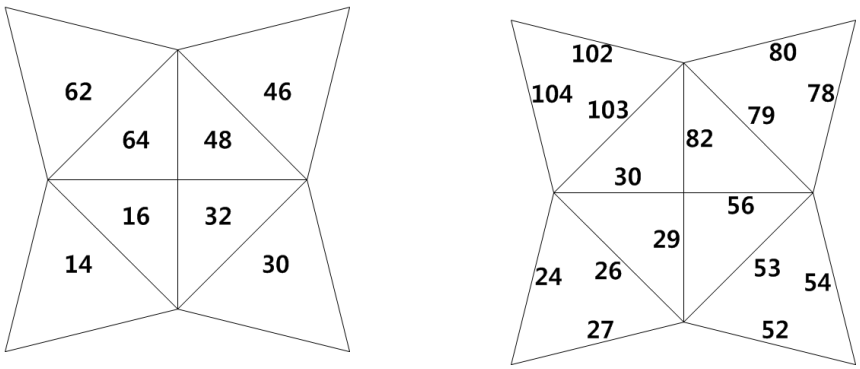

(a) Mesh index.

(b) Edge index

Figure 5.2: Cell and edge indices for the region around the North pole.

Table 15: Current coefficients at edges in Fig. 5.2(b).

Index of edges	Current coefficients
29	$9.2 \times 10^{-11} - j8.3 \times 10^{-10}$
30	$1.1 \times 10^{-9} + j1.0 \times 10^{-9}$
56	$-3.4 \times 10^{-11} + j8.3 \times 10^{-10}$
82	$1.4 \times 10^{-9} + j1.1 \times 10^{-9}$
26	-7.5-j0.24
53	-7.5-j0.24
79	-7.5-j0.24
103	-7.5-j0.24
24	-1.9 - j 0.22
27	1.9 + j 0.22
52	-1.9 - j 0.22
54	1.9 + j 0.22
78	-1.9 - j 0.22
80	1.9 + j 0.22
102	-1.9 - j 0.22
104	1.9 + j 0.22

In order to analyze a malfunction of the current discontinuity estimator, we need to understand how the surface current density is represented. As mentioned in Chapter 2, the surface current density for a given mesh is approximated by the RWG basis functions. The RWG basis functions, as defined in (2.15), correspond to edges. For instance, the surface current density in cell 32, $\bar{J}_{32}$, is a summation of products of the RWG basis functions and current coefficients located at edges 29, 53, and 56. That is,

$$\bar{J}_{32} = I_{29}\bar{B}_{29} + I_{53}\bar{B}_{53} + I_{56}\bar{B}_{56} \tag{5.1}$$

Table 15 shows current coefficients at 16 edges in Fig. 5.2(b). The first 8 coefficients are related to cells 16, 32, 48, and 64 and the others are associated with the adjacent cells. According to the table, the surface current densities of cells 16, 32, 48, and 64 can

be approximated by only one current coefficient and a corresponding basis function, i.e., $\bar{J}_{32} \approx I_{53}\bar{B}_{53}$, and because of symmetry in the mesh and excitation the surface current densities in those cells are identical to one another.

Then, let us evaluate the local error in cell 32 using the current discontinuity estimator. This error is defined in (3.3). The current discontinuity estimator measures the discontinuities of the surface current densities at the mid-point of each edge around a given cell and averages their values to obtain the local error for that cell. Remember that it is sufficient to use the tangential components of the surface current densities because the RWG basis functions enforce the continuity of normal components across the edges. For the local error in cell 32, the discontinuities are measured at the mid-point of edges 29, 53, and 56. In equation form,

$$\mathrm{LE}^{32}_{J_{\tan}} = \frac{\hat{t}_{29}\cdot(\bar{J}_{32}-\bar{J}_{16}) + \hat{t}_{53}\cdot(\bar{J}_{32}-\bar{J}_{30}) + \hat{t}_{56}\cdot(\bar{J}_{32}-\bar{J}_{48})}{3\max_i|\bar{J}_i|} \tag{5.2}$$

Note that $\bar{J}_{32}$ depends on coefficients I_{29}, I_{53}, and I_{56} while $\bar{J}_{16}$ depends on coefficients I_{26}, I_{29}, and I_{30}. The first term on the right-hand side of (5.2) is almost 0, because I_{26} and I_{53} are the same and I_{29}, I_{30}, and I_{56} are essentially zero. The same reasoning applies to the third term. The second term is also approximately 0 because the current densities, $\bar{J}_{32}$ and $\bar{J}_{30}$ have $I_{53}\bar{B}_{53}$ in common and I_{52} and I_{54} have the same magnitude and the opposite signs to each other:

$$\begin{aligned}
\bar{J}_{32}-\bar{J}_{30} &= I_{53}\bar{B}_{53} + I_{56}\bar{B}_{56} + I_{29}\bar{B}_{29} && \leftarrow I_{29}, I_{56} \approx 0 \\
&\quad - I_{53}\bar{B}_{53} + I_{52}\bar{B}_{52} + I_{54}\bar{B}_{54} && \leftarrow I_{54} = -I_{52} \\
&\approx 0
\end{aligned} \tag{5.3}$$

Similarly, we can show that the local errors in cells 16, 48, and 64 are also 0.

The reason that the current discontinuity estimator produces zeros at cells around the North pole is that a z-component electric current source produces only a $\hat{\theta}$-component electric field [13], and the mesh is uniform and symmetric around the North pole. First of all, the fact that the current density has only one component forces current coefficients including I_{29}, I_{30}, I_{56} and I_{82} to be close to 0. Then, the symmetry and uniformity of

the mesh results in the same current coefficients at edges 26, 53, 79, and 103. Finally, the tangential components of the current densities at edges 26, 53, 79, and 103 are approximately the $\hat{\phi}$-component, and this yields two current coefficients having the same magnitude and the opposite signs to each other, i.e., $I_{54} = -I_{52}$. At cells farther away from the North pole, representations of the surface current density become more complicated, with both $\hat{\theta}$ and $\hat{\phi}$ components, which generates discontinuities along edges. Then, the current discontinuity estimator starts to work accurately. The charge discontinuity estimator produces zeros of local errors around the North pole for magnetic sources for similar reasons.

5.3 Combined Discontinuity Error Estimator

From the previous section, we can see that the discontinuity estimators may fail under certain conditions, when the quantities they work with are forced to cancel by the symmetry of the geometry or the source. However, we also observe that the two estimators fail under different conditions. This suggests that an estimator based on both quantities may be more robust. Hence, the following sections will illustrate techniques for combine the current discontinuities and the charge discontinuities. These combined discontinuity error estimators are motivated by aligning the units of quantities or by an analogy with the EFIE.

5.3.1 Unit Matching Type

The current discontinuity estimator involves a dot product with a unit vector that is tangential to a given edge and computes the difference between the current densities in the two cells sharing that edge. The unit of the surface current is ampere per meter, [A/m], while the tangential vector is unitless. The first combined discontinuity estimator, named the "unit matching type" of estimator, replaces the unit tangential vectors with vectors in the same directions but with lengths scaled to the length of the corresponding edges. Hence, the resulting unit of current discontinuity is ampere. For charge discontinuities, the estimator uses Maxwell's continuity equation,

$$\nabla \cdot \bar{J} = -j\omega\rho \tag{5.4}$$

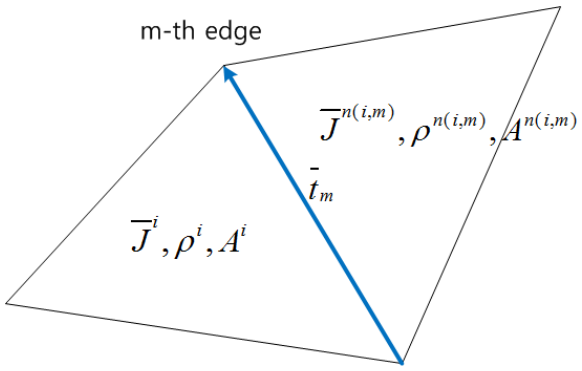

Figure 5.3: A scheme of the combined discontinuity error estimator of unit matching type.

where ω is the angular frequency. The quantity in (5.4) has a unit of ampere per square meter, [A/m^2]. In order to match units of both discontinuities, (5.4) is multiplied by the area of the triangular cell, used to compute the charge discontinuity, and added to the scaled current discontinuity. The combined discontinuities are normalized by the maximum value of a dot product between the incident field and the tangential vector.

The local cell-based error from the combined discontinuity error estimator of the unit matching type at cell i-th is defined as:

$$\mathrm{LE}^{i}_{\mathrm{Comb}_{UM}} = \frac{\frac{\eta}{3}\sum_{n=1}^{3}\left|\bar{t}_m \cdot \left(\bar{J}^{i} - \bar{J}^{n(i,m)}\right)\right| + \omega\left|A^{i}\rho^{i} - A^{n(i,m)}\rho^{n(i,m)}\right|}{2\max\left|\bar{t}_m \cdot \bar{E}^{inc}\right|} \tag{5.5}$$

where i is the index of the given cell, m is the local index of the edges of cell i, and $n(i,m)$ is the neighbor cell of edge m and cell i. The numerator of (5.5) is multiplied by the intrinsic impedance, η, to cancel the unit of the denominator. Since the estimator measures two different discontinuities, we divide the local error by 2. Lastly, A^i is the area of the i-th cell.

5.3.2 The EFIE Type

The second combined discontinuity estimator is named the "EFIE type" of estimator. This estimator is obtained by combining the current and charge in the same form that they appear within the EFIE. The EFIE is written as:

$$\bar{E}^{inc} = jk\eta\left(\bar{J} * G\right) + \frac{1}{\epsilon}\nabla\left(\rho * G\right). \tag{5.6}$$

The estimator is obtained by removing the Green's functions (G), and the convolution operators ($*$) from (5.6) and then, by applying the razor-blade testing functions. Thus, the local error of the combined discontinuity error estimator of the EFIE type for cell i is given by:

$$\mathrm{LE}^i_{\mathrm{Comb}_{EFIE}} = \frac{\frac{1}{3}\sum_{n=1}^{3}\left|jk\eta\left(\bar{T}^i_m \cdot \bar{J}^i + \bar{T}^{n(i,m)}_m \cdot \bar{J}^{n(i,m)}\right)\right| + \left|\frac{\rho^i - \rho^{n(i,m)}}{\epsilon}\right|}{\max\left|\bar{E}^{inc}\right|} \tag{5.7}$$

The subscripts m and superscripts i and $n(i,m)$ are identical to those of the unit matching type.

5.4 Numerical Results

The Pearson correlation coefficients for the discontinuity error estimators are shown in Tables 16-20. Geometries, source polarizations, source positions, and source types of the test problems are identical to the previous chapter. The correlation coefficients for the current discontinuity estimator (J_t) and the charge discontinuity estimator (ρ_e) are also provided for comparison with the combined discontinuity estimators. In the tables, the unit matching type and the EFIE type are denoted as Comb_{UM}, and Comb_{EFIE}, respectively.

When the point source is on z-axis and is close to the North pole (see Table 16), the correlation coefficients for the combined discontinuity estimators are greater than the smallest of the two existing discontinuity estimators, especially when they yield low correlation coefficients. For an electric current source near the North pole (the first row in Table 16), the correlation coefficients for the combined discontinuity estimators are greater by at least 0.4 than the current discontinuity estimator. Given a magnetic current source around the

Table 16: Correlation coefficients between the reference error and the discontinuity error estimators for the spherical cavity.

Src.	Pos.	J_t	ρ_e	Comb_{UM}	Comb_{EFIE}
J_z	①	0.05	0.74	0.45	0.69
J_z	②	0.95	0.76	0.91	0.85
M_z	①	0.85	0.35	0.85	0.82

Table 17: Correlation coefficients between the reference error and the discontinuity estimators for the cylindrical cavity.

Src.	Pos.	J_{t}	ρ_{e}	Comb_{UM}	Comb_{EFIE}
J_z	①	0.94	0.63	0.92	0.71
J_z	②	0.94	0.75	0.92	0.81
J_z	③	0.88	0.70	0.91	0.73
M_z	①	0.80	0.85	0.81	0.89
M_z	②	0.88	0.88	0.88	0.95
M_z	③	0.74	0.74	0.77	0.78
J_x	①	0.95	0.62	0.93	0.69
J_x	②	0.86	0.81	0.86	0.84
J_x	③	0.81	0.79	0.86	0.81

North pole (the third row in Table 16), the correlation coefficients for the combined discontinuity estimators are greater by 0.47 than the coefficient for the charge discontinuity estimator. For a z-polarized electric current source that is located on the x-axis, the correlation coefficients for the combined discontinuity estimators lie between those of the current discontinuity estimator and the charge discontinuity estimator, but both are reasonably large as shown in the second row of the Table 16.

When applied to the cylindrical cavity test problem, both the current discontinuity estimator and the charge discontinuity estimator produce strong correlations with the reference error as well as the combined discontinuity estimators as shown in Table 17. The correlation coefficients of the combined estimators usually produce values between those of the existing discontinuity estimators, but there are several cases where the coefficients of the combined discontinuity estimators are greater than those of the existing discontinuity estimators. In addition, the coefficients of the unit matching combined estimator are larger than those of the EFIE type for electric current sources. Given magnetic current sources, however, the coefficients of the EFIE type are greater than those of the unit matching type.

From Table 18, we can see that the correlation coefficients of the combined discontinuity

Table 18: Correlation coefficients between the reference error and the discontinuity estimators for the rectangular plate.

Src.	Pos.	J_{t}	ρ_{e}	Comb_{UM}	Comb_{EFIE}
J_z	Plane wave	0.49	0.31	0.53	0.76
J_z	①	0.70	0.59	0.81	0.64
J_z	②	0.54	0.41	0.58	0.45

Table 19: Correlation coefficients between the reference error and the discontinuity estimators for the torus.

Src.	Pos.	J_{t}	ρ_{e}	Comb_{UM}	Comb_{EFIE}
J_z	①	0.89	0.78	0.89	0.86
J_z	②	0.91	0.87	0.92	0.88
J_z	③	0.93	0.88	0.97	0.91

Table 20: Correlation coefficients between the reference error and the discontinuity estimators for the NASA almond.

Src.	Pos.	J_{t}	ρ_{e}	Comb_{UM}	Comb_{EFIE}
J_z	①	0.87	0.96	0.95	0.98
J_z	②	0.90	0.96	0.93	0.99
J_z	③	0.70	0.71	0.76	0.72

estimators are also increased for the rectangular plate cases. For a plane wave excitation, the correlation coefficients of the combined discontinuity estimators are 0.53, and 0.76, which are greater than the coefficient of the current discontinuity estimator by at least 0.04. This implies that the combined discontinuity estimators may have similar or higher level of accuracy and efficiency when comparing with the current discontinuity estimator. When an electric current source is on either the corner or the center of the plate, the coefficients of the combined discontinuity estimator of unit matching type are larger or similar to the current discontinuity estimator while the coefficients of the EFIE type produce values between the existing discontinuity estimators.

Similar to the cylindrical cavity, the torus and the NASA almond test cases yield strong correlations between the reference error and the discontinuity estimators, as shown in Table 19 and Table 20. The combined discontinuity estimators produce correlation coefficients either lying between those of the existing discontinuity estimators, or greater than them.

In order to illustrate the improvement in the combined discontinuity estimators, we explore several examples where the current discontinuity estimator or the charge discontinuity estimator was unable to determine large error domains. The first example is the spherical cavity when an electric current source is on the z-axis, close to the North pole. The scatter plots and the local error plots for the current discontinuity estimator and the combined discontinuity estimators are given in Fig. 5.4. Again, due to the uniformity and the symmetry of the meshes, 4 points in the scatter plot overlap one another and therefore, they are seen as one point in the plot.

According to Fig. 5.4(a), the scatter plot for the current discontinuity estimator indicates that the estimator identifies 8 lower-error cells instead of the 4 cells containing the greatest reference error. The combined discontinuity estimator of the unit matching type removes 4 unnecessary cells and produced increased error values in the cells with greatest reference error as compared to the current discontinuity estimator, as shown in Fig. 5.4(b). Thus, the unit matching estimator gives a better error estimate than the current discontinuity estimator. The combined discontinuity estimator of the EFIE type yields even better performance than the other estimators. The scatter plot in Fig. 5.4(c) shows that the EFIE

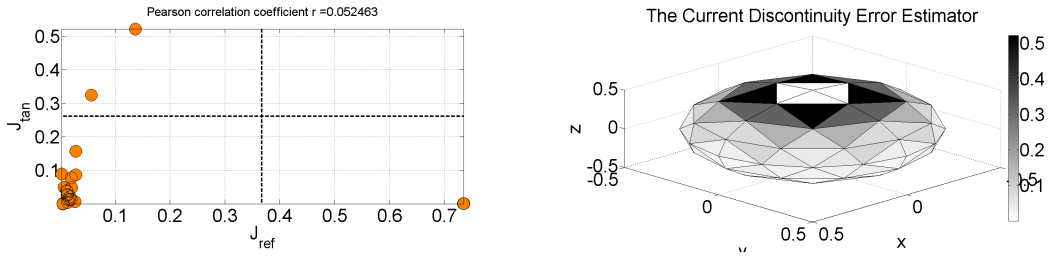

(a) A local error plot and a scatter plot for the current discontinuity estimator.

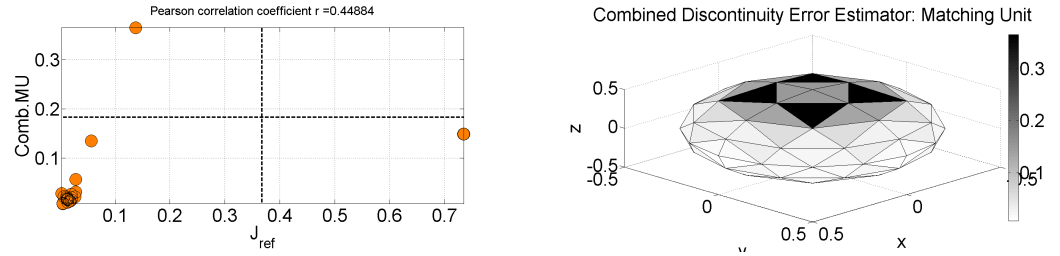

(b) A local error plot and a scatter plot for the combined discontinuity estimator of the unit matching type.

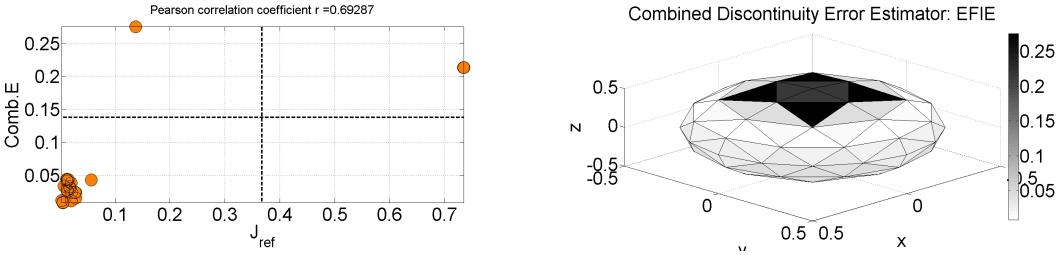

(c) A local error plot and a scatter plot for the combined discontinuity estimator of the EFIE type

Figure 5.4: Local error plots and scatter plots of the spherical cavity when a z-polarized electric current source is at the North pole (①).

estimator correctly identifies the cells with the largest errors.

Figure 5.5(a) gives the scatter plot and the local error plot for the charge discontinuity estimator when a magnetic source is placed near the North pole of the sphere test problem. The correlation coefficient for the charge discontinuity estimator is 0.35, which is greater than that of the current discontinuity estimator for an electric current source. However, the situation is similar the previous case: the estimator misses the 4 cells having the largest local errors, but includes 8 cells with lower errors. When observing the scatter plots and the local plots in Fig. 5.5(b) and Fig. 5.5(c), both combined discontinuity estimators not only identify the largest-error cells but also exclude superfluous cells. Because of this, the correlation coefficients of the combined discontinuity estimators are greater than 0.81.

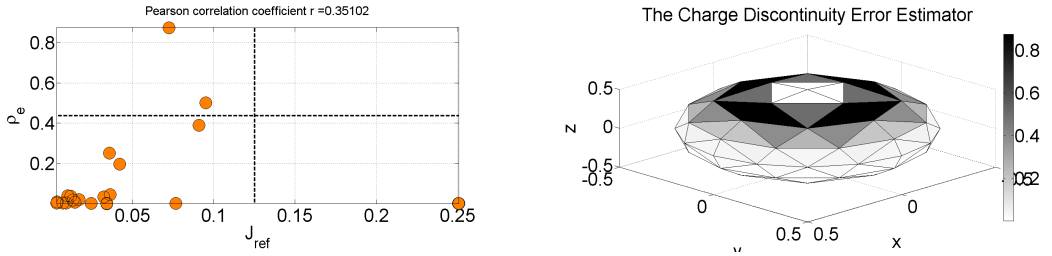

(a) A local error plot and a scatter plot for the current discontinuity estimator.

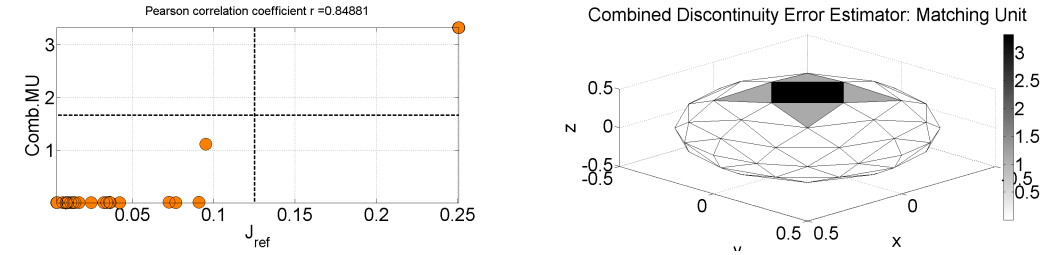

(b) A local error plot and a scatter plot for the combined discontinuity estimator of the unit matching type.

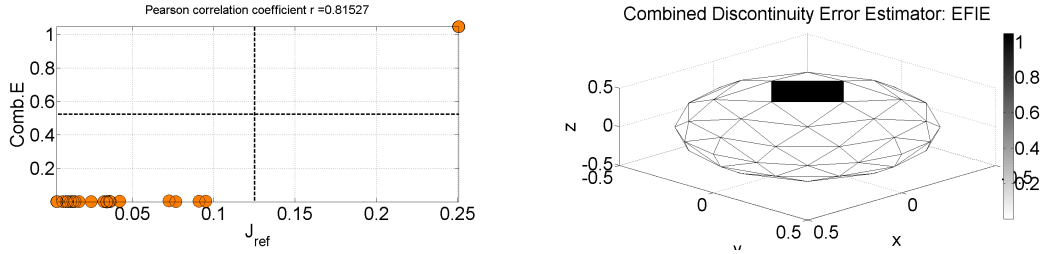

(c) A local error plot and a scatter plot for the combined discontinuity estimator of the EFIE type

Figure 5.5: Local error plots and scatter plots of the spherical cavity when a z-polarized magnetic current source is at the North pole (①).

5.5 Concluding Remarks

In this chapter, we studied the current discontinuity estimator for the spherical cavity test case where an electric current source is close to the North pole in order to understand why the estimator fails to identify large error regions. Current discontinuities along the edges around the North pole are canceled by source polarizations combined with the geometric characteristics and mesh formations. Based on the analysis, we postulated that the current and charge discontinuities can be combined to determine large error domains and we proposed two new discontinuity error estimators. The first one is called the combined discontinuity error estimator of the unit matching type, which unified units of the surface current density and the surface charge density. The second is referred as to the combined discontinuity error estimator of the EFIE type because the estimator is formed by analogy

Table 21: Averaged values of the correlation coefficient between reference error and the discontinuity estimators for various scatterers.

Geometry	J_{t}	ρ_{e}	Comb_{UM}	Comb_{EFIE}
Sphere	0.62	0.62	0.74	0.79
Cylinder	0.87	0.75	0.87	0.80
Plate	0.58	0.44	0.64	0.62
Torus	0.91	0.84	0.93	0.88
NASA almond	0.82	0.88	0.88	0.90

with the EFIE.

We compared the performance of the combined discontinuity estimators with the existing discontinuity estimators for the test problems where the existing estimators failed. Table 21 summarizes the averaged correlation coefficients of all discontinuity estimators for the full suite of test problems considered in Chapter 4. The correlation coefficients for the combined discontinuity estimators are larger than the others by more than 0.12 for the spherical cavity cases. In addition, using the scatter plots and the local error plots we confirmed that the efficiency and the accuracy of the combined discontinuity estimators are better for the sphere. For the other test cases, the combined discontinuity estimators produce correlation coefficients, which are greater or are between the coefficients of the existing discontinuity estimators.

CHAPTER VI

ADAPTIVE h-REFINEMENT IN THE METHOD OF MOMENTS

6.1 Introduction

Adaptive refinement is an iterative procedure to achieve precise numerical solutions by changing mesh sizes or increasing representation orders over certain regions. The specified regions are usually determined by an error estimator, as studied throughout the previous chapters. After refining the discretization in the regions with large errors, new numerical solutions are obtained for the modified problem. Then, the local errors across the entire domain are estimated again. The process is repeated until the level of error is under a prescribed error criterion throughout the mesh. Adaptive refinement can be classified based on how it re-defines the given problem. It is called h-refinement if it works by adjusting the mesh and it is called p-refinement if it works by adjusting the order of the basis functions.

In this chapter, we illustrate a simple implementation of adaptive h-refinement for the 3D method of moments. First, regions with large error are identified by an error estimator. Second, additional nodes are generated in cells around the large error domains. Third, a refined mesh is formed incorporating the new and existing nodes by means of the advancing front Delaunay triangulation algorithm. Finally, the cells in the new mesh are regularized by Laplacian smoothing to improve their shape. We define the regularity of a triangular cell by how close it is to an equilateral triangle (the quality factor introduced in Chapter 2).

Numerical results are given and discussed to illustrate the adaptive refinement procedure. A global error will be defined as a weighted average of local errors in order to confirm that the numerical solutions have converged. Error estimators including the current discontinuity error estimator, the combined discontinuity error estimator of the EFIE type, and the tangential residual error estimator are tested for the cavity test problems described in the previous chapters. Furthermore, we will compare results obtained from the adaptive

refinement with those obtained from a uniform mesh refinement to justify that the adaptive refinement is an efficient and reliable method to improve the accuracy of the numerical solutions.

6.2 The Adaptive h-Refinement Algorithm

This section illustrates how to form refined meshes from the existing meshes. The algorithm begins by classifying meshes and distributes nodes based on the mesh class. Then, it removes all connectivities of the involved meshes such as mesh-to-node connectivities, mesh-to-edge connectivities, and edge-to-node connectivities. The new connectivities are generated from the created nodes and the existing nodes by the advancing front Delaunay triangulation algorithm. Since the quality of the mesh can deteriorate in this procedure, the algorithm also executes Laplacian smoothing, which adjusts node positions by taking averages of adjacent nodes to improve cell shapes.

6.2.1 Mesh Refinement Scheme

The first step of the process is to identify the actual regions needing refinement. For this we use an error estimator. Based on the analysis of error estimators in Chapter 4 and Chapter 5, we saw that error estimators sometimes missed large-error cells, and that it was not always effective to (1) reduce the prescribed error criterion of the error estimators or (2) include adjacent cells that only share edges with the identified regions. Instead, we concluded that the adaptive refinement should also include cells that share nodes with cells in the large-error region. To illustrate this approach, Figure 6.1 shows an example of our mesh refinement scheme for the case when two cells are identified by an error estimator. The identified cells are shaded, while other cells sharing nodes with the large-error cells denoted in white.

The second step of the refinement process is the addition of new nodes to the mesh. The new nodes are generated according to the following algorithm:

1. For the large-error cells identified by the estimator, nodes are added at the mid-point of the edges.

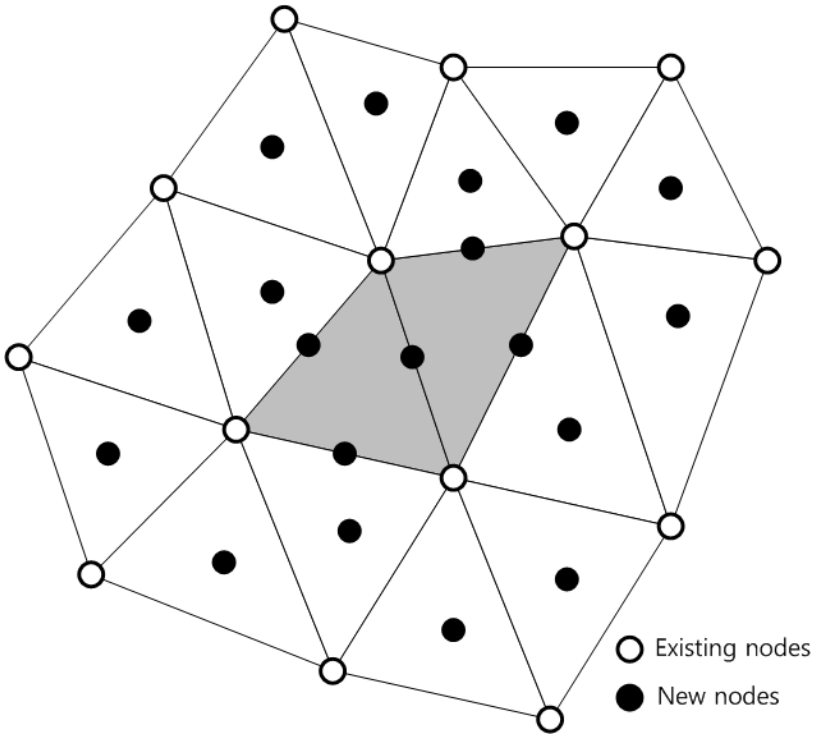

Figure 6.1: Cells and nodes illustrating mesh refinement.

2. For the cells sharing nodes with the identified cells, nodes are added at the cell centroids.

For illustration, white dots in Figure 6.1 represent the original nodes while black dots denote the created nodes.

6.2.2 Advancing Front Delaunay Triangulation

Delaunay triangulation is an algorithm that creates a triangular mesh, with cell shapes optimized based on the circle criterion. The advancing front Delaunay triangulation is one of several methods to accomplish it. Thus, it is necessary to understand the Delaunay triangulation before proceeding to its specific algorithm. We refer notations, definitions, lemmas, and corollaries associated with the Delaunay triangulation on [65], [66], and [67] and summarize them as the follows. Our description of the Delaunay procedure is limited to triangles in two dimensions, but it can also be extended to tetrahedral cells in three dimensions.

Consider a set of distinct points $V = \{v_1, v_2, \ldots, v_N\}$ $(N \geq 3)$, in the Euclidean space,

a set of all possible edges $E = \{e_1, e_2, \ldots, e_M\}$ ($M = \binom{N}{2}$) between two vertices in V, and Euclidean distance $d(v_i, v_j)$ between points v_i and v_j.

Definition 6.1. Two edges $e_1, e_2 \in E$, $e_1 \neq e_2$ are said to properly intersect if they intersect at a point other than their endpoints.

Definition 6.2. A triangulation of a V is a planar straight-line graph $G(V, E')$ for which E' is a maximal subset of E such that no two edges of E' properly intersect.

Definition 6.3. The region

$$R(i) = \{x \in \mathbb{R}^2 | d(x, v_i) \leq d(x, v_j), j = 1, 2, \ldots, N, \text{ and } i \neq j\} \tag{6.1}$$

which is the locus of points closer to vertex v_i than to any other vertex, is called the Voronoi polygon associated with the vertex v_i.

Voronoi polygons can be explained by an analogy with a growing process. Suppose that vertices in V are nuclei of growing cells. Assume further that each growth speed of the cell is the same and the growth direction is isotropic. In other words, the cell shape at the early stage of the growth is a circle in the two-dimensional plane. As cells continue to expand, they start to collide at the mid-points between two neighboring cells and those cells stop growing in the direction of the collisions. After the first contact, they start to form common edges of two growing Voronoi polygons. These edges are called Voronoi edges, and Voronoi polygons that share Voronoi edges are called Voronoi neighbors. Note that any points on a given Voronoi edge are equidistant from the nuclei of the Voronoi neighbors of that edge.

The Voronoi edge continues to stretch until it encounters another Voronoi edge from a third growing cell. The point of contact of these edges is said to be a Voronoi point. Since the distances between the Voronoi point and three Voronoi nuclei are identical to one another, the Voronoi point is the center of the circumscribed circle of the triangle formed by the three nuclei. The growing nuclei of all Voronoi neighbors result in areas consisting of tessellated triangles within the convex hull of the point set. This tessellation is called the Delaunay triangulation $DT(V)$ of V.

An example of the Voronoi polygons and the Delaunay triangulation is shown in Fig. 6.2. White dots are nuclei of growing cells, which are the nodes of triangles constructed by

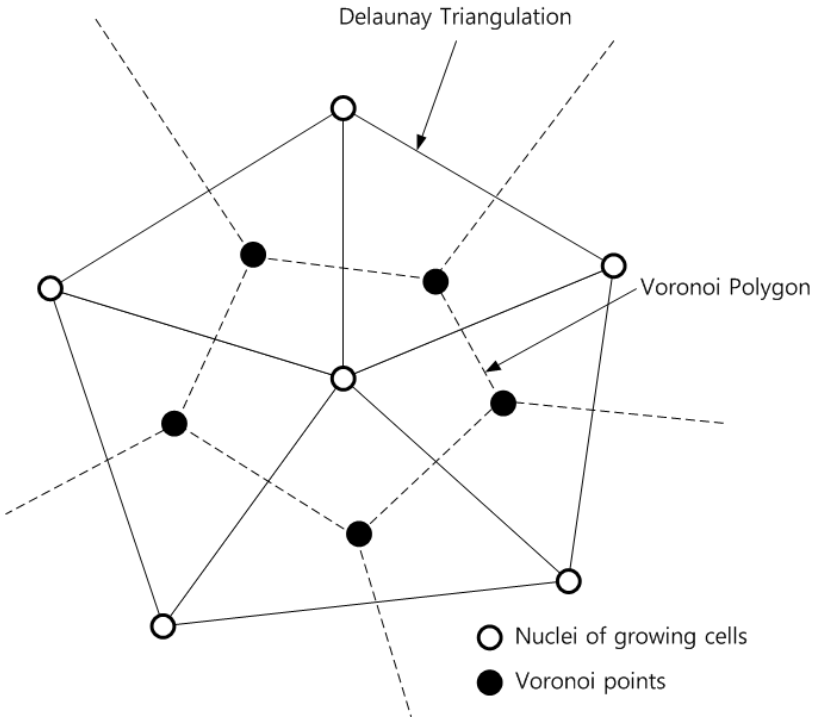

Figure 6.2: Voronoi polygons and Delaunay triangulation.

the Delaunay triangulation. The edges of the triangles are called the Delaunay edges and they are denoted as solid lines. On the other hand, black dots are the Voronoi points and dotted lines are the Voronoi edges. Lastly, the polygon formed by dotted lines in Fig. 6.2 is the Voronoi polygon.

The following lemmas, and a corollary are useful in the implementation of the Delaunay triangulation.

Lemma 6.4. Given a set V of N points, any triangulation $T(V)$ has the same number of triangles:

$$N_t = 2(N-1) - N_h \tag{6.2}$$

where N_h is the number of points on the convex hull of V. Moreover, $T(V)$ has the same number of edges:

$$N_e = 3(N-1) - N_h \tag{6.3}$$

Lemma 6.5. Given a set $V = \{v_1, v_2, \ldots, v_N\}$ of points, $\Delta v_i v_j v_k$ is a Delaunay triangle of $DT(V)$ if and only if its circumscribed circle does not contain any other point of V in its interior.

Lemma 6.4 can be used to verify that the Delaunay triangulation generates triangular meshes properly. This is because (due to programming errors) the algorithm can generate the same triangular cells repeatedly even for trivial mistakes and those errors are hard to distinguish by an inspection of the mesh. The mesh illustrated in Fig. 6.1, for instance, has 10 nodes on the convex hull (or on the boundary) and 33 nodes in total. Hence, the number of created cells should be 54 and the number of generated edges should be 86 by (6.2) and (6.3). If the mesh appears to be fine but the corresponding numbers are not 54 and 86, then it implies that there is a problem with the implementation of the algorithm.

Lemma 6.5 is called the circle criterion, which determines whether a triangular cell should be formed or not. It means that a candidate triangle is not allowed to be created if the circumscribed of the mesh contains any nodes inside. Otherwise, the cell is considered as a validated Delaunay triangle and it will be generated.

We note that the Delaunay procedure chooses the optimal triangles (in terms of their shape) for a given set of starting nodes. If the set of nodes is very non-uniform, the resulting mesh may exhibit elongated cells of poor quality (cells that are very unlike equilateral triangles in shape). The Delaunay procedure does not adjust the node positions to improve the cell shapes.

Having summarized the theory, it is necessary to describe how to produce Delaunay triangular meshes in practice. The algorithm we employ is called the advancing front Delaunay triangulation because it constructs one triangular cell at a time and the edge segment on the boundary is advanced after it is used for creating the cell. The set of edge segments forming the boundary is called a front, and this is why the approach is called the advancing front triangulation. For our purposes we assume that the region being refined is entirely interior to the mesh; in other words the front surrounds a closed region.

Figure 6.3 explains the process of the advancing front Delaunay triangulation. The set of edge segments is referred to as the front and is depicted as solid lines. The front forms a polygon in our problem. Nodes located on the front are called boundary nodes, and white dots represent them. Let us begin by selecting an edge on the front as shown in Fig. 6.3(a). The chosen edge segment is denoted by a red dashed line. Except for

nodes that are end-points of the selected edge, any node can be a candidate to form a triangle. We only consider the three black dots in Fig. 6.3(a) as possible nodes. These are called interior nodes because the front has them inside. In order to determine a Delaunay triangular mesh, the algorithm chooses an arbitrary interior node and makes a triangle with the interior point and the two end-points of the selected edge. If the circumscribed circle of this triangle contains any other nodes, this is not a legitimate Delaunay triangle. In that situation the algorithm selects another node and repeats the circle test until it finds a node where the circumscribed circle of the triangle, formed by the node and the two end-points of the selected edge, contains no other nodes inside. This iterative process is said to be the circle test, as discussed in Lemma 6.5. Examples of the circle test are shown in Fig. 6.3, where circles with solid lines correspond to the valid Delaunay triangles. Circles made with dashed lines contain at least one node inside, and triangles formed by three nodes on those circles are not allowed.

After generating a Delaunay triangle, the selected edge segment is deleted and the new edges are added to the front. Note that it is possible to form a Delaunay triangle from three boundary nodes. We can see this in Fig. 6.3 (b) and Fig. 6.3(c). Although a Delaunay triangle cannot be formed in Fig. 6.3(b) because the circumscribed circle of the triangle with three boundary nodes contains an interior node, it is possible in the next stage as shown in Fig. 6.3(c). The algorithm is terminated when the front does not have any other edge segments.

However, there is a situation when the circle test alone is not enough to determine a unique Delaunay triangle. The problem is illustrated in Fig. 6.4. For a given edge segment, depicted as a red dashed line, two boundary nodes pass the circle test simultaneously. One will form a valid Delaunay triangle, which is denoted by a solid circle, but the other will generate and overlap the existing mesh. In order to prevent this situation from occurring, we observe that the front is a closed polygon and therefore, we can distinguish between the inside and outside of the polygon. Suppose that we take sample points in the two possible triangular cells. The point in the legitimate Delaunay triangle is contained in the polygon while the one in the existing mesh is outside the polygon. Hence, the problem can be

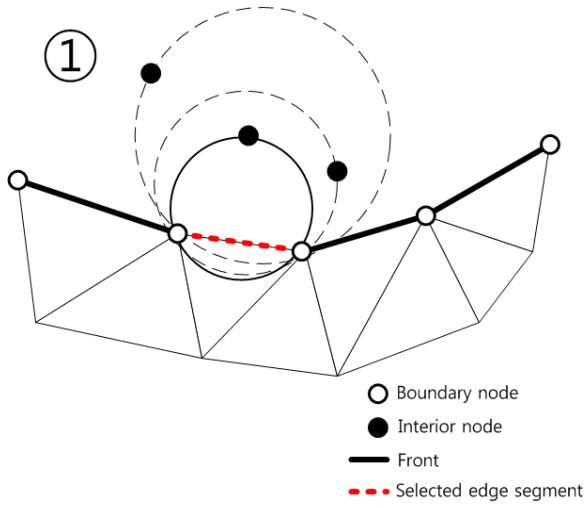

(a)

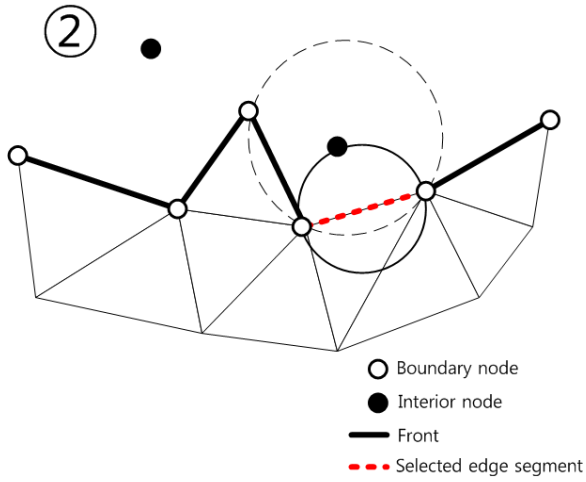

(b)

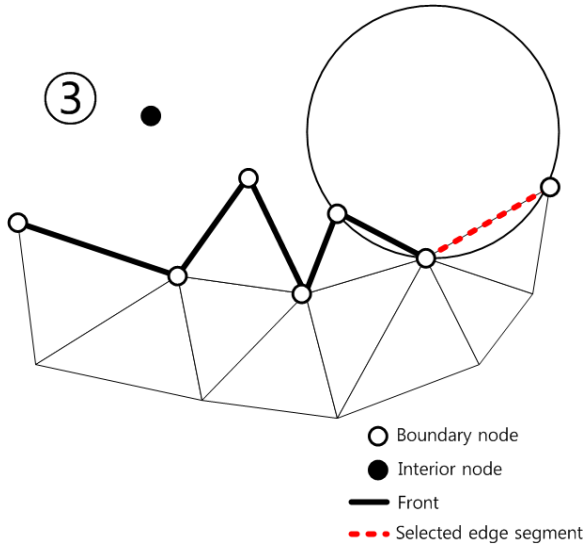

(c)

Figure 6.3: Illustration of the advancing front Delaunay triangulation.

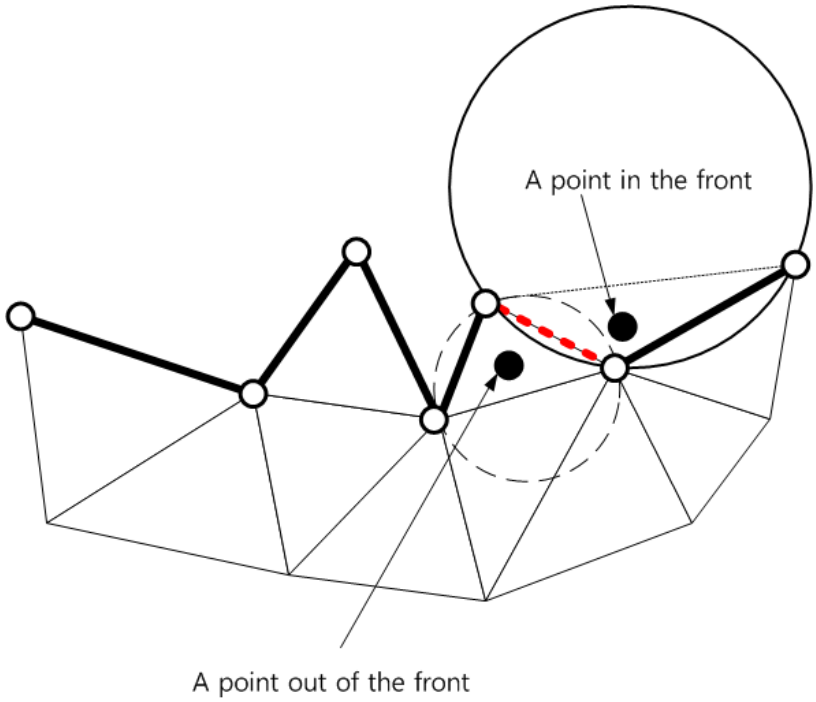

Figure 6.4: A case when only the circle test is not sufficient to generate the Delaunay triangle.

addressed if the algorithm is able to determine whether a sample point is inside the polygon or not, and this can be determined by using the winding number algorithm [75], [76].

The winding number $w_n(\bar{P}, C)$ is defined as the total number of times that a closed curve travels counterclockwise around a point. Consider a closed parametrized curve C and a point P, which is not on C. Let us define a unit vector $\bar{w}(\bar{P}, t) = \bar{C}(t) - \bar{P}/|\bar{C}(t) - \bar{P}|$ where $\bar{P}$ is the position vector of the point P and $\bar{C}(t)$ is the position vector of the point on C for given t. Since the vector $\bar{w}(\bar{P}, t)$ maps a point $\bar{C}(t)$ on C to a point on the unit circle, it can be represented in polar coordinates $(\cos\theta(t), \sin\theta(t))$ where $\theta(t)$ is a positive counterclockwise angle. Then the winding number is given by

$$w_n(\bar{P}, C) = \frac{1}{2\pi} \oint_{t=0}^{1} \theta(t) dt \tag{6.4}$$

If a point is inside the closed curve, then the winding number is greater or equal to 1, depending on how many turns the curve has. If the point is outside the curve, the winding number is 0. For a closed polygon with nodes $v_1, v_2, \ldots v_N = v_0$, the winding number

$w_n(\bar{P}, C)$ in (6.4) and the unit vector $\bar{w}(\bar{P}, t)$ can be rewritten as

$$w_n(P, C) = \frac{1}{2\pi} \sum_{i=0}^{N-1} \text{sign}(i) \arccos \left[\frac{(\bar{v}_i - \bar{P}) \cdot (\bar{v}_{i+1} - \bar{P})}{|\bar{v}_i - \bar{P}||\bar{v}_{i+1} - \bar{P}|} \right] \tag{6.5}$$

$$\bar{w} = \frac{(\bar{v}_0 - \bar{P}) \times (\bar{v}_1 - \bar{P})}{|\bar{v}_0 - \bar{P}||\bar{v}_1 - \bar{P}|} \tag{6.6}$$

where $\bar{v}_i$ $(i = 0, 1, 2, \ldots, N)$ is the position vector of node v_i, and

$$\text{sign}(i) = \begin{cases} +1 & \text{if } \bar{w} \cdot \left[(\bar{v}_i - \bar{P}) \times (\bar{v}_{i+1} - \bar{P}) \right] > 0 \\ -1 & \text{if } \bar{w} \cdot \left[(\bar{v}_i - \bar{P}) \times (\bar{v}_{i+1} - \bar{P}) \right] < 0 \end{cases} \tag{6.7}$$

Note that the winding number in our application will be either 1 or 0.

6.2.3 Regularity of Triangular Meshes and Laplacian Smoothing

The iterative h-refinement can yield meshes of poor quality: it repeatedly divides given triangles into several smaller cells, which can produce a triangle with one side much longer than another, or a triangle with interior angles close to zero or 180 degrees. Such cells may result in poor accuracy and slow convergence of the numerical solution [68]. Hence, our goal in this subsection is to evaluate and improve the quality of triangular meshes. In order to do that, we will introduce the quality factor of the triangle and the Laplacian smoothing algorithm.

The quality factor, Q, of a triangle measures how close a given triangle is to an equilateral triangle. Q is defined as the ratio of twice the radius of the inscribed circle of the triangle, r_i, to the radius of the circumscribed circle of the triangle, R_c:

$$Q = 2\frac{r_\text{i}}{R_\text{c}} = \frac{(b + c - a)(c + a - b)(a + b - c)}{abc}, \quad 0 < Q \leq 1 \tag{6.8}$$

where a, b and c are the side lengths of the triangle. The factor of 2 normalizes the quality factor to 1 in the ideal case of an equilateral triangle. The quality factor has a maximum value of 1, and it decreases to 0 as one angle of the triangle approaches 180°.

Laplacian smoothing is a simple way to alleviate degradation of mesh quality by reshaping triangles. The process iteratively adjusts a node position by shifting it to the average of its adjacent nodes. In equation form, it is expressed as:

$$\bar{v}_0 = \frac{1}{N} \sum_{j=1}^{N} \bar{v}_j \tag{6.9}$$

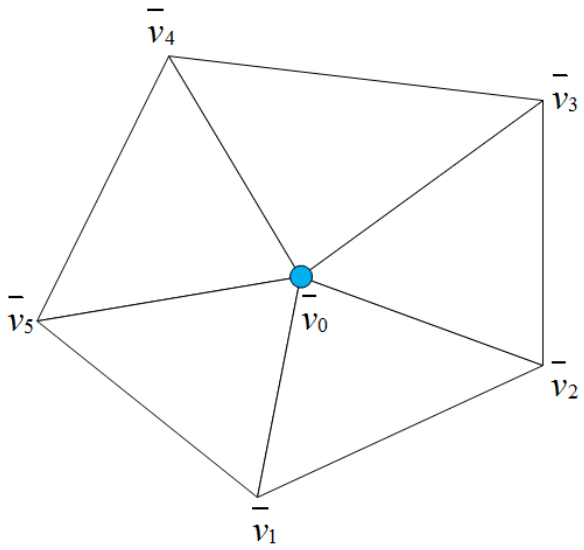

Figure 6.5: The idea behind Laplacian smoothing.

where $\bar{v}_0$ is the position vector of the node to be varied, and v_j $(j = 1, 2, \ldots, N)$ are the position vectors of the neighboring nodes. If the nodes all lie in a plane, as shown in Fig. 6.5, this is straightforward. If however, the nodes are on a curved or bent surface in 3D, averaging may shift a node off the original surface. Consequently, a geometric constraint must be applied to the adjusted node during the iteration. For instance, a node $v_i = (x_i, y_i, z_i)$ on the sphere with radius a must satisfy $x_i^2 + y_i^2 + z_i^2 = a^2$. The Laplacian smoothing stops when the maximum displacement of the adjusted nodes from one iteration to the next falls below the prescribed criterion. In this dissertation, we set the maximum displacement to be less than or equal to 10^{-5}.

6.3 Numerical Results

The adaptive refinement iterative process must stop when the overall global error falls below some preset criterion. In this dissertation, we define the global error to be the square root of a weighted sum of the local errors, where the weights are areas of triangles and the summation is normalized by the total area of the domain. It is given by:

$$\text{Global Error} = \sqrt{\frac{\sum_{i=1}^{N} \mathrm{A}_i |\mathrm{LE}^i|^2}{\sum_{i=1}^{N} \mathrm{A}_i}} \tag{6.10}$$

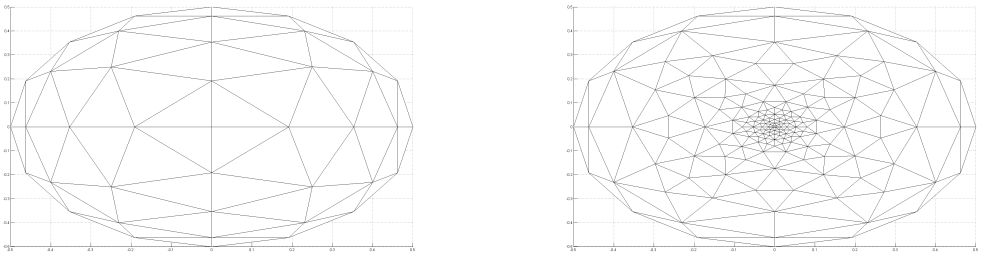

Figure 6.6: Comparison of spherical cavity meshes before (left) and after (right) the adaptive h-refinement technique is applied when using the combined discontinuity error estimator of the EFIE type.

where N is the number of celles, A_i is the area of the i-th cell, and LE^i is the local error obtained by an error estimator. We estimate the global error after each iteration of the adaptive refinement.

As an example to illustrate the adaptive h-refinement technique, consider the spherical cavity with radius 0.5λ excited by an internal z-polarized electric source close to the North pole. Error estimators including the current discontinuity estimator, the combined discontinuity estimator of the EFIE type, and the tangential residual estimator are tested. During each iteration, cells whose error values are greater than the half of the maximum local error are refined, and the refinement will cease when the global error falls below one eighth of its starting value.

Figure 6.6 (a) shows the initial 128-cell mesh for the spherical cavity test problem, while Fig. 6.6(b) shows the 376-cell mesh resulting from the adaptive h-refinement with the combined discontinuity estimator of the EFIE type. We see that the cell sizes have decreased near the North pole because that is the large error region. In terms of the total degrees of freedom (unknowns), the original problem had 192 unknown variables and the refined problem has 564. The global error decreased from 0.074 to 0.0052, a 93% reduction, while the number of cells and the number of unknown variables increased by a factor of 2.9.

The global errors obtained with the combined discontinuity estimator of the EFIE type, the current discontinuity estimator, and the tangential residual error estimator for the spherical cavity are presented in Fig. 6.7, where the x-axis is the number of the unknown variables, and the y-axis is the value of the global errors. The solid line with circle markers

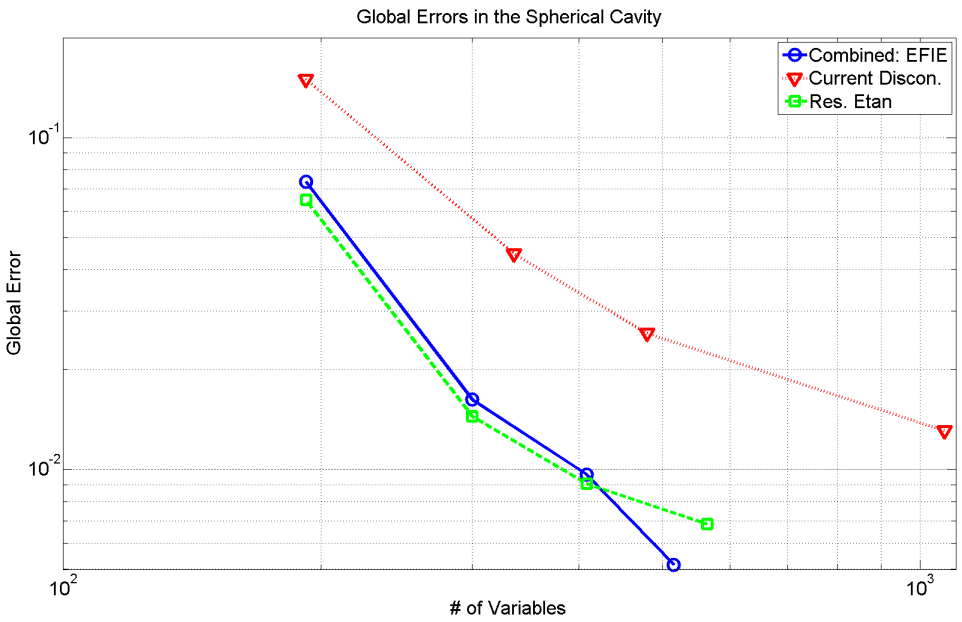

Figure 6.7: Global errors produced by the combined discontinuity estimator of the EFIE type, the current discontinuity estimator, and the tangential residual error estimator for the spherical cavity problem.

denotes the combined discontinuity estimator of the EFIE type, the dotted line with triangle markers denotes the current discontinuity estimator, and the dashed line with square markers denotes the tangential residual estimator. The markers indicate the measured global error for each step of the adaptive refinement process. For each of the three estimators, the adaptive h-refinement requires 3 iterations to reduce the global error to less than 1/8 of its starting value.

Table 22 and Table 23 compare the number of unknown variables and the global errors for uniform h-refinement and adaptive h-refinement. The first column of both tables indicate the error estimator where Comb_{EFIE} is the combined discontinuity estimator of the EFIE type, J_t is the current discontinuity estimator, and Res E_t is the tangential residual error estimator. ΔN in the fourth and sixth columns in Table 22 is the multiplicative factor that the number of unknown variables increased by. For uniform h-refinement the unknowns increased to 768, which is a factor of 4 times greater than that of the original problem, while for adaptive h-refinement with the same error estimator there is about a 2.7 factor increase. In Table 23, ΔG.E. denotes the percentage decrease in the global error for the

Table 22: The number of cells for the original spherical cavity problem, after uniform h-refinement, and after adaptive h-refinement when the combined estimator of the EFIE type, the current discontinuity estimator, and the tangential residual estimator are applied.

Err. Est.	Original	Uniform	ΔN (times)	Adaptive	ΔN (times)
Comb_{EFIE}	192	768	4.0	516	2.7
J_t	192	768	4.0	480	2.5
Res E_t	192	768	4.0	564	2.9

Table 23: The global errors for the original spherical cavity problem, after uniform h-refinement, and after adaptive h-refinement.

Err. Est.	Original	Uniform	Δ G.E. (%)	Adaptive	Δ G.E. (%)
Comb_{EFIE}	0.074	0.027	63.5	0.0052	93.0
J_t	0.15	0.071	52.7	0.026	82.7
Res E_t	0.065	0.028	56.9	0.0068	89.5

same cases.

The tables tell us that uniform h-refinement reduces the global errors by 52%-64% at the expense of increasing the number of unknown variables by a factor of 4, while adaptive h-refinement only requires us to increase the number of unknown variables by 2.5-3 times in order to reduce the global errors by 82%-93%.

As a second example to illustrate adaptive refinement, consider the cylindrical cavity, with an interior z-polarized electric current source near the top and side plates of the cylinder. The radius and the height of the cylinder are 0.2λ and 0.5λ, respectively. Adaptive refinement will be applied using the same error estimator criterion as that used for the spherical cavity problem, but the global error criterion used to terminate the process is set to be one fourth of the initial global error. Again, the combined discontinuity estimator of the EFIE type, the current discontinuity estimator, and the residual error estimator are used in connection with adaptive h-refinement.

The original meshes and the refined meshes for the top and side views of the cylindrical

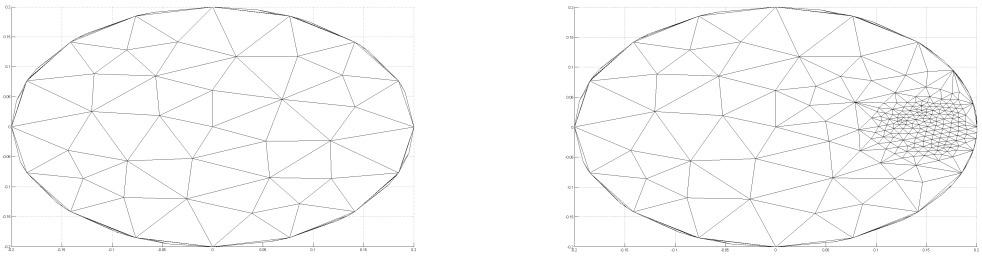

(a) Meshes for the top surface of the cylindrical cavity

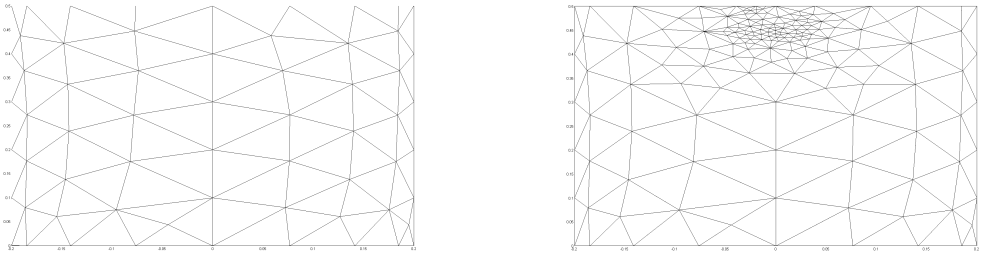

(b) Meshes for the side surface of the cylindrical cavity

Figure 6.8: Comparison of cylindrical cavity meshes before (left) and after (right) adaptive h-refinement is applied when using the combined discontinuity error estimator of the EFIE type.

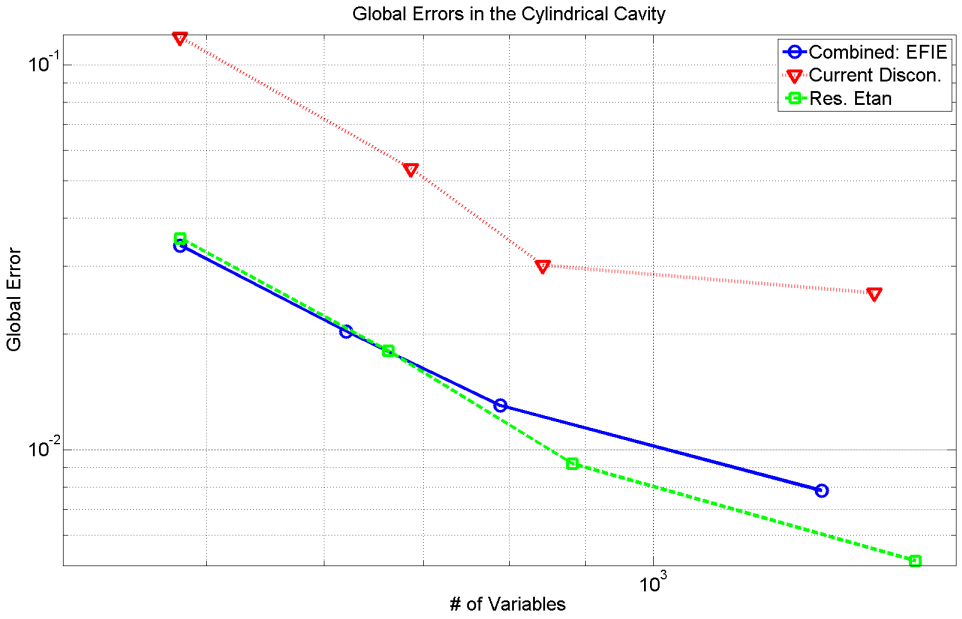

Figure 6.9: Global errors produced by the combined discontinuity estimator of the EFIE type, the current discontinuity estimator, and the tangential residual error estimator for the cylindrical cavity problem.

Table 24: The number of cells in the original cylindrical cavity mesh, after uniform h-refinement, and after adaptive h-refinement when the combined discontinuity estimator of the EFIE type, the current discontinuity estimator, and the tangential residual estimator are applied.

Err. Est.	Original	Uniform	ΔN (times)	Adaptive	ΔN (times)
Comb_{EFIE}	480	780	1.63	789	1.64
J_t	480	780	1.63	843	1.75
Res E_t	480	780	1.63	882	1.84

Table 25: The global errors produced by the original cylindrical cavity mesh, the mesh obtained with uniform h-refinement, and the mesh obtained with adaptive h-refinement.

Err. Est.	Original	Uniform	Δ G.E. (%)	Adaptive	Δ G.E. (%)
Comb_{EFIE}	0.034	0.029	14.7	0.030	61.8
J_t	0.118	0.082	30.1	0.009	74.5
Res E_t	0.036	0.028	20.3	0.001	74.1

cavity are shown in Fig. 6.8. After refinement, cells are dense in the region near the point source. The global errors produced by the different error estimators are presented in Fig. 6.9. The adaptive refinement process requires 3 iterations to decrease the global error to less than 1/4 of its initial value.

Table 24 and Table 25 compare the number of unknown variables and the percentage decrease in the global errors for uniform h-refinement and adaptive h-refinement, for the cylindrical cavity example. The number of unknown variables resulting from uniform h-refinement is 780, which is about 1.63 times greater than that of the original problem. For adaptive h-refinement, we select the global error values where the number of unknown variables is comparable to that of the uniform h-refinement. As indicated in both tables, the global errors produced by adaptive h-refinement are reduced by 62%-75% while those of the uniform h-refinement only decrease by 15%-30%. Therefore, based on results from both examples in Table 22-25, we conclude that the adaptive h-refinement technique demands

less computational costs while ensuring more accuracy than uniformly refining all cells.

6.4 Concluding Remarks

In this chapter, we implemented a simple adaptive h-refinement scheme and tested it on two examples. During each iteration, the algorithm uses an an error estimator to identify cells needing refinement, adds nodes to the appropriate cells, and uses the advancing Delaunay triangulation to create a refined mesh based on the circle test. Since this procedure may entail a decrease in mesh quality, the Laplacian smoothing algorithm was invoked to improve the mesh before the refined problem was solved. A global error measure, a normalized and weighted sum of the local errors, is used to guide the process and to determine when the adaptive refinement iterations should cease. Three error estimators, the current discontinuity estimator, the tangential residual estimator, and the combined discontinuity estimator of the EFIE type are used to identify cells needing refinement at each iteration. All three estimators yielded acceptable performance and a similar rate of convergence.

The spherical cavity and the cylindrical cavity problems were used to test the adaptive h-refinement process and results are compared to that obtained with a uniform h-refinement. A comparison of global errors obtained with uniform h-refinement and adaptive h-refinement show the superiority of adaptive refinement. For the spherical cavity problem, the global errors obtained after adaptive h-refinement are reduced by 82%-93% when the number of unknown variables increased by a factor of 2.5-3, while the global errors obtained after uniform h-refinement are only reduced by 52%-64% while the number of the unknown variables increased by a factor of 4. For the cylindrical cavity, adaptive h-refinement results in a 62%-75% decrease in the global error while uniform h-refinement diminishes the global errors by only 15%-30% for a similar increase in unknown variables. These results demonstrate that the adaptive h-refinement technique is an efficient and reliable method to obtain the accurate numerical solutions for electromagnetic problems of this type.

CHAPTER VII

CONCLUDING REMARKS AND FUTURE WORK

The main focus of the dissertation is to develop and evaluate error estimators and to implement a simple adaptive h-refinement technique in the method of moments. The problem is confined to electromagnetic scattering from PEC objects and is solved by using flat triangular cell modeling, the EFIE, and RWG basis functions. Error estimators are tested for problems involving sources that are located inside or ouside surface of the PEC scatterers. Sources are placed close to the surface to induce large gradients in the currents nearby, which generally leads to large local errors in the numerical solution. This facilitates distinguishing regions with large errors and regions with small errorrs and allows to evaluate the performance of the error estimators.

Error estimators including the current discontinuity error estimator, the charge discontinuity error estimator, the tangential residual error estimator, the normal residual error estimator, the charge recovery error estimator and the implicit error estimator were illustrated in Chapter 3. The accuracy and efficiency of the error estimators were assessed by employing the Pearson correlation coefficient, the local error plots and the scatter plots in Chapter 4. Our conclusions based on the evaluation of the error estimators are summarized as the following:

1. Error estimators in this work showed good accuracy for most of the test cases. According to the averaged Pearson correlation coefficient, the implicit estimator showed the best performance for the spherical cavity, the current discontinuity estimator for the cylindrical cavity and the torus, the normal residual estimator for the plate, and the charge discontinuity estimator for the NASA almond. Although the tangential residual estimator did not have the largest correlation coefficients in all testing cases, it showed the most consistent performance overall.

2. The current discontinuity error estimator and the charge discontinuity error estimator

yielded local errors with minimal computational cost, and the charge recovery error estimator required only slightly more computations. The implicit error estimator required heavier computations than the discontinuity estimators and the charge recovery estimator, but the elapsed time of these error estimators is linearly proportional to the number of cells. On the other hand, the residual error estimators are proportional to the square of the number of cells. In particular, the tangential residual error estimator is the slowest estimator of those studied.

3. The correlation between the charge discontinuity estimator and the charge recovery estimator was always strong because both estimators are related to the discontinuities of the surface charge density. On the other hand, the charge discontinuity estimator and the tangential residual estimator showed strong correlations except when the charge discontinuity estimator failed to determine large error regions.

In Chapter 5, we improved the accuracy of the discontinuity error estimators by measuring the discontinuities of the surface current density and the surface charge density simultaneously. Combining both quantities were accomplished by unifying the units between the current and the charge or by analogy with the form of the EFIE. The former is called the combined discontinuity error estimator of the unit matching type, and the latter is called the combined discontinuity error estimator of the EFIE type. After a similar analysis to that carried out in the Chapter 4, we observed that the accuracy of both combined discontinuity estimators were superior for the test cases where the existing discontinuity estimators failed to identify large error domains correctly. Moreover, the performance of the combined discontinuity estimators were comparable to those of the existing discontinuity error estimators for the other test cases where the existing discontinuity estimators were accurate.

A simple adaptive h-refinement technique was discussed in Chapter 6. The advancing front Delaunay triangulation refined cells that had been identified by the error estimator and Laplacian smoothing improved the quality of the resulting meshes. We measured the global errors for the spherical and cylindrical cavity problems when the current discontinuity error

estimator, the tangential residual error estimator, and the combined discontinuity error estimator of the EFIE type were employed. Numerical results showed that the global errors produced by the adaptive h-refinement decreased more rapidly than those of the uniform h-refinement.

The discussion was restricted to h-refinement, and the method of moments, but the ideas in this dissertation can be extended to adaptive p-refinement and hp-refinement, and to the locally corrected Nyström method, which replaces the integral operator in the surface integral equation with an appropriate quadrature rule. It is known for demanding less computational costs for higher order representations than the method of moments. These topics are left to future work.

The implicit error estimator did not work completely in the NASA almond cases. Considering that the estimator showed strong correlations with the reference error for the other cases, the erratic behavior for the NASA almond is hard to understand. Furthermore, the normal residual error estimator showed relatively poor reliability when comparing it with the other error estimators. These error estimators need to be improved, and associated topics are also left for future work.

APPENDIX A

THE DYADIC GREEN'S FUNCTION FOR CAVITY PROBLEMS

Consider a PEC sphere whose radius is a. When an electrical point source is placed inside the sphere at (r', θ', ϕ'), the dyadic Green's functions and the total magnetic field, $\bar{\bar{H}}^{tot}$, are given by:

$$\bar{\bar{G}}_{mo} = \frac{ik^2}{4\pi} \sum_{n=1}^{\infty} \sum_{m=0}^{\infty} C_{mn} \left[\bar{N}^{(1)}(k) \bar{M}'(k) + \bar{M}^{(1)}(k) \bar{N}'(k) \right] \tag{A.1}$$

$$\bar{\bar{G}}_{ms} = \frac{ik^2}{4\pi} \sum_{n=1}^{\infty} \sum_{m=0}^{\infty} C_{mn} \left[a_n \bar{N}(k) \bar{M}'(k) + b_n \bar{M}(k) \bar{N}'(k) \right] \tag{A.2}$$

$$\bar{\bar{H}}^{tot} = \bar{\bar{G}}_{mo} + \bar{\bar{G}}_{ms} \tag{A.3}$$

With a magnetic point source,

$$\bar{\bar{G}}_{eo} = \frac{ik}{4\pi} \sum_{n=1}^{\infty} \sum_{m=0}^{\infty} C_{mn} \left[\bar{M}^{(1)}(k) \bar{M}'(k) + \bar{N}^{(1)}(k) \bar{N}'(k) \right] \tag{A.4}$$

$$\bar{\bar{G}}_{eo} = \frac{ik}{4\pi} \sum_{n=1}^{\infty} \sum_{m=0}^{\infty} C_{mn} \left[b_n \bar{M}(k) \bar{M}'(k) + a_n \bar{N}(k) \bar{N}'(k) \right] \tag{A.5}$$

$$\bar{\bar{H}}^{tot} = \frac{ik}{\eta} \left[\bar{\bar{G}}_{eo} + \bar{\bar{G}}_{es} \right] \tag{A.6}$$

where

$$C_{mn} = (2 - \delta_0) \frac{(2n+1)}{n(n+1)} \frac{(n-m)!}{(n+m)!} \tag{A.7}$$

$$a_n = -\frac{j_n(ka)}{h_n^{(1)}(ka)} \tag{A.8}$$

$$b_n = -\left. \frac{(d/dr)[r j_n(r)]}{(d/dr)[r h_n^{(1)}(r)]} \right|_{r=ka} \tag{A.9}$$

$$\bar{N}(k) = \frac{1}{k} \nabla \times \nabla \times (\hat{r} r \psi) \tag{A.10}$$

$$\bar{M}(k) = \frac{1}{k} \nabla \times (\hat{r} r \psi) \tag{A.11}$$

$$\bar{N}^{(1)}(k) = \frac{1}{k} \nabla \times \nabla \times \left(\hat{r} r \psi^{(1)} \right) \tag{A.12}$$

$$\bar{M}^{(1)}(k) = \frac{1}{k} \nabla \times \left(\hat{r} r \psi^{(1)} \right) \tag{A.13}$$

$$\psi = j_n(kr)P_n^m(\cos\theta)(\cos m\phi + \sin m\phi) \tag{A.14}$$

$$\psi^{(1)} = h_n^{(1)}(kr)P_n^m(\cos\theta)(\cos m\phi + \sin m\phi) \tag{A.15}$$

$$\delta_m = \begin{cases} 1 & m = 0 \\ 0 & \text{otherwise} \end{cases} \tag{A.16}$$

$P_n^m(\cdot)$ is the first kind of the associated Legendre functions, and $j_n(\cdot)$ and $h_n^{(1)}(\cdot)$ are the spherical Bessel functions defined by

$$j_n(x) = \sqrt{\frac{\pi}{2x}} J_{n+\frac{1}{2}}(x) \tag{A.17}$$

$$h_n^{(1)}(x) = \sqrt{\frac{\pi}{2x}} H_{n+\frac{1}{2}}^{(1)}(x) \tag{A.18}$$

where $J_n(x)$ is the first kind of the Bessel function, and $H_n^{(1)}(x)$ is the first kind of the Hankel function.

Next, consider a cylindrical cavity where the radius and height of the cylinder are given by a and h, respectively. When an electric point source is located at (ρ', ϕ', z') in the cylinder, the dyadic Green's functions and the total magnetic field are given by

$$\bar{\bar{G}}_{m2}^{+} = -k \sum_{n=1}^{\infty}\sum_{m=1}^{\infty} \frac{2-\delta_0}{2\pi} \left[\frac{\bar{N}_{\mu o}(c-z)\bar{M}'_{\mu o}(z')}{\mu^2 I_\mu k_\mu \sin k_\mu c} - \frac{\bar{M}_{\lambda e}(c-z)\bar{N}'_{\lambda e}(z')}{\lambda I_\lambda k_\lambda \sin k_\lambda c} \right], \quad z > z' \tag{A.19}$$

$$\bar{\bar{G}}_{m2}^{-} = -k \sum_{n=1}^{\infty}\sum_{m=1}^{\infty} \frac{2-\delta_0}{2\pi} \left[\frac{\bar{N}_{\mu o}(z)\bar{M}'_{\mu o}(c-z')}{\mu^2 I_\mu k_\mu \sin k_\mu c} - \frac{\bar{M}_{\lambda e}(z)\bar{N}'_{\lambda e}(c-z')}{\lambda I_\lambda k_\lambda \sin k_\lambda c} \right], \quad z < z' \tag{A.20}$$

$$\bar{\bar{H}}^{tot} = \bar{\bar{G}}_{m2} \tag{A.21}$$

For a magnetic point source,

$$\bar{\bar{G}}_{e2}^{+} = -\frac{1}{k^2}\delta(\bar{R} - \bar{R}') + \sum_{n=1}^{\infty}\sum_{m=1}^{\infty} \frac{2-\delta_0}{2\pi} \left[\frac{\bar{N}_{\mu o}(c-z)\bar{N}'_{\mu o}(z')}{\mu^2 I_\mu k_\mu \sin k_\mu c} - \frac{\bar{M}_{\lambda e}(c-z)\bar{M}'_{\lambda e}(z')}{\lambda I_\lambda k_\lambda \sin k_\lambda c} \right], \quad z > z' \tag{A.22}$$

$$\bar{\bar{G}}_{e2}^{-} = -\frac{1}{k^2}\delta(\bar{R}-\bar{R}') + \sum_{n=1}^{\infty}\sum_{m=1}^{\infty}\frac{2-\delta_0}{2\pi}\left[\frac{\bar{N}_{\mu o}(z)\bar{N}'_{\mu o}(c-z')}{\mu^2 I_\mu k_\mu \sin k_\mu c}\right.$$
$$\left. -\frac{\bar{M}_{\lambda e}(z)\bar{M}'_{\lambda e}(c-z')}{\lambda I_\lambda k_\lambda \cos k_\lambda c}\right], \quad z<z' \tag{A.23}$$

$$\bar{\bar{H}}^{tot} = \frac{ik}{\eta}\bar{\bar{G}}_{e2} \tag{A.24}$$

where

$$\bar{M}_{\mu o}(z) = \nabla\times[\hat{z}J_n(\mu\rho)(\sin n\phi+\cos n\phi)\sin k_\mu z] \tag{A.25}$$

$$\bar{M}_{\mu e}(z) = \nabla\times[\hat{z}J_n(\mu\rho)(\sin n\phi+\cos n\phi)\cos k_\mu z] \tag{A.26}$$

$$\bar{N}_{\lambda o}(z) = \nabla\times[\hat{z}J_n(\lambda\rho)(\sin n\phi+\cos n\phi)\sin k_\lambda z] \tag{A.27}$$

$$\bar{N}_{\lambda e}(z) = \nabla\times[\hat{z}J_n(\lambda\rho)(\sin n\phi+\cos n\phi)\cos k_\lambda z] \tag{A.28}$$

$$I_\lambda = \frac{a^2}{2\lambda^2}J'_n(\lambda a) \tag{A.29}$$

$$I_\mu = \frac{a^2}{2\mu^2}\left(\mu^2-\frac{n^2}{a^2}\right)J_n^2(\mu a) \tag{A.30}$$

$$k_\mu^2 = \mu^2+k_z^2 \tag{A.31}$$

$$k_\lambda^2 = \lambda^2+k_z^2 \tag{A.32}$$

$$J_n(p_{nm}) = 0, \quad \mu = \frac{p_{nm}}{a} \tag{A.33}$$

$$J'_n(q_{nm}) = 0, \quad \lambda = \frac{q_{nm}}{a} \tag{A.34}$$

The reference surface current density can be obtained by the PEC boundary condition after applying a dot product of $\bar{\bar{H}}^{tot}$ and desired primed unit vectors. For example, the surface current density on the spherical cavity, induced by exciting a z-polarized electric current source inside the cavity, can be obtained by:

$$\bar{J}_s = -\hat{\rho}\times\left(\bar{z}'\cdot\bar{\bar{H}}^{tot}\right) \tag{A.35}$$

REFERENCES

[1] A. F. Peterson, S. L. Ray, R. Mittra, *Computational methods for electromagnetics*, New York: IEEE press, 1998.

[2] R. F. Harrington, *Field computation by moment methods*, Oxford University Press, 1996.

[3] W. C. Gibson, *The method of moments in electromagnetics*, CRC press, 2014.

[4] D. B. Davidson, *Computational electromagnetics for RF and microwave engineering*, Cambridge University Press, 2010.

[5] A. F. Peterson, *Mapped vector basis functions for electromagnetic integral equations*, Synthesis Lectures on Computational Electromagnetics 1.1, 2005.

[6] A. F. Peterson, and M. M. Bibby, *An Introduction to the Locally-Corrected Nyström Method*, Morgan & Claypool Publishers, 2009.

[7] R. F. Harrington, *Time-Harmonic Electromagnetic Fields*, New York: IEEE press, 2001.

[8] D. G. Dudley, *Mathematical foundations for electromagnetic theory*, New York: IEEE press, 1994.

[9] C. Tai, *Dyadic Green functions in electromagnetic theory*, New York: IEEE press, 1994.

[10] H. J. Eom, *Electromagnetic wave theory for boundary-value problems*, Springer, 2004.

[11] M. Ainsworth, and J. T. Oden., *A posteriori error estimation in finite element analysis*, John Wiley & Sons, 2011.

[12] S. Usman, *Adaptive numerical techniques for the solution of electromagnetic integral equations*, PhD Dissertation: Georgia Institute of Technology, 2011.

[13] W. J. Yu,, *Electromagnetic fields by dipole current inside a spherical conducting cavity*, MS Dissertation: KAIST, 2007.

[14] J. K. Paek, *Radiation of Hertzian dipole in slotted circular conducting cylinders*, PhD Dissertation: KAIST, 2009.

[15] M. M. Botha, "A Family of Augmented Duffy Transformations for Near-Singularity Cancellation Quadrature," *Antennas and Propagation, IEEE Transactions on*, vol.61, no.6, pp.3123-3134, Jun. 2013.

[16] M. M. Bibby, C. M. Coldwell, and A. F. Peterson, "A High Order Numerical Investigation of Electromagnetic Scattering From a Torus and a Circular Loop," *Antennas and Propagation, IEEE Transactions on*, vol.61, no.7, pp.3656-3661, Jul. 2013.

[17] B. J. Davies, "A Least-Squares Boundary Residual Method for the Numerical Solution of Scattering Problems," *Microwave Theory and Techniques, IEEE Transactions on*, vol.21, no.2, pp.99-104, Feb. 1973.

[18] F. J. C. Meyer, and D. B. Davidson, "A posteriori error estimates for two-dimensional electromagnetic field computations: Boundary elements and finite elements," *Applied Computational Electromagnetics Society Journal*, vol.11, no.2, pp.40-54, Feb. 1996.

[19] T. Grätsch, and K. J. Bathe, "A posteriori error estimation techniques in practical finite element analysis," *Computers & structures*, vol.83.4, pp.235-265, 83.4 2005.

[20] J. J. Rencis, and J. Kwo-Yih, "A self-adaptive h-refinement technique for the boundary element method," *Computer methods in applied mechanics and engineering*, vol.73.3, pp.295-316, 1989.

[21] A. F. Peterson, "A simple approach for estimating errors bars to accompany moment-method and finite-element-method results," *Antennas and Propagation Magazine, IEEE*, vol.35, no.6, pp.61-62, Dec. 1993.

[22] M. M. Botha, "Accuracy of Near-Singularity Cancellation Quadrature Schemes for the Dynamic MoM Kernel," *Antennas and Wireless Propagation Letters, IEEE*, vol.12, pp.714-717, 2013.

[23] D. Harutyunyan, F. Izsák, F. J. J. W. van der Vegt and M. A. Botchev, "Adaptive finite element techniques for the Maxwell equations using implicit a posteriori error estimates," *Computer Methods in Applied Mechanics and Engineering*, vol.197.17, pp.1620-1638, 2008.

[24] P. Girdinio, P. Molfino, G. Molinari and M. Nervi, "Adaptive Meshing in Two-Variable Static Problems with Field Based Error Estimators Using Edge and Facet Elements," *Applied Computational Electromagnetics Society journal*, vol.12, pp.142-147, 1997.

[25] M. M. Kostic, and B. M. Kolundzija, "Adaptive refinement of higher order method of moment applied to surface integral equations," *Antennas and Propagation (EuCAP), 2010 Proceedings of the Fourth European Conference on*, pp.1-5, 12-16 Apr. 2010.

[26] X. Wang, M. M. Botha, and J. M. Jin, "An error estimator for the moment method in electromagnetic scattering," *Microwave and optical technology letters*, vol.44.4, pp.320-326, 2005.

[27] M. M. Botha, and D. B. Davidson, "An explicit a posteriori error indicator for electromagnetic, finite element-boundary integral analysis," *Antennas and Propagation, IEEE Transactions on*, vol.53, no.11, pp.3717-3725, Nov. 2005.

[28] W. Rachowicz and A. Zdunek, "An hp-adaptive finite element method for scattering problems in computational electromagnetics," *International Journal for Numerical Methods in Engineering*, vol.62, pp.1226-1249, 2005.

[29] A. D. Yaghjian, "Augmented electric and magnetic-field integral equations," *Radio Science*, vol. 16, pp.987-1001 1981.

[30] V. Skala, "Barycentric coordinates computation in homogeneous coordinates," *Computers & Graphics*, vol.32.1, pp.120-127, Jul. 2008.

[31] G. C. Hsiao and R. E. Kleinman, "Error control in numerical solution of boundary integral equations," *Applied Computational Electromagnetics Society journal*, vol. 11, pp. 32-36, 1996.

[32] E. Kita, and N. Kamiya, "Error estimation and adaptive mesh refinement in boundary element method, an overview," *Engineering Analysis with Boundary Elements*, vol. 25.7, pp.479-495, 2001.

[33] R. De Smedt, and J. G. Van Bladel, "Field singularities near aperture corners," *Physical Science, Measurement and Instrumentation, Management and Education - Reviews, IEE Proceedings A* , vol.134, no.8, pp.694-698, Sep. 1987.

[34] J. J. Rodrguez, and H. Power, "h-Adaptive mesh refinement strategy for the boundary element method based on local error analysis," *Engineering analysis with boundary elements*, vol.25.7, pp.565-579, 2001.

[35] J. Wang and J. P. Webb, "Hierarchal vector boundary elements and p-adaption for 3-D electromagnetic scattering," *Antennas and Propagation, IEEE Transactions on*, vol.45, no.12, pp.1869-1879, Dec. 1997.

[36] D. A. Dunavant, "High degree efficient symmetrical Gaussian quadrature rules for the triangle," *International journal for numerical methods in engineering*, vol.21.6, pp.1129-1148, 1985.

[37] S. M. Rao, D. Wilton, and A. W. Glisson,, "Electromagnetic scattering by surfaces of arbitrary shape," *Antennas and Propagation, IEEE Transactions on*, vol.30, no.3, pp.409-418, May 1982.

[38] M. Bibby, A. F. Peterson, A.F. and C. M. Coldwell, "High Order Representations for Singular Currents at Corners," *Antennas and Propagation, IEEE Transactions on*, vol.56, no.8, pp.2277-2287, Aug. 2008.

[39] J. P. Webb, "hp-Adaption for Computing Scattering Parameters on Tetrahedral Meshes," *Electromagnetics*, vol.34.3-4, pp.298-306, 2014.

[40] M. M. Botha, and W. J. Strydom, "Integrating the dynamic MoM kernel with near-singularity cancellation quadrature schemes," *AFRICON 2013*, pp.1-3, 9-12 Sept. 2013.

[41] M. M. Botha and D. B. Davidson, "Investigation of an explicit, residual-based, a posteriori error indicator for the adaptive finite element analysis of waveguide structures," *Applied Computational Electromagnetics Society journal*, vol. 21, no. 1, pp.63-71+, Mar. 2006.

[42] U. Saeed and A. F. Peterson, "Local residual error estimators for the method of moments solution of electromagnetic integral equations," *Applied Computational Electromagnetics Society journal*, vol. 26, no. 5, pp.403-410, May 2011.

[43] G. C. Hsiao and R. E. Kleinman, "Mathematical foundations for error estimation in numerical solutions of integral equations in electromagnetics," *Antennas and Propagation, IEEE Transactions on*, vol.45, no.3, pp.316-328, Mar. 1997.

[44] R. Cools, and P. Rabinowitz, "Monomial cubature rules since Stroud: a compilation," *Journal of Computational and Applied Mathematics*, vol. 48.3, pp.309-326, July 1993.

[45] M. A. Khayat, and D. R. Wilton, "Numerical evaluation of singular and near-singular potential Integrals," *Antennas and Propagation, IEEE Transactions on*, vol.53, no.10, pp.3180-3190, Oct. 2005.

[46] P. O. Persson, and G. Strang, "A simple mesh generator in MATLAB," *SIAM review*, vol.46.2, pp.329-345, July 2004.

[47] A. F. Peterson, "Observed Baseline Convergence Rates and Superconvergence in the Scattering Cross Section Obtained From Numerical Solutions of the MFIE," *Antennas and Propagation, IEEE Transactions on*, vol.56, no.11, pp.3510-3515, Nov. 2008.

[48] S. Prudhomme, and J. T. Oden, "On goal-oriented error estimation for elliptic problems: application to the control of pointwise errors," *Computer Methods in Applied Mechanics and Engineering*, vol.176.1, pp.313-331, 1999.

[49] C. P. Davis, and K. F. Warnick, "On the physical interpretation of the Sobolev norm in error estimation," *Applied Computational Electromagnetics Society journal*, vol.2, pp.144-150, July 2005.

[50] M. M. Bibby and Peterson, A.F., "On the use of overdetermined systems in the adaptive numerical solution of integral equation," *Antennas and Propagation, IEEE Transactions on*, vol.53, no.7, pp.2267-2273, July 2005.

[51] A. P. C Fourie, D. C. Nitch, and A. R. Clark, "Predicting MoM error currents by inverse application of residual E-fields," *Applied Computational Electromagnetics Society journal*, vol.14, pp.72-75, 1999.

[52] J. S. Savage, and A. F. Peterson, "Quadrature rules for numerical integration over triangles and tetrahedra," *Antennas and Propagation Magazine in IEEE*, vol.38, no.3, pp.100-102, June 1996.

[53] O. C. Zienkiewicz, , B. Boroomand, and J. Z. Zhu, "Recovery procedures in error estimation and adaptivity Part I: Adaptivity in linear problems," *Computer methods in applied mechanics and engineering*, vol.176.1, pp.111-125, 1999.

[54] W. J. Strydom, and M. M. Botha, "Recovery-based a posteriori error estimation for the charge in the method of moments," *Antennas and Propagation (EuCAP), 2015 9th European Conference on*, pp.1-4, 13-17 Apr. 2015.

[55] A. W. Glisson, and D. Wilton, "Simple and efficient numerical methods for problems of electromagnetic radiation and scattering from surfaces," *Antennas and Propagation, IEEE Transactions on*, vol.28, no.5, pp.593-603, Sep. 1980.

[56] O. C. Zienkiewicz, and J. Z. Zhu, "Superconvergence and the superconvergent patch recovery," *Finite elements in analysis and design*, vol.19.1, pp.11-23, 1995.

[57] J. Meixner, "The behavior of electromagnetic fields at edges," *Antennas and Propagation, IEEE Transactions on*, vol.20, no.4, pp.442-446, Jul. 1972.

[58] K. J. Bunch, and R. W. Grow, "The boundary-residual method for three-dimensional homogeneous field problems with boundaries of arbitrary geometry," *International Journal of Infrared and Millimeter Waves*, vol.10.8, pp.1007-1032, Jul. 1989.

[59] O. C. Zienkiewicz, and J. Z. Zhu, "The superconvergent patch recovery (SPR) and adaptive finite element refinement," *Computer Methods in Applied Mechanics and Engineering*, vol.101.1, pp.207-224, 1992.

[60] M. M. Bibby, A. F. Peterson, and C. M. Coidwell, "Use of extrapolation to improve accuracy and enhance confidence in numerical results," *Antennas and Propagation Magazine, IEEE*, vol.50, no.4, pp.150-155, Aug. 2008.

[61] Peterson, A.F., Wilton, D.R. and Jorgenson, R.E., "Variational nature of Galerkin and non-Galerkin moment method solutionse," *Antennas and Propagation, IEEE Transactions on*, vol.44, no.4, pp.500-503, Apr. 1996.

[62] H. Abdi, "The Kendall rank correlation coefficient," *Encyclopedia of Measurement and Statistics*, pp.508-510, 2007.

[63] J. R. Taylor, *An introduction to error analysis: the study of uncertainties in physical measurements*, University Science Books, Mill Valley, CA, 1982.

[64] H. J. Berendsen, *A student's guide to data and error analysis*, Cambridge University Press, 2011.

[65] J. F. Lee, and R. Dyczij-Edlinger, "Automatic mesh generation using a modified Delaunay tessellation," *Antennas and Propagation Magazine*, IEEE , vol.39, no.1, pp.34-45, Feb. 1997.

[66] D. T. Lee, and B. J. Schachter, "Two algorithms for constructing a Delaunay triangulation," *International Journal of Computer & Information Sciences*, vol.9, no.3, pp.219-242, Jun. 1980.

[67] M. L. Merriam, "An efficient advancing front algorithm for Delaunay triangulation," *29th Aerospace Sciences Meeting, Aerospace Sciences Meetings*, vol.1, pp. 1-9, Jan. 1991.

[68] J. F. Lee, R. Dyczij-Edlinger, E. Lucas, and T. Fontana,, "Application of steepest descent smoothing and de-meshing techniques in h-version adaptive FEMs," *IEEE Transactions on Magnetics*, IEEE , vol. 35, no. 3, pp. 1346-1349, May 1999.

[69] Y. Srisukh and R. Lee, "The nested h refinement in 2D FETD via the hanging variable technique," *2006 IEEE Antennas and Propagation Society International Symposium*, Albuquerque, NM, pp. 2821-2824 Jul. 2006.

[70] R. Ait-Sadi and C. R. I. Emson, "A 'three step' refinement process for automatic 2-D mesh adaption,", *Computation in Electromagnetics, 1994. Second International Conference on*, London, 1994, pp. 215-218.

[71] H. L. De Cougny, and M. S. Shephard, "Parallel refinement and coarsening of tetrahedral meshes,", *International Journal for Numerical Methods in Engineering*, vol. 46, no. 7, pp. 1101-1125, 1999.

[72] A. C. Woo, H. T. G. Wang, M. J. Schuh and M. L. Sanders, "EM programmer's notebook-benchmark radar targets for the validation of computational electromagnetics programs", *in IEEE Antennas and Propagation Magazine*, vol. 35, no. 1, pp. 84-89, Feb 1993.

[73] "Pearson product-moment correlation coefficient", *Wikipedia*, accessed on 2016. [Online]. Available: https://en.wikipedia.org/wiki/Pearson_product-moment_correlation_coefficient.

[74] "Laplacian smoothing", *Wikipedia*, accessed on 2016. [Online]. Available: https://en.wikipedia.org/wiki/Laplacian_smoothing.

[75] "Winding number", *Wikipedia*, accessed on 2016. [Online]. Available: https://en.wikipedia.org/wiki/Winding_number.

[76] Dan Sunday, "Inclusion of a point in a polygon", accessed on 2016. [Online]. Available: http://geomalgorithms.com/a03-_inclusion.html.

VITA

Sang Kyu Kim received the B.S. in electrical engineering from Hongik University, Seoul, Korea, in 2008 and the M.S. degree in electrical engineering from KAIST, Dae-jeon, Korea in 2010, respectively. He is received the M.S. degree in mathematics from the Georgia Institute of Technology, Atlanta, GA, USA in 2015, where he is currently pursuing the Ph.D. degree in electrical and computer engineering. His research focus is on error estimation and adaptive refinement technique in the electromagnetics.